

Determining Inclinations of Active Galactic Nuclei Via Their Narrow-Line Region Kinematics - I. Observational Results¹

T.C. Fischer², D.M. Crenshaw², S.B. Kraemer³, H.R. Schmitt⁴

ABSTRACT

Active Galactic Nuclei (AGN) are axisymmetric systems to first order; their observed properties are likely strong functions of inclination with respect to our line of sight. However, except for a few special cases, the specific inclinations of individual AGN are unknown. We have developed a promising technique for determining the inclinations of nearby AGN by mapping the kinematics of their narrow-line regions (NLRs), which are often easily resolved with *Hubble Space Telescope* (*HST*) [O III] imaging and long-slit spectra from the Space Telescope Imaging Spectrograph (STIS). Our studies indicate that NLR kinematics dominated by radial outflow can be fit with simple biconical outflow models that can be used to determine the inclination of the bicone axis, and hence the obscuring torus, with respect to our line of sight. We present NLR analysis of 53 Seyfert galaxies and resultant inclinations from models of 17 individual AGN with clear signatures of biconical outflow. Our model results agree with the unified model in that Seyfert 1 AGN have NLRs inclined further toward our line of sight (LOS) than Seyfert 2 AGN. Knowing the inclinations of these AGN NLRs, and thus their accretion disk and/or torus axes, will allow us to determine how their observed properties vary as a function of polar angle. We find no correlation between the inclinations of the AGN NLRs and the disks of their host galaxies, indicating that the orientation of the gas in the torus is independent from that of the host disk.

¹Based on observations made with the NASA/ESA Hubble Space Telescope, obtained at the Space Telescope Science Institute, which is operated by the Association of Universities for Research in Astronomy, Inc. under NASA contract NAS 5-26555. These observations are associated with programs 11243, 11611, and 12212

²Department of Physics and Astronomy, Georgia State University, Astronomy Offices, 25 Park Place, Suite 600, Atlanta, GA 30303; fischer@chara.gsu.edu

³Institute for Astrophysics and Computational Sciences, Department of Physics, The Catholic University of America, Washington, DC 20064

⁴Naval Research Laboratory, Washington, DC 20375

Subject headings: galaxies: active, galaxies: Seyfert, galaxies: kinematics and dynamics, galaxies: individual(Akn 564, Circinus, IC 3639, IRAS 11058-1131, MCG-6-30-15, Mrk 34, Mrk 279, Mrk 348, Mrk 463e, Mrk 493, Mrk 509, Mrk 705, Mrk 766, Mrk 1040, Mrk 1044, Mrk 1066, NGC 1358, NGC 1386, NGC 1667, NGC 2110, NGC 2273, NGC 3081, NGC 3227, NGC 3393, NGC 3516, NGC 3783, NGC 4051, NGC 4303, NGC 4395, NGC 4507, NGC 5135, NGC 5252, NGC 5283, NGC 5347, NGC 5427, NGC 5506, NGC 5548, NGC 5643, NGC 5695, NGC 5728, NGC 5929, NGC 6300, NGC 7212, NGC 7469, NGC 7674, NGC 7682, NGC 788, UM 146)

1. Introduction

Within all massive galaxies with bulges are supermassive black holes (SMBHs) that reside in the center of their hosts and whose masses usually exceed 10^6 solar masses (M_{\odot}). While most galaxies in the current epoch contain SMBHs that lie dormant, a small percentage of galaxies with Active Galactic Nuclei (AGN) contain SMBHs that are actively gaining mass from the surrounding matter of their accretion disk. As the matter falls into a SMBH, it loses angular momentum and gravitational potential energy and as a result emits a massive amount of electromagnetic radiation, often outshining the rest of the galaxy.

Seyfert galaxies, a relatively moderate luminosity ($L_{bol} \approx 10^{43} - 10^{45}$ erg s $^{-1}$), nearby ($z \leq 0.1$) subset of the overall collection of AGN, exhibit a dichotomy of broad and narrow hydrogen and other permitted emission lines. This led the Seyfert class of objects to be divided into two groups (Khachikian & Weedman 1974). Seyfert 1 galaxies are defined to have spectra containing broad (full width at half-maximum [FWHM] ≥ 1000 km s $^{-1}$) permitted lines, narrower (FWHM ≤ 1000 km s $^{-1}$) forbidden lines, and distinct, non-stellar optical and UV continua while Seyfert 2s contain only narrow permitted and forbidden lines and their optical and UV continua are dominated by the host galaxy. This difference can be attributed to these AGN being similar objects being viewed from different angles, where the central engine and source of broad line emission is visible in Seyfert 1s and obscured by a toroidal structure of gas and dust in Seyfert 2s (Antonucci 1993).

The NLR, a knotty, extended (1 - 1000 pc) region responsible for emitting the narrow emission lines visible in both Seyfert types, is the focus of our study as it is the only AGN component that can be spatially resolved in the optical. The narrow emission lines are generated by low-density ($n_H \leq 10^6$ cm $^{-3}$) gas clouds photo-ionized by the non-stellar continuum emission of the AGN (Peterson 1997; Osterbrock & Ferland 2006). The clouds are often driven in outflow by the central engine (Hutchings et al. 1998; Crenshaw et al. 2000; Crenshaw & Kraemer 2000), and are generally in a biconical structure, with the apex of the bicone residing in the central AGN (Pogge 1988; Schmitt et al. 1994). Observed primarily in Seyfert 2s, these biconical formations have projected opening angles typically in the range of $\sim 30^\circ - 100^\circ$, often with well defined linear edges (Schmitt et al. 2003), which imply the NLR is defined by collimation of ionizing radiation by an optically thick, torus-shaped absorbing material (Antonucci & Miller 1985), or possibly a dusty disk wind (Elitzur & Shlosman 2006), at small radial distances of a few parsecs from the SMBH. Around the same scale and position of the NLR, Seyferts also sometimes contain radio emitting knots of low-density plasma, which suggests that there may be some connection between the thermal narrow-line gas and the non-thermal plasma. At radial distances of ≥ 1 kpc, ionized gas often exists in an extended NLR (ENLR) likely in the plane of the host galaxy (Unger et al. 1987). Seyfert

hosts can have any morphological types, but tend to be found in early type galaxies (Ho et al. 1997).

While it is generally accepted that Seyfert 1 AGN are viewed more face-on and Seyfert 2 AGN are viewed more edge-on with respect to the obscuring toroidal structure, the specific inclinations of all but a few AGN are generally unknown. Thus we still do not know how the properties of AGN change with inclination beyond comparing Seyfert 1s and 2s. By employing our NLR kinematics mapping technique, detailed below, we can for the first time determine our viewing angle to a sample of AGN and begin finding inclination dependencies, allowing us to progress beyond the simple unified model of Type 1 and 2 AGN.

We have previously shown that the NLR kinematics in Seyfert galaxies are often dominated by radial outflow in the approximate shape of a bicone, through kinematic modeling of the NLRs of five individual AGN: NGC 1068 (Seyfert 2; Crenshaw & Kraemer 2000; Das et al. 2006), NGC 4151 (Seyfert 1; Crenshaw et al. 2000; Das et al. 2005), Mrk 3 (Seyfert 2; Ruiz et al. 2001; Crenshaw et al. 2010), Mrk 573 (Seyfert 2; Fischer et al. 2010), and Mrk 78 (Seyfert 2; Fischer et al. 2011).

Our current outflow model originated in the Crenshaw & Kraemer (2000) study while attempting to determine the nature of the NLR kinematics as possibly due to in-fall, rotation, outflow, or some other flow pattern. By observing NGC 1068, the nearest bright Seyfert 2 galaxy, with the *HST* STIS, they were able to resolve [O III] emission-line knots that presumably accelerated out from the inner nucleus, reached a terminal velocity, and then decelerated due possibly to drag through interactions with the surrounding ambient material. Additionally, a lack of low radial velocities where the kinematic curves peaked suggested that the NLR was evacuated of [OIII] emission along its axis, which is close to the plane of the sky in NGC 1068. These data, combined with *HST* imaging that indicated a biconical geometry for the NLRs of many Seyfert 2 galaxies (Schmitt & Kinney 1996), led to the postulation that a radial outflow shaped as a biconical shell could reproduce the NLR kinematics seen in the Seyfert 2 galaxy NGC 1068. The resultant kinematic model assumes the knots are radially outflowing and accounted for by a simple velocity law close to the nucleus, $v = kr$, where r is the distance from the nucleus and k is a constant. In addition to gaining a better understanding of the NLR kinematics, their model also produced a geometry of the NLR, including an inclination of 5° out of the plane of the sky, which was required for the model to fit the observed radial velocities.

Crenshaw et al. (2000) proceeded to apply their new kinematic model to the NLR of the brightest Seyfert 1 galaxy NGC 4151, in which they found, similarly to their model of NGC 1068, evidence for radial acceleration and subsequent deceleration of emission-line knots and a hollowed region near the axis. The largest difference between the two NLR models was

their inclination from our line of sight. The bicone axis of NGC 4151 was inclined closer to our line of sight at $\sim 45^\circ$ out of the plane of the sky versus $\sim 5^\circ$ out of the plane of the sky, nearly perpendicular to our line of sight, for NGC 1068. By matching the observed radial velocities of a second Seyfert galaxy to their kinematic model, it was realized that it could be possible to determine not just the nature of the NLR kinematics, but the orientation and geometry of the AGN system as well.

Das et al. (2005, 2006) tested the outflow model with more detailed data sets using higher-resolution spectra at multiple slit locations across the NLRs of NGC 4151 and NGC 1068 respectively. The original modeling code used by Crenshaw & Kraemer (2000) was also updated to include a variable n in the velocity law, $v = kr^n$. They concluded that the models from Crenshaw et al. (2000) and Crenshaw & Kraemer (2000) were consistent with their own and that the original velocity law ($n = 1$) remained the strongest fit to their kinematic data. Further kinematic studies of three additional AGN, Mrk 3, Mrk 78, and Mrk 573, confirm the success of the original velocity law (Crenshaw et al. 2010; Fischer et al. 2010, 2011).

In order to determine if any correlations exist between inclination and other AGN parameters, we require more data points than the five individual AGN previously modeled by our group. Thus, the motivation behind this study is to determine the inclinations of a larger sample of individual AGN, add them to our previous AGN inclination sample, and compare them with observed properties of the AGN to identify any existing correlations (to be published in a forthcoming paper). Section 2 describes the observations used in our work. Sections 3 and 4 describe our analysis technique of the spectral observations and the resultant kinematics. Section 5 describes the models and how we employ them, with notes on modeled AGN results in Sections 6. Finally, Sections 7 and 8 contain discussion and conclusions respectively.

2. Observations

All AGN in this work were observed using *HST* STIS, with the CCD detector through either a slit of $52'' \times 0.2''$ or $52'' \times 0.1''$, or in a slitless mode (discussed more in depth below). Our sample includes all Seyferts with archival G430L or G430M long-slit spectra of [O III] $\lambda 5007$ in the Mikulski Archive for Space Telescopes (MAST; 32 AGN), as well as 11 Seyferts from our own G430M observations (GO-11611 and GO-12212, PI Crenshaw). Additional archival G750M observations of $H\alpha$ $\lambda 6563$ that exist for our sample were also harvested, as a large fraction of $H\alpha$ emission originates in the same gas that emits [O III]. Both emission lines were chosen as they are typically the strongest optical lines originating in the NLR

([O III]/H β \approx 10; H α /H β \approx 3; Peterson 1997). Observations using the G750M grating can contain emission that originates from star formation or H II regions. However, when we compare velocities measured from H α emission to those measured from [O III] NLR emission at the same slit position, we find that they agree fairly well. Specifications of each grating used are listed in Table 1.

To expand our sample even further, we returned to results from Ruiz et al. (2005) to analyze slitless G430M spectra of 6 Seyfert AGN; 4 of which were new to our sample. To quickly summarize their spectral measurement process, emission-line knots were identified in both the direct and grating-dispersed images. Both spatial and spectral images were then fit row by row with a Gaussian for each knot and the radial velocity of each knot was determined by subtracting the positions of the Gaussian peaks in the direct and dispersed images. This created a two-dimensional velocity map where each knot in the image was assigned a radial velocity, from which we could extract in a strip across the image to simulate a long-slit observation. From the slitless observations, only very bright, distinct knots of emission yielded radial velocities. Thus, simulated observations were taken in 2'' wide slits. These pseudo-slit observations, which already contain radial velocity measurements, were then assigned a distance along the slit to the nucleus position determined via imaging, which produced data sets in an identical fashion as typical long-slit observations which we fit with our modeling program.

In total, the expanded sample, not including the five AGN previously modeled by our group, contains 161 spectra of 48 AGN. The STIS image scale is 0.05'' pixel⁻¹ and the spatial resolution is 0.1'' pixel⁻¹ in the cross-dispersion direction. In many cases, multiple observations at the same position were dithered along the slit with respect to the first spectrum to avoid problems due to hot pixels. Wavelength calibration lamp spectra were taken during Earth occultation. Observation parameters, including slit orientation, offset distance from the continuum flux peak, and the source of the observation, are listed in Table 2. Spectral images of all long-slit observations are available online.

The STIS spectra were processed using Interactive Data Language (IDL) software developed at NASA's Goddard Space Flight Center for the STIS Instrument Definition Team. Cosmic-ray hits were removed before further processing. The zero points of the wavelength scales were corrected using wavelength-calibration exposures taken after each observation. Finally, the spectra were geometrically rectified and flux calibrated to provide spectral images that have a constant wavelength along each column and display fluxes in units of erg s⁻¹ cm⁻² Å⁻¹ per cross-dispersion pixel. Occasionally, a number of hot pixels remained after the data were processed. In those cases, we performed an additional cleaning step by replacing the bad pixel with a local median value in the data.

Images with overplotted STIS slit positions for each modeled AGN are depicted in Appendix A, with all other images available online. Table 3 lists the *HST* instruments used to image each AGN, as well as their redshifts, distances, and transverse scales assuming $H_0 = 73 \text{ km Mpc s}^{-1}$. Redshifts were taken from the NASA/IPAC Extragalactic Database (NED). Distances for nearby AGN ($z < .01$) were retrieved from the Extragalactic Distance Database (EDD; Tully et al. 2009), all other distances were derived from measured redshifts. Images taken with filters containing [O III] $\lambda 5007$ or $H\alpha \lambda 6563$ emission were preferred, otherwise wide-band continuum filters, which contained some emission-line contributions, were used.

3. Analysis

The described procedure to extract velocities and other information from a long-slit observation applies to every slit position in our sample excluding slitless observations. Each spectral image produced one spectrum per cross-dispersed pixel along the slit centered on the [OIII] or $H\alpha$ emission lines. Because there are 2 pixels per resolution element, the data are slightly oversampled. In each spectrum, individual [OIII] $\lambda 5007$ or $H\alpha \lambda 6563$ emission lines were fit with Gaussians over an average continuum taken from line-free regions throughout the spectrum. Many spectra contained two or more lines, where each identifiable peak was fit with a Gaussian. If an emission line contains a peak and an asymmetric wing, where the wing is a flux component responsible for creating a significant ($> 3\sigma$) asymmetry in an emission line traceable through several spectra along the slit, our fitting program fits the wing as a separate line.

The central peak of each Gaussian is the central wavelength from which we measured a Doppler shifted velocity for both the [O III] $\lambda 5007$ and $H\alpha$ emission lines, given in the rest frame of the galaxy and using [O III] and $H\alpha$ vacuum rest wavelengths of 5008.2\AA and 6564.6\AA respectively. In solving for each velocity, we do not need the relativistic formula for velocity because our lines are always shifted less than 2000 km s^{-1} .

We employ a Gaussian fit rather than a direct integration across the line profile because in most cases the former is more suited to extract individual velocities from blended lines. Noisy spectra ($S/N < 3$ per resolution element) or broad $H\alpha$ lines near the nucleus of Seyfert 1s, which blended into the surrounding [NII] doublet, were not fitted.

Figure 1 depicts a typical progression of spectra illustrating the fitting of multiple lines with change in position. The graphs represent spectra taken from the central slit position over Mrk 34 and range from $0''$ to $0.3''$ in increments of $0.05''$, stepping away from the nucleus in the eastern direction.

In the initial panel at the upper left, a central line is visible, which we fit with a Gaussian. Besides obvious line peaks that are easy to fit, additional lines are identified by comparing adjacent spectra along the slit. Passing through multiple sets of emission lines, we should expect resolved knots of emission to be present in more than a single spectrum. As we step away from the nucleus, a second blueshifted line emerges to the left of the original line and is also fit with a Gaussian. A possible third line is visible in the fourth and fifth panels which is well fit with a Gaussian without altering the fits to the two adjacent, high-flux lines. The center line ceases to exist in the bottom right panel as it can no longer be fit with a Gaussian and more closely resembles the increased noise seen at 5250 and 5270Å, a result of this panel containing line fluxes approximately half those of the previous panels.

Figure 2 shows the entire velocity data set, as well as full-width at half-maxima (FWHM), and normalized fluxes across the central slit position for Mrk 34 (further kinematics for each modeled AGN are given in Appendix A). Note that multiple velocities exist at several positions along the slit as shown in Figure 1, and that they generally agree between the two gratings. The scaled differences in FWHM are due to uncorrected instrumental spectral resolutions of ~ 650 , ~ 60 , and ~ 130 km s $^{-1}$ for the G430L, G430M, and G750M gratings respectively. Adding the FWHM of the resolved G750M H α lines (as well as G430M [O III] lines) to the FWHM of the line spread function of the G430L grating for a 0.2" slit in quadrature gives a value typical of the observed FWHM of the G430L [O III] lines indicating the intrinsic widths from the gratings are the same. Further discrepancies can be attributed to blending of lines within the G430L spectra. Lumpiness of fluxes across long-slit observations are due to spatially resolved knots of emission.

There are two sources of uncertainty in our velocity measurements. The first is that the measured emission lines are not perfect Gaussians, as shown in Figure 1, but instead tend to have stronger peaks than pure Gaussians. To measure a typical value for this uncertainty, denoted as σ_{hi} , we found the average difference between Gaussians fit to a selection of 15 random, isolated high signal-to-noise emission lines as detailed above and the actual centroid of the same line. The second error comes from photon noise, σ_{noise} . By repeating the measurements performed on high S/N lines to 15 random, low S/N lines and subtracting in quadrature the subsequent averaged value from the average σ_{hi} , we can solve for the remaining variance due to photon noise, σ_{noise} . Both errors are given for each grating in Table 1, as well as the total maximum error (σ_{total}), a summation of the two errors in quadrature. Varied continuum placements for randomly selected spectra were also tested, but did not affect the central wavelengths significantly. It should be noted that σ_{total} is an upper limit that accounts for the maximum value of each contributing error, as the total error will be lower for high signal-to-noise spectra because σ_{noise} will be close to zero.

4. Observational Results

Appendix A shows a portion of the radial velocities, FWHM, and fluxes for our sample as a function of projected distance from the nucleus using the line analysis procedure described in the previous section, with the entire sample available online. Lines measured using G430L, G430M, or G750M gratings are marked as green diamonds, blue circles, and red squares respectively.

From the observed radial velocities, we have classified the kinematics of each AGN as Outflows, Ambiguous, Complex, and Compact. Kinematic classifications for our entire sample, as described below and shown in Figure 3, are listed in Table 5.

Within the expanded sample, we found 12 additional AGN (including Mrk 34 in Figures 2 and 3; top) that clearly show kinematics that are characteristic of biconical outflows seen in our previously modeled targets, and are thus classified as "Outflow" kinematic targets. AGN with Outflow kinematics required multiple outflow components, sets of velocities that increase out to a certain radius before decelerating back to systemic velocity, to be visible to fit our current model. Outflow targets ideally display four components, from the near and far sides of each cone, but can possibly be observed with only two as discussed in Section 5. We do not define all outflows that originate from AGN by these parameters, as it is possible to have an outflow that does not exhibit decelerating velocities (Fischer et al. 2010). High radial velocities also were ideal as they discount the likelihood that the observed kinematics could be due to rotation, where v is rarely greater than 400 km s^{-1} (Sparke & Gallagher 2000).

The remaining 36 AGN within the sample do not show distinct Outflow characteristics. The sources of their kinematics remain unclear, and it is possible that their NLR kinematics may be due to processes other than biconical AGN outflows. 17 AGN show kinematics that we have deemed "Ambiguous" (Figure 3; middle). Targets displaying these kinematics have a symmetrical component on each side of the nucleus traveling in opposite directions in velocity space. While some of these targets have kinematics that partially resemble those of Outflow AGN, it is unclear, or ambiguous, if these components possibly correspond to symmetrical sides in each half of a NLR bicone. As many exhibit low velocities and do not decelerate after a certain distance, they could also be due to rotation within the host disk (Sparke & Gallagher 2000; Müller-Sánchez et al. 2011) or some other factor not incorporated into our current model. Even with confirmation that the kinematics were half of an outflowing system, with their adjacent components either too faint or too compact to detect, we would be unable to create a successful kinematic model as the components are not adjacent to one another (as mentioned in Section 5).

Six additional targets show knotty, turbulent “Complex” kinematics (Figure 3; bottom) that reside near systemic velocity, containing large gradients in velocity possibly caused by in situ acceleration (similar to those in Mrk 573; Fischer et al. 2010). These targets show no signs of and cannot be explained by Outflow kinematics, though some exhibit signs of rotation.

There are 12 targets that do not contain enough data points in their kinematic plots to fit a model, and their kinematics are simply defined as “Compact”. A majority of these contain highly blueshifted velocities without corresponding redshifted velocities near the nucleus, suggesting outflow that cannot be resolved into individual components. Additionally, two targets, Mrk 348 and NGC 5347, were also deemed Compact as they were observed with the slit position outside the extended NLR, thus only detecting the nucleus emission. As the kinematics do not meet the criteria mentioned above to qualify as outflow kinematics, it is again possible that the observed velocities seen in this kinematic classification may be due to other processes. Finally, NGC 4303 cannot be modeled as we do not detect its NLR. Observations contain only continuum emission and no [O III] lines are clearly present.

5. Models

The kinematic models generated to match the observations are simple, yet give good fits to radial velocities for both Seyfert 1s and 2s showing outflows. This simple approach stems from four basic assumptions concerning the characteristics of the NLR clouds:

- 1) The model employs a biconical geometry for the NLR, with both cones being identical. This geometry best explains how [O III] images often show axisymmetric, triangular NLRs for Seyfert 2s and compact circular or elliptical NLRs for Seyfert 1s, consistent with the unified model (Schmitt et al. 2003).
- 2) The model assumes that the biconical geometry is due to the illumination from the nucleus surrounded by a torus-like structure of optically thick material. Thus, the apex of the bicone originates at the nucleus of the AGN (i.e. the SMBH). The apex is assumed to be sharp, but this is not always the case (Schmitt et al. 2003).
- 3) The model assumes a filling factor of 1 within the hollow bicone geometry and 0 outside, as we do not know the location of a cloud along our LOS through the bicone shell. This assumption gives a range of velocities along any LOS that a cloud can occupy. We assume that there is no absorption of this line within the bicone by the gas because the majority of our analysis is based on a forbidden line, although dust could possibly absorb some of this emission (Kraemer et al. 2011).

4) The model assumes that the bicone edges are sharp. Thus, the inner and outer opening angles define edges of ionized gas. However, in reality, the observed bicone often has fuzzy edges (Kraemer & Crenshaw 2000; Kraemer et al. 2008), but this has little effect on our results, as discussed later. The model also assumes a sharp edge on each end of the bicone defined by its total length, so that the model does not apply to clouds at greater distances.

The kinematic models used in this study are generated in a 3-dimensional geometry that depends on some basic input parameters. These parameters are listed in Table 4 and shown as a cartoon in Figure 4 as reference. The position angle ($P.A.$) is the angle between North and the bicone axis in the plane of the sky, measured in the eastward (counter-clockwise) direction. The inclination (i) of the bicone is measured out of the plane of the sky, with $i = 0$ placing the bicone axis in the plane of the sky and $i = 90$ placing the bicone axis along our line of sight. The inner and outer opening angles ($\theta_{min}, \theta_{max}$) are given as half of the total opening angles, measured from the bicone axis to the given opening angle. The maximum velocity (v_{max}) is the boundary value set in the velocity law $v = kr$, where the knots accelerate out (as a result of radiation pressure, for example) to a distance where the maximum velocity is reached before deceleration occurs. The maximum height (z_{max}) is the distance from the nucleus to one end of the bicone, measured along the bicone axis. The turnover radius (r_t) is the specific distance where clouds are no longer accelerated and begin to decelerate back to systemic velocity (due to, for example, gravitational or drag forces).

As mentioned in Section 1, the kinematic model used in this work originated in the Crenshaw & Kraemer (2000) study where the code generated a two-dimensional velocity map and sampled the map with a slit that matched the position, orientation, and width of an observed slit. The kinematic modeling code has since been updated, as described in Das et al. (2005), to produce a three-dimensional velocity cube which is sampled by extracting a two-dimensional sub-array corresponding to an *HST* STIS observation slit position, orientation, and width that contains all the radial velocity values within that slit. Long-slit extraction from the kinematic model results in a plot of radial velocity versus distance from the nucleus with up to four components. The model components have a width determined by $\theta_{max} - \theta_{min}$, which results in envelopes of shaded regions in the plots.

This model allows for different velocity laws of the form $v = kr^n$ at $r \leq r_t$ (turnover radius) and $v = v_{max} - kr^n$ at $r > r_t$. We found that the linear form was sufficient as the resultant models fit the data better than the other laws in general.

Model parameters are initially set to observed values, taken from imaging ($z_{max}, \theta_{max}, P.A.$) and the kinematics data (v_{max}, r_t). By creating a model parameter set and extracting slit positions corresponding to all observational positions for a particular galaxy, we can compare the two-dimensional model velocity extractions to the data simultaneously. The

comparison is done by eye as we have found no efficient statistical algorithm to compare the model and data. For example, expanding the width of the cone ($\theta_{max} - \theta_{min}$) will always include more observed velocities within the modeled velocity space and result in a lower χ^2 , but more empty space in the kinematic plot is also included. The process of model fitting is as follows:

- 1) The best fit model parameters are obtained when a model encloses the maximum amount of data points within a minimum shaded region (i.e. minimum difference between θ_{min} and θ_{max} , effects shown in Figures 5 and 6) and also matches the trend of increasing and decreasing velocity in the data reasonably well.
- 2) Input parameters cannot change across individual slits, as models must be consistent for all slits for each galaxy. Additionally, each of the two cones must be identical in terms of their model parameters.
- 3) The shaded regions in the models should not necessarily contain all data points, because some points are likely not in the NLR (e.g. they may be in the host galaxy) and thusly are not incorporated in the bicone geometry. Furthermore, it is clear that many emission-line knots have their own peculiar velocities with respect to the general flow. Emphasis is placed on the higher flux emission-line knots, which generally followed a more structured curve.
- 4) If a fit is not suitable for the given data, the parameters are intuitively adjusted in an iterative process. The most important parameter is the inclination of the bicone axis as it relates to the Seyfert type and has the greatest influence on the position of the model components that are compared to the data. Thus, a frequent course of action is to vary the inclination (Figures 7 and 8) and then make adjustments to the rest of the parameters to offset any resulting changes. Model generation, slit extraction, and plotting are repeated until an acceptable match to the data is determined. A suitable fit must account for most velocities and have a geometry that agrees with imaging.
- 5) Errors for a fit are defined as a range of values over which each individual parameter can vary without significantly altering the fit between model and data. For example, we can typically vary i by $\pm 5^\circ$ while maintaining a good fit.

We do not require our kinematic model to agree with the unified model. Should kinematics of an AGN be fit with two individual parameter sets that are inclined perpendicular to one another (i.e. a Type 1 vs Type 2 scenario), our model is constrained by available [O III] imaging and the parameter set that best matches the NLR morphology is chosen. Successfully fitting a kinematic model to the velocity data does not require information from all four components. Only two adjacent components (i.e. two components from the same cone or two components closest to Earth) are required in order to see the effects of changing

any of the model parameters. This means that a model can be obtained for targets that suffer from extinction via the host disk, which can obscure large portions of the NLR. Without adjacent components, it is impossible to solve for a single model as the combination of one inclination with a multitude of opening angles (and vice versa) would form solutions matching the available kinematic data, which provides the main reason why "Ambiguous" kinematics targets remain unmodeled.

A final parameter in determining the fit of a model is the interaction between the NLR and the host disk. Adding the geometry of the host disk to that of the NLR allows us to check the compatibility of the kinematic model with available imaging. Imaging that depicts a single cone of emission, for example, must be compatible with a kinematic model that both fits the spectral data and places one cone of the NLR outflow behind the host disk ¹. Disk inclinations and position angles for the host galaxy of each modeled AGN are listed from the literature in Table 6 and were generally determined by fitting isophotes to the host disk (Schmitt & Kinney 2000). Kinney et al. (2000) chose isophotes corresponding to a surface brightness level of 24-25 B mag arcsec⁻², which is often deep enough to avoid bar and oval distortion problems. Assuming a circular host galaxy disk, inclinations were determined from the measured ellipticity. Errors for inclination and P.A. range between 1° – 2° and 2° – 6° respectively. When it was not predetermined from imaging which side of the inclined disk was closer to Earth, orientations that most favorably agreed with the observed NLR geometry were employed.

6. Model Results

The resultant models for each "Outflow" AGN are detailed in Appendix A, with the final parameter values of each modeled AGN, including the five previously observed AGN, listed in Table 6. When comparing properties of our 17 successfully modeled versus the remaining unsuccessfully modeled AGN, we find no bias in the ability to model the kinematics due to Seyfert type (35% of Seyfert 1s; 37% of Seyfert 2s).

In Figures 9 and 10 we show the distribution of AGN polar angles ($= 90^\circ - i$, or the angle between the bicone axis and our LOS) and opening angles respectively of our modeled sample. Note that while our sample size is small, it covers a full range in both inclination and opening angle. The distribution of polar angles shows a trend of Seyfert 1s having smaller inclinations from our line of sight and Seyfert 2s being more inclined, in nearly complete agreement with the unified model of AGN. The sole exception to this trend is the

¹In some observed cases, there is not enough dust in the disk to obscure the NLR behind it.

inclination of NGC 5506, a Seyfert 1.9 with an inclination near the plane of the sky, which we discuss later. The distribution of half-opening angles show Seyfert 1s and Seyfert 2s have no preference for specific angles, in further agreement with the unified model. The broad range of opening angles points to differences in the inner torus-like geometry surrounding each AGN.

Table 6 also gives position angles and inclinations of each host galaxy disk required for our geometric models, as well as the angle between the NLR bicone axis and the normal to the host galaxy disk (β). The distribution of these β values, even within type 1 and 2 subsets (Figure 11), shows such diversity that no alignment of the NLR is seen relative to the host disk. These observations concur with previous studies (Schmitt et al. 1997; Clarke et al. 1998; Kinney et al. 2000; Schmitt et al. 2003) that compared the P.A. of the projected NLR to the P.A. of the host galaxy major axis and found that the distribution of their differences was homogeneous. Alignment between [O III] NLR and radio jet emission implies that the axes of the toroidal structure surrounding the AGN and the accretion disk contained within are relatively well aligned, with some exceptions (Schmitt et al. 2003). Thus, our β angle distribution suggests that the orientation of the gas in the inner torus is controlled more by the central SMBH than the galactic disk.

7. Discussion

While star-formation is a common feature amongst Seyfert galaxies (Cid Fernandes et al. 2004; Sarzi et al. 2007; Davies et al. 2007; Kauffmann & Heckman 2009), it remains unclear how much this process contributes to the kinematics using lines associated with the NLR in our AGN sample. Thus, it is possible that star formation may instigate or contribute to outflows in some AGN. We have therefore limited our identification of AGN-driven outflows to those that show the characteristic acceleration/deceleration signature, identified in our previous studies of AGN, with little or no nuclear star formation (Meléndez et al. 2008).

Excluding the 5 AGN with published results and the two galaxies from Ruiz et al. (2005), the remaining ten AGN in Table 6 have $P.A._{slit} = P.A._{bicone}$ within an error $< 10^\circ$, with the exception of Mrk 279 and the long-slit observation of NGC 5643, having differences of $\sim 30^\circ$ and $\sim 50^\circ$ respectfully. However, using value estimates from Schmitt & Kinney (1996) and Schmitt et al. (2003), the position angle of the NLR axis in [OIII] imaging, $P.A._{[O\ III]}$, is only equal to $P.A._{bicone}$ in 5 AGN (Circinus, Mrk 34, Mrk 1066, NGC 4507 and NGC 7674). In three galaxies (NGC 3227, NGC 3783 and NGC 4051), the difference between $P.A._{[O\ III]}$ and $P.A._{bicone}$ is $\sim 15^\circ$, and in Mrk 279 the difference is greater than 50° degrees. It is not possible to do this comparison in NGC 1667 due to the lack of [OIII]

images for this AGN, as mentioned in Section A.5. This relationship, or lack thereof, is highly dependent on the ability to identify the [OIII] PA in the imaging. The 5 AGN that have small differences between $P.A.[O\ III]$ and $P.A.bicone$ are the Seyfert 2s of the sample with extended, well resolved NLRs. The remaining 4 AGN with larger differences between position angles are all Seyfert 1 AGN that contain compact elliptical or circular NLRs. These NLRs prove much more difficult to fit with a position angle, as no conical structure is visible and we are sometimes forced to rely on a single asymmetric, extended knot of emission to provide guidance. Assuming the morphology of these Sy1 NLRs are due to the orientation of their biconical NLR lying along our line of sight, these extensions may only be bright knots of emission (similar to Mrk 78; Fischer et al. 2011) within the otherwise radially symmetric NLR.

While determining inclinations for a portion of the overall AGN sample is encouraging, a question now presents itself as to why we cannot model the remaining 35 AGN in our sample. One answer is poor positioning of the STIS long-slit. It is clear that four AGN with both [O III] spectra and imaging, Mrk 348, NGC 3081, NGC 5252, and NGC 5347 (Compact, Complex, Ambiguous, and Compact kinematics respectively) have long-slit positions that are not optimally placed inside the bicone region. Ground-based [O III] imaging (Mulchaey et al. 1996) of NGC 1358 and NGC 2110 (both Ambiguous kinematics) and pre-COSTAR *HST* WFPC (Schmitt & Kinney 1996) and OASIS IFU (Stoklasová et al. 2009) [O III] imaging of NGC 5929 also show a misalignment between NLR and STIS slit. OSIRIS IFU observations of NGC 7469 (Müller-Sánchez et al. 2011), which in *HST* [O III] imaging appears to have a circular NLR, show that [Si VI] NLR kinematics have the highest velocities along a position angle of $\sim 90^\circ$ which is misaligned with the *HST* STIS slit position by $\sim 65^\circ$. In addition, five "Ambiguous" AGN (IC 3639, Mrk 493, NGC 5283, NGC 7682, UM 146) and three "Complex" AGN (NGC 5427, NGC 5695, NGC 6300) may also have observations where the slit position is misaligned with their NLR, however this cannot be confirmed due to a lack of [O III] images for these targets.

Biconical outflow may still exist in a portion of the remaining targets if the required kinematic components for our models are not visible because they are too compact, faint, or convolved with other components like rotation. Developing a rotational kinematic model to fit the Ambiguous and Complex AGN spectra (Barbosa et al. 2009; Müller-Sánchez et al. 2011; Riffel & Storchi-Bergmann 2011) could provide insight on the true source of their kinematics as fitting and removing all AGN exhibiting rotational kinematics would allow us to search for possible remaining outflow components in the remaining AGN. As these data already exist, improving our models will be the most effective way to illuminate NLR kinematics moving forward without needing additional observations. AGN with truly Compact NLRs have a more clear cut dilemma: with high NLR velocities only observed in less than

a 0.5" diameter over the nucleus, we simply do not have enough spectral data to attempt fitting individual kinematic components.

8. Conclusions

We have measured radial velocities across NLRs for 47 Seyfert AGN observed with *HST*/STIS G430L/M gratings and combined these with our published measurements of 5 Seyferts with outflows. From our measurements, we found an additional 12 AGN that contained kinematics characteristic of biconical AGN outflow. Comparing the inclination of the NLR outflow to the normal of the host disk to calculate a β angle, we found a distribution that suggests that the orientation of the gas in the torus and that of the host disk are independent from one another.

With inclinations and geometries of 17 Seyfert galaxies, our model results agree with the unified model in that Seyfert 1 AGN are inclined further toward our LOS than Seyfert 2 AGN, save for the NLS1 NGC 5506 (Section A.10). Modeling the kinematics of this AGN results in a NLR cone inclined 10° from the plane of the sky. This contrasts with the unified model as the torus of absorbing material should obscure the BLR emission from our LOS at this orientation. As the host galaxy of this AGN is highly inclined (76°), it is possible that obscuration from the host disk is extinguishing regions of extended emission and that we are only modeling what remains of the NLR. Additionally, we have determined a correlation between i and neutral hydrogen column density (N_H) (Fischer et al. in prep) where AGN observed further from their NLR axis and closer to the obscuring torus are observed to have larger column densities. NGC 5506 has an N_H orders of magnitude lower than all other AGN at high inclinations, implying that it should have an inclination closer to our LOS.

Similar to observations of Mrk 3 and Mrk 573, multiple observed NLRs (IRAS 11058-1131, Mrk 34, NGC 3393, NGC 3516, NGC 5252) have morphologies consistent with intersections between the NLR ionizing radiation and the host disk (Mulchaey et al. 1996). It is likely that for these targets, the emitting gas did not originate in the nucleus of the AGN, but rather it was accelerated off the host disk. Does NLR emitting gas primarily originate in the nucleus or is it mainly due to in situ acceleration? Perhaps the NLR results primarily from a stream of ionizing radiation unleashed upon the galaxy, ionizing and accelerating ambient material that it encounters? The NLR in Circinus, which is nearly perpendicular to the host galaxy, is only 35 pc in height. As our own Milky Way has a scale height of less than 100 pc, we could be seeing the matter-bounded ionization of an abnormally rich (Freeman et al. 1977) host disk above the AGN.

Knowing the inclinations of AGN will allow us to determine how their observed properties vary as a function of polar angle with respect to the accretion disk and/or torus axes. As our technique for determining inclinations of AGN is not a simple task, correlating inclination with parameters that are more easily observable could provide astronomers a way to estimate the inclination of an AGN without modeling its NLR kinematics. Thus, the motivation for future study then is to expand beyond our current results by 1) determining the inclinations of the NLRs in a much larger sample of AGN, and 2) determining the multi-wavelength properties of these AGN to identify correlations that will probe the structure of the AGN components.

TCF thanks M.C. Bentz, H.R. Miller, R.J. White, and P.J. Wiita for the useful discussions, and the anonymous referee for their practical suggestions. Some of the data presented in this paper were obtained from the Mikulski Archive for Space Telescopes (MAST). STScI is operated by the Association of Universities for Research in Astronomy, Inc., under NASA contract NAS5-26555. This research has also made use of the NASA/IPAC Extragalactic Database (NED) which is operated by the Jet Propulsion Laboratory, California Institute of Technology, under contract with the National Aeronautics and Space Administration.

Table 1. *HST*/STIS Grating Specifications

Grating	Spectral Range (Å)		Target Line	Resolving Power ($\lambda/\Delta\lambda$)	Resolving Power (km s ⁻¹ FWHM)	σ_{hi}^c (Å)	σ_{noise}^b (Å)	σ_{total}^c (Å)	σ_{total} (km s ⁻¹)
	Complete	Per Tilt							
G430L	2900-5700	2800	[O III] λ 5007	~900	~330	0.26	0.79	0.83	49.7
G430M	3020-5610	286	[O III] λ 5007	~9000	~30	0.11	0.13	0.17	10.2
G750M	5450-10,140	570	H α λ 6563	~5900	~50	0.07	0.34	0.35	20.9

^aMaximum error due to fitting a Gaussian to an emission line

^bMaximum error due to noise

^cTotal Maximum error

Table 2:: Expanded Sample: *HST*/STIS Observations

Target	STScI Data Set	Source	Date (UT)	Grating	Aperture	Central λ (\AA)	P.A. (deg)	Offset (arcsec)	Exp. (s)
Akn 564	OBGU08010	C	2011 Jul 31	G430M	52 \times 0.2	5093	159.65	0.0	695
	OBGU08010	C	2011 Jul 31	G430M	52 \times 0.2	5093	159.65	0.0	695
	OBGU08010	C	2011 Jul 31	G430M	52 \times 0.2	5093	159.65	0.0	695
Circinus	O65B01040	A	2000 Oct 12	G430M	52 \times 0.2	4961	113.65	-0.6	1400
	O65B01050	A	2000 Oct 12	G430M	52 \times 0.2	4961	113.65	-0.4	1443
	O65B01060	A	2000 Oct 12	G430M	52 \times 0.2	4961	113.65	-0.2	1400
	O65B01070	A	2000 Oct 12	G430M	52 \times 0.2	4961	113.65	0.0	1495
	O65B01080	A	2000 Oct 12	G430M	52 \times 0.2	4961	113.65	+0.2	1400
	O65B01090	A	2000 Oct 12	G430M	52 \times 0.2	4961	113.65	+0.4	1492
	O65B03020	A	2002 Jan 04	G750M	52 \times 0.2	6581	-145.35	0.0	2120
	O65B03020	A	2002 Jan 04	G750M	52 \times 0.2	6581	-145.35	0.0	2120
IC 3639	O6BU01010	A	2002 Jan 23	G750M	52 \times 0.2	6581	-104.41	0.0	1080
	O6BU01020	A	2002 Jan 23	G750M	52 \times 0.2	6581	-104.41	0.0	1158
	O6BU01030	A	2002 Jan 23	G750M	52 \times 0.2	6581	-104.41	0.0	900
	O6BU01040	A	2002 Jan 23	G430L	52 \times 0.2	4300	-104.41	0.0	840
	O6BU01050	A	2002 Jan 23	G430L	52 \times 0.2	4300	-104.41	0.0	823
IRAS 11058	O56C03050	A	1999 Apr 08	G430L	52 \times 0.2	4300	36.03	0.0	600
MCG-6-30-15	O5GU08010	A	2000 Mar 07	G430M	52 \times 0.2	4961	-75.02	0.0	1707
	O5GU08020	A	2000 Mar 07	G430M	52 \times 0.2	4961	-75.02	0.0	2511
	O5GU08030	A	2000 Mar 07	G430M	52 \times 0.2	4961	-75.02	+0.2	1250
	O5GU08040	A	2000 Mar 07	G430M	52 \times 0.2	4961	-75.02	+0.2	1192
	O5GU08050	A	2000 Mar 07	G430M	52 \times 0.2	4961	-75.02	-0.2	1250
	O5GU08060	A	2000 Mar 07	G430M	52 \times 0.2	4961	-75.02	-0.2	1189
Mrk 34	O5G404010	A	2000 Feb 17	G430M	52 \times 0.2	5216	152.48	0.0	1500
	O5G404010	A	2000 Feb 17	G430L	52 \times 0.2	4300	152.48	0.0	627

Continued on next page

Table 2 Continued from previous page

Target	STScI Data Set	Source ^a	Date (UT)	Grating	Aperture	Central λ (Å)	P.A. (deg)	Offset ^b (arcsec)	Exposure (s)
	O5G404010	A	2000 Feb 17	G430M	52×0.2	5216	152.48	+0.28	1460
	O5G404010	A	2000 Feb 17	G430M	52×0.2	5216	152.48	-0.28	1460
Mrk 279	OBGU05010	C	2011 May 10	G430M	52×0.2	5093	124.65	0.0	712
	OBGU05020	C	2011 May 10	G430M	52×0.2	5093	124.65	0.0	712
	OBGU05030	C	2011 May 10	G430M	52×0.2	5093	124.65	0.0	712
Mrk 348	O5G405010	A	1999 Sep 28	G430M	52×0.2	5093	145.98	0.0	1410
	O5G405020	A	1999 Sep 28	G430L	52×0.2	4300	145.98	0.0	600
Mrk 463e	O5G406010	A	2000 Mar 14	G430M	52×0.2	5216	-178.03	0.0	1200
	O5G406020	A	2000 Mar 14	G430L	52×0.2	4300	-178.03	0.0	556
Mrk 493	O92X16010	A	2004 Jul 28	G430L	52×0.2	4300	74.65	0.0	720
	O92X16020	A	2004 Jul 28	G430L	52×0.2	4300	74.65	0.0	720
	O92X16030	A	2004 Jul 28	G430L	52×0.2	4300	74.65	0.0	720
Mrk 509	OBGU07010	C	2011 Aug 07	G430M	52×0.2	5093	74.65	0.0	695
	OBGU07020	C	2011 Aug 07	G430M	52×0.2	5093	74.65	0.0	695
	OBGU07030	C	2011 Aug 07	G430M	52×0.2	5093	74.65	0.0	695
Mrk 705	OB1105010	B	2010 Dec 10	G430M	52×0.1	5093	-100.35	0.0	2148
	OB1106010	B	2011 Feb 10	G430M	52×0.1	5093	7.92	0.0	2148
Mrk 766	OB1101010	B	2010 Mar 21	G430M	52×0.1	5093	129.65	0.0	2148
	OB1102010	B	2010 Dec 23	G430M	52×0.1	5093	-120.35	0.0	2148
Mrk 1040	OB1103010	B	2009 Jul 02	G430M	52×0.1	5093	-144.20	0.0	2148
	OB1104010	B	2009 Nov 14	G430M	52×0.1	5093	119.65	0.0	2148
Mrk 1044	OBGU01010	C	2011 Nov 06	G430M	52×0.2	5093	-36.23	0.0	695
	OBGU02010	C	2011 Nov 06	G430M	52×0.2	5093	-36.23	0.0	695
	OBGU03010	C	2011 Nov 06	G430M	52×0.2	5093	-36.23	0.0	695
Mrk 1066	O5G407010	A	2000 Oct 30	G430M	52×0.2	4961	130.65	0.0	1440

Continued on next page

Table 2 Continued from previous page

Target	STScI Data Set	Source ^a	Date (UT)	Grating	Aperture	Central λ (Å)	P.A. (deg)	Offset ^b (arcsec)	Exposure (s)
NGC 1358	O5G407020	A	2000 Oct 30	G430L	52×0.2	4300	130.65	0.0	600
	O6BU03010	A	2002 Jan 25	G750M	52×0.2	6581	23.89	0.0	1080
	O6BU03020	A	2002 Jan 25	G750M	52×0.2	6581	23.89	0.0	1080
	O6BU03030	A	2002 Jan 25	G750M	52×0.2	6581	23.89	0.0	840
	O6BU03040	A	2002 Jan 25	G430L	52×0.2	4300	23.89	0.0	840
NGC 1386	O6BU03050	A	2002 Jan 25	G430L	52×0.2	4300	23.89	0.0	805
	O5F402030	D	2000 Jun 23	G430M	50CCD	4961	175.82	0.0	2106
NGC 1667	O6BU04010	A	2001 Oct 14	G750M	52×0.2	6581	-120.21	0.0	1080
	O6BU04020	A	2001 Oct 14	G750M	52×0.2	6581	-120.21	0.0	1080
	O6BU04030	A	2001 Oct 14	G750M	52×0.2	6581	-120.21	0.0	840
	O6BU04040	A	2001 Oct 14	G430L	52×0.2	4300	-120.21	0.0	840
NGC 2110	O6BU04050	A	2001 Oct 14	G430L	52×0.2	4300	-120.21	0.0	805
	O5G401010	A	2000 Dec 24	G430M	52×0.2	4961	-36.20	0.0	1522
	O5G401020	A	2000 Dec 24	G430M	52×0.2	4961	-36.20	+0.68	600
	O64F02010	A	2000 Dec 30	G750M	52×0.2	6581	-24.35	0.0	1440
	O64F02020	A	2000 Dec 30	G750M	52×0.2	6581	-24.35	0.0	1440
NGC 2273	O64F02030	A	2000 Dec 30	G750M	52×0.2	6581	-24.35	0.0	1440
	O6BU05010	A	2001 Nov 04	G750M	52×0.2	6581	-151.61	0.0	1140
	O6BU05020	A	2001 Nov 04	G750M	52×0.2	6581	-151.61	0.0	1226
	O6BU05030	A	2001 Nov 04	G750M	52×0.2	6581	-151.61	0.0	900
	O6BU05040	A	2001 Nov 04	G430L	52×0.2	4300	-151.61	0.0	840
NGC 3081	O6BU05050	A	2001 Nov 04	G430L	52×0.2	4300	-151.61	0.0	951
	O6BU06010	A	2001 Dec 04	G750M	52×0.2	6581	-110.52	0.0	1080
	O6BU06020	A	2001 Dec 04	G750M	52×0.2	6581	-110.52	0.0	1080
	O6BU06030	A	2001 Dec 04	G750M	52×0.2	6581	-110.52	0.0	840

Continued on next page

Table 2 Continued from previous page

Target	STScI Data Set	Source ^a	Date (UT)	Grating	Aperture	Central λ (\AA)	P.A. (deg)	Offset ^b (arcsec)	Exposure (s)
	O6BU06040	A	2001 Dec 04	G430L	52 \times 0.2	4300	-110.52	0.0	840
	O6BU06050	A	2001 Dec 04	G430L	52 \times 0.2	4300	-110.52	0.0	812
NGC 3227	O57204010	A	1999 Jan 31	G750M	52 \times 0.2	6581	-137.62	-0.75	2105
	O57204020	A	1999 Jan 31	G750M	52 \times 0.2	6581	-137.62	-0.5	1600
	O57204030	A	1999 Jan 31	G750M	52 \times 0.2	6581	-137.62	-0.25	1884
	O57204040	A	1999 Jan 31	G750M	52 \times 0.2	6581	-137.62	0.0	1890
	O57204050	A	1999 Jan 31	G750M	52 \times 0.2	6581	-137.62	+0.25	1600
	O57204060	A	1999 Jan 31	G750M	52 \times 0.2	6581	-137.62	+0.5	1884
	O57204070	A	1999 Jan 31	G750M	52 \times 0.2	6581	-137.62	+0.75	1887
	O5KP01020	A	2000 Feb 08	G430L	52 \times 0.2	4300	-150.34	0.0	120
NGC 3393	O56C02010	A	1999 Apr 22	G750M	52 \times 0.2	6581	39.98	-0.3	1080
	O56C02030	A	1999 Apr 22	G750M	52 \times 0.2	6581	39.98	0.0	865
	O56C02040	A	1999 Apr 22	G750M	52 \times 0.2	6581	39.98	0.0	600
	O56C02050	A	1999 Apr 22	G430L	52 \times 0.2	4300	39.98	0.0	600
	O56C02060	A	1999 Apr 22	G750M	52 \times 0.2	6581	39.98	+0.3	1021
NGC 3516	O5F406030	D	2000 Jan 18	G430M	50CCD	5093	-154.98	0.0	2154
	O56C01050	A	2000 Jun 18	G430L	52 \times 0.2	4300	38.98	0.0	600
NGC 3783	OBGU03010	C	2011 Mar 23	G430M	52 \times 0.2	4961	-20.35	0.0	696
	OBGU03020	C	2011 Mar 23	G430M	52 \times 0.2	4961	-20.35	0.0	696
NGC 4051	O5G402010	A	2000 Apr 15	G430M	52 \times 0.2	4961	89.78	-0.05	1796
	O5G402020	A	2000 Apr 15	G430M	52 \times 0.2	4961	89.78	+0.2	600
NGC 4303	O6LC01010	A	2003 Mar 04	G430M	52 \times 0.2	4961	-140.35	0.0	2156
	O6LC01020	A	2003 Mar 04	G430L	52 \times 0.2	4961	-140.35	0.0	1200
NGC 4395	OBGU04010	C	2011 May 25	G430M	52 \times 0.2	4961	64.65	0.0	693
	OBGU04020	C	2011 May 25	G430M	52 \times 0.2	4961	64.65	0.0	693

Continued on next page

Table 2 Continued from previous page

Target	STScI Data Set	Source ^a	Date (UT)	Grating	Aperture	Central λ (\AA)	P.A. (deg)	Offset ^b (arcsec)	Exposure (s)
	OBGU04030	C	2011 May 25	G430M	52 \times 0.2	4961	64.65	0.0	693
NGC 4507	O5DF03010	A	2001 Apr 04	G430M	52 \times 0.2	4961	-34.35	0.0	1440
	O5DF03010	A	2001 Apr 04	G430L	52 \times 0.2	4300	-34.35	0.0	624
NGC 5135	O6BU07010	A	2002 Jan 11	G750M	52 \times 0.2	6581	-115.81	0.0	1080
	O6BU07020	A	2002 Jan 11	G750M	52 \times 0.2	6581	-115.81	0.0	1104
	O6BU07030	A	2002 Jan 11	G750M	52 \times 0.2	6581	-115.81	0.0	832
	O6BU07040	A	2002 Jan 11	G430L	52 \times 0.2	4300	-115.81	0.0	840
	O6BU07040	A	2002 Jan 11	G430L	52 \times 0.2	4300	-115.81	0.0	829
NGC 5252	O56C04010	A	1999 Jan 27	G750M	52 \times 0.2	6581	-135.52	-0.2	1080
	O56C04030	A	1999 Jan 27	G750M	52 \times 0.2	6581	-135.52	0.0	841
	O56C04040	A	1999 Jan 27	G750M	52 \times 0.2	6581	-135.52	0.0	600
	O56C04050	A	1999 Jan 27	G430L	52 \times 0.2	4300	-135.52	0.0	600
	O56C04060	A	1999 Jan 27	G750M	52 \times 0.2	6581	-135.52	+0.2	997
NGC 5283	O6BU08010	A	2001 Oct 11	G750M	52 \times 0.2	6581	-37.06	0.0	1200
	O6BU08020	A	2001 Oct 11	G750M	52 \times 0.2	6581	-37.06	0.0	1213
	O6BU08030	A	2001 Oct 11	G750M	52 \times 0.2	6581	-37.06	0.0	900
	O6BU08040	A	2001 Oct 11	G430L	52 \times 0.2	4300	-37.06	0.0	900
	O6BU08050	A	2001 Oct 11	G430L	52 \times 0.2	4300	-37.06	0.0	900
NGC 5347	O6BU09010	A	2001 Dec 24	G750M	52 \times 0.2	6581	-102.20	0.0	1080
	O6BU09020	A	2001 Dec 24	G750M	52 \times 0.2	6581	-102.20	0.0	1126
	O6BU09030	A	2001 Dec 25	G750M	52 \times 0.2	6581	-102.20	0.0	840
	O6BU09040	A	2001 Dec 25	G430L	52 \times 0.2	4300	-102.20	0.0	840
	O6BU09050	A	2001 Dec 25	G430L	52 \times 0.2	4300	-102.20	0.0	851
NGC 5427	O6BU10010	A	2002 Jan 04	G750M	52 \times 0.2	6581	-113.38	0.0	1080
	O6BU10020	A	2002 Jan 04	G750M	52 \times 0.2	6581	-113.38	0.0	1080

Continued on next page

Table 2 Continued from previous page

Target	STScI Data Set	Source ^a	Date (UT)	Grating	Aperture	Central λ (Å)	P.A. (deg)	Offset ^b (arcsec)	Exposure (s)
	O6BU10030	A	2002 Jan 04	G750M	52×0.2	6581	-113.38	0.0	840
	O6BU10040	A	2002 Jan 04	G430L	52×0.2	4300	-113.38	0.0	840
	O6BU10050	A	2002 Jan 04	G430L	52×0.2	4300	-113.38	0.0	805
NGC 5506	O5F407030	D	2000 Mar 18	G430M	50CCD	4961	-153.39	0.0	2096
NGC 5548	OBGU06010	C	2011 Mar 11	G430M	52×0.2	5093	-160.35	0.0	695
	OBGU06020	C	2011 Mar 11	G430M	52×0.2	5093	-160.35	0.0	695
	OBGU06030	C	2011 Mar 11	G430M	52×0.2	5093	-160.35	0.0	695
NGC 5643	O5F408030	D	2000 Feb 23	G430M	50CCD	4961	-99.98	0.0	2107
	O6BU11010	A	2000 Mar 12	G750M	52×0.2	6581	-128.04	0.0	1140
	O6BU11020	A	2000 Mar 12	G750M	52×0.2	6581	-128.04	0.0	1223
	O6BU11030	A	2000 Mar 12	G750M	52×0.2	6581	-128.04	0.0	900
	O6BU11040	A	2000 Mar 12	G430L	52×0.2	4300	-128.04	0.0	840
	O6BU11050	A	2000 Mar 12	G430L	52×0.2	4300	-128.04	0.0	868
NGC 5695	O6BU12010	A	2001 Aug 11	G750M	52×0.2	6581	50.65	0.0	1080
	O6BU12020	A	2001 Aug 11	G750M	52×0.2	6581	50.65	0.0	1158
	O6BU12030	A	2001 Aug 11	G750M	52×0.2	6581	50.65	0.0	900
	O6BU12040	A	2001 Aug 11	G430L	52×0.2	4300	50.65	0.0	840
	O6BU12050	A	2001 Aug 11	G430L	52×0.2	4300	50.65	0.0	823
NGC 5728	O5F409030	D	2000 Apr 24	G430M	50CCD	5093	-79.98	0.0	2110
NGC 5929	O5G403010	A	2000 Feb 07	G430M	52×0.2	4961	-134.62	0.0	1524
NGC 6300	O6BU13010	A	2001 Nov 08	G750M	52×0.2	6581	90.28	0.0	1140
	O6BU13020	A	2001 Nov 08	G750M	52×0.2	6581	90.28	0.0	1226
	O6BU13030	A	2001 Nov 08	G750M	52×0.2	6581	90.28	0.0	840
	O6BU13040	A	2001 Nov 08	G430L	52×0.2	4300	90.28	0.0	900
	O6BU13050	A	2001 Nov 08	G430L	52×0.2	4300	90.28	0.0	951

Continued on next page

Table 2 Continued from previous page

Target	STScI Data Set	Source ^a	Date (UT)	Grating	Aperture	Central λ (Å)	P.A. (deg)	Offset ^b (arcsec)	Exposure (s)
NGC 7212	O5F410030	D	2000 Jun 04	G430M	50CCD	5093	-174.98	0.0	2112
NGC 7469	OBGU09010	C	2010 Oct 05	G430M	52×0.1	5093	34.65	0.0	697
	OBGU09020	C	2010 Oct 05	G430M	52×0.1	5093	34.65	0.0	697
	OBGU09030	C	2010 Oct 05	G430M	52×0.1	5093	34.65	0.0	697
NGC 7674	O5DF04010	A	2000 Sep 12	G430M	52×0.2	5093	124.65	0.0	1140
	O5DF04020	A	2000 Sep 12	G430L	52×0.2	4300	124.65	0.0	600
NGC 7682	O6BU14010	A	2001 Oct 23	G750M	52×0.2	6581	17.85	0.0	1080
	O6BU14020	A	2001 Oct 23	G750M	52×0.2	6581	17.85	0.0	1080
	O6BU14030	A	2001 Oct 23	G750M	52×0.2	6581	17.85	0.0	840
	O6BU14040	A	2001 Oct 23	G430L	52×0.2	4300	17.85	0.0	840
	O6BU14050	A	2001 Oct 23	G430L	52×0.2	4300	17.85	0.0	805
NGC 788	O6BU15010	A	2001 Sep 17	G750M	52×0.2	6581	-129.56	0.0	1080
	O6BU15020	A	2001 Sep 17	G750M	52×0.2	6581	-129.56	0.0	1080
	O6BU15030	A	2001 Sep 17	G750M	52×0.2	6581	-129.56	0.0	840
	O6BU15040	A	2001 Sep 17	G430L	52×0.2	4300	-129.56	0.0	840
	O6BU15050	A	2001 Sep 17	G430L	52×0.2	4300	-129.56	0.0	805
UM 146	O6BU16010	A	2001 Dec 20	G750M	52×0.2	6581	21.33	0.0	1080
	O6BU16020	A	2001 Dec 20	G750M	52×0.2	6581	21.33	0.0	1080
	O6BU16030	A	2001 Dec 20	G750M	52×0.2	6581	21.33	0.0	840
	O6BU16040	A	2001 Dec 20	G430L	52×0.2	4300	21.33	0.0	840
	O6BU16050	A	2001 Dec 20	G430L	52×0.2	4300	21.33	0.0	805

^a**Sources:** (A) MAST Archive (B) HST Prop ID: 11611 (C) HST Prop ID: 12212 (D) Ruiz et al. (2005)

^bPerpendicular to the slit position

Table 3. AGN Distances *HST* Imaging Observations and Redshifts

Target	z	Source	Dist. Mpc	Ref.	Scale (pc $''$)	Type	Instr.	Filter
Akn 564	0.024684	21 cm	101.4	NED	491	1	WFC3	FQ508N
Circinus	0.001453	21 cm	4.2	EDD	20	2	WFPC2	F606W
IC 3639	0.010924	21 cm	44.9	NED	217	2	WFPC2	F606W
IRAS 11058-1131	0.054828	Stellar	225.2	NED	1092	2	WFPC2	F547M
MCG-6-30-15	0.007749	Stellar	25.5	EDD	123	1	WFPC2	FR533N
Mrk 34	0.051167	Stellar	210.1	NED	1019	2	WFPC2	FR533N
Mrk 279	0.030451	Stellar	125.1	NED	606	1	WFC3	FQ508N
Mrk 348	0.015034	21 cm	61.7	NED	299	2	WFPC2	FR533N
Mrk 463e	0.050000	—	205.3	NED	996	2	WFPC2	FR533N
Mrk 493	0.031485	21 cm	129.3	NED	627	1	WFPC2	F606W
Mrk 509	0.034397	Stellar	141.3	NED	685	1	WFC3	FQ508N
Mrk 705	0.029150	Stellar	119.7	NED	580	1	WFPC2	FR533N
Mrk 766	0.012929	Stellar	53.1	NED	257	1	WFPC2	FR533N
Mrk 1040	0.016642	21 cm	68.3	NED	331	1	WFPC2	FR533N
Mrk 1044	0.016451	21 cm	67.6	NED	328	1	WFC3	FQ508N
Mrk 1066	0.011858	Stellar	48.7	NED	236	2	WF/PC	F492M
NGC 1358	0.013436	21 cm	55.2	NED	268	2	WFPC2	F606W
NGC 1386	0.002895	Stellar	16.5	EDD	80	2	WFPC2	F502N
NGC 1667	0.015257	21 cm	62.7	NED	304	2	WFPC2	F606W
NGC 2110	0.007789	Stellar	29.0	EDD	140	2	WFPC2	F606W
NGC 2273	0.006138	21 cm	17.9	EDD	87	2	WFPC2	FR533N
NGC 3081	0.007988	21 cm	28.6	EDD	139	2	WFPC2	FR533N
NGC 3227	0.003859	21 cm	26.4	EDD	128	1	WFPC2	F606W
NGC 3393	0.012509	21 cm	51.4	NED	249	2	WFC3	FQ508N
NGC 3516	0.008836	Stellar	38.0	EDD	184	1	WFPC2	FR533N
NGC 3783	0.009730	21 cm	25.1	EDD	122	1	WFPC2	FR533N
NGC 4051	0.002418	21 cm	17.1	EDD	83	1	WFC3	F502N
NGC 4303	0.005234	21 cm	17.6	EDD	85	2	WFPC2	F606W
NGC 4395	0.001064	21 cm	4.7	EDD	23	1	WFC3	F502N
NGC 4507	0.011829	21 cm	48.6	NED	236	2	WFPC2	FR533N
NGC 5135	0.013693	21 cm	56.2	NED	273	2	WFPC2	F606W
NGC 5252	0.023093	21 cm	94.8	NED	460	1.9	WFPC2	FR533N
NGC 5283	0.010404	Stellar	42.7	NED	207	2	WFPC2	F606W
NGC 5347	0.007959	21 cm	39.0	EDD	189	2	WFPC2	FR533N
NGC 5427	0.008733	21 cm	27.0	EDD	131	2	WFPC2	F606W
NGC 5506	0.006084	21 cm	21.7	EDD	105	1	FOC	F501N
NGC 5548	0.017175	21 cm	70.5	NED	342	1	WFC3	FQ508N

Table 3—Continued

Target	z	Source	Dist. Mpc	Ref.	Scale (pc $''$)	Type	Instr.	Filter
NGC 5643	0.003999	21 cm	11.8	EDD	57	2	WFPC2	F502N
NGC 5695	0.014093	21 cm	57.9	NED	281	2	WFPC2	F606W
NGC 5728	0.009316	21 cm	24.8	EDD	120	2	WF/PC	F492M
NGC 5929	0.008543	21 cm	32.2	EDD	156	2	WFPC2	F606W
NGC 6300	0.003699	21 cm	13.1	EDD	64	2	WFPC2	F606W
NGC 7212	0.026001	Stellar	106.8	NED	518	2	WFPC2	FR533N
NGC 7469	0.016268	21 cm	66.8	NED	324	1	WFPC2	FR533N
NGC 7674	0.029030	21 cm	119.2	NED	578	2	WFPC2	FR533P15
NGC 7682	0.017140	21 cm	70.4	NED	341	2	WFPC2	F606W
NGC 788	0.013603	Stellar	55.9	NED	271	2	WFPC2	F606W
UM 146	0.017225	21 cm	70.7	NED	343	1.9	WFPC2	F606W

Table 4. Kinematic Model Parameter Abbreviations

Parameter	Symbol
Position angle of bicone axis ($^{\circ}$)	$P.A.$
Inclination of bicone axis ($^{\circ}$)	i
Outer opening angle ($^{\circ}$)	θ_{max}
Inner opening angle ($^{\circ}$)	θ_{min}
Maximum velocity (km s^{-1})	v_{max}
Bicone height (pc)	z_{max}
Turnover radius (pc)	r_t

Table 5. Total Sample AGN Kinematic Classifications

Type	Target		
<i>Outflow</i>	Circinus	Mrk 3	Mrk 34
	Mrk 78	Mrk 279	Mrk 573
	Mrk 1066	NGC 1068	NGC 1667
	NGC 3227	NGC 3783	NGC 4051
	NGC 4151	NGC 4507	NGC 5506
	NGC 5643	NGC 7674	
<i>Ambiguous</i>	Akn 564	IC 3639	MCG-6-30-15
	Mrk 493	Mrk 509	NGC 1358
	NGC 2110	NGC 2273	NGC 3516
	NGC 4395	NGC 5252	NGC 5283
	NGC 5728	NGC 5929	NGC 7682
	NGC 788	UM 146	
<i>Complex</i>	IRAS 11058-1131	NGC 1386	NGC 3081
	NGC 3393	NGC 5135	NGC 7212
<i>Compact</i>	Mrk 348	Mrk 463e	Mrk 705
	Mrk 766	Mrk 1040	Mrk 1044
	NGC 5347	NGC 5427	NGC 5548
	NGC 5695	NGC 6300	NGC 7469
<i>Poor</i>	NGC 4303		

Table 6. Total Sample Modeled AGN Parameters.¹

Target	NLR Bicone							Host Disk			β ² (°)
	<i>P.A.</i> (°)	<i>i</i> (°)	θ_{min} (°)	θ_{max} (°)	v_{max} (km/s)	z_{max} (pc)	r_t (pc)	<i>P.A.</i> (°)	<i>i</i> (°)	Disk Ref.	
Circinus	-52	25 (NW)	36	41	300	35	9	30	65	1	7
Mrk 3	89	05 (NE)	—	51	800	270	80	129	64	9	52
Mrk 34	-32	25 (SE)	30	40	1500	1750	1000	65	30	2	85
Mrk 78	65	30 (SW)	10	35	1200	3200	700	84	55	2	87
Mrk 279	-24	55 (SE)	59	62	1800	300	250	33	56	3,4	86
Mrk 573	-36	30 (NW)	51	53	400	1200	800	103	30	3,2	44
Mrk 1066	-41	10 (NW)	15	25	900	400	80	90	54	3	45
NGC 1068	30	05 (NE)	20	40	2000	400	140	115	40	8	45
NGC 1667	55	18 (NW)	45	58	300	100	60	5	39	4	46
NGC 3227	30	75 (SW)	40	55	500	200	100	-31	63	2,5	76
NGC 3783	-20	75 (SE)	45	55	130	110	32	-15	35	6	38
NGC 4051	80	78 (NE)	10	25	550	175	52	50	05	6	15
NGC 4151	60	45 (SW)	15	33	800	400	96	33	20	7	39
NGC 4507	-37	43 (NW)	30	50	1000	200	90	65	28	2	12
NGC 5506	22	10 (SW)	10	40	550	220	65	-89	76	3	32
NGC 5643	80	25 (SE)	50	55	500	285	70	136	30	3	42
NGC 7674	-63	30 (NW)	35	40	1000	700	200	76	40	2	42

¹Inclination direction specifies which end of the NLR bicone is inclined out of the plane of the sky toward Earth

²Angle between the NLR bicone axis and the normal to the host galaxy disk

References: (1) Freeman et al. (1977), (2) Schmitt & Kinney (2000), (3) Kinney et al. (2000), (4) NED, (5) Xilouris & Papadakis (2002), (6) Hicks et al. (2009), (7) Das et al. (2005), (8) Das et al. (2006), (9) Crenshaw et al. (2010)

REFERENCES

- Antonucci, R. 1993, *ARA&A*, 31, 473
- Antonucci, R. R. J., & Miller, J. S. 1985, *ApJ*, 297, 621
- Barbosa, F. K. B., Storchi-Bergmann, T., Cid Fernandes, R., Winge, C., & Schmitt, H. 2009, *MNRAS*, 396, 2
- Bower, G., Wilson, A., Morse, J. A., Gelderman, R., Whittle, M., & Mulchaey, J. 1995, *ApJ*, 454, 106
- Cid Fernandes, R., Gu, Q., Melnick, J., Terlevich, E., Terlevich, R., Kunth, D., Rodrigues Lacerda, R., & Joguet, B. 2004, *MNRAS*, 355, 273
- Clarke, C. J., Kinney, A. L., & Pringle, J. E. 1998, *ApJ*, 495, 189
- Crenshaw, D. M., & Kraemer, S. B. 2000, *ApJ*, 532, L101
- Crenshaw, D. M. et al. 2000, *AJ*, 120, 1731
- Crenshaw, D. M., Kraemer, S. B., Schmitt, H. R., Jaffé, Y. L., Deo, R. P., Collins, N. R., & Fischer, T. C. 2010, *AJ*, 139, 871
- Crenshaw, D. M. et al. 2002, *ApJ*, 566, 187
- Das, V. et al. 2005, *AJ*, 130, 945
- Das, V., Crenshaw, D. M., Kraemer, S. B., & Deo, R. P. 2006, *AJ*, 132, 620
- Davies, R. I., Müller Sánchez, F., Genzel, R., Tacconi, L. J., Hicks, E. K. S., Friedrich, S., & Sternberg, A. 2007, *ApJ*, 671, 1388
- Elitzur, M., & Shlosman, I. 2006, *ApJ*, 648, L101
- Fischer, T. C., Crenshaw, D. M., Kraemer, S. B., Schmitt, H. R., Mushotsky, R. F., & Dunn, J. P. 2011, *ApJ*, 727, 71
- Fischer, T. C., Crenshaw, D. M., Kraemer, S. B., Schmitt, H. R., & Trippe, M. L. 2010, *AJ*, 140, 577
- Freeman, K. C., Karlsson, B., Lynga, G., Burrell, J. F., van Woerden, H., Goss, W. M., & Mebold, U. 1977, *A&A*, 55, 445
- Greenhill, L. J. et al. 2003, *ApJ*, 590, 162

- Guainazzi, M., Bianchi, S., Matt, G., Dadina, M., Kaastra, J., Malzac, J., & Risaliti, G. 2010, MNRAS, 406, 2013
- Hicks, E. K. S., Davies, R. I., Malkan, M. A., Genzel, R., Tacconi, L. J., Müller Sánchez, F., & Sternberg, A. 2009, ApJ, 696, 448
- Ho, L. C., Filippenko, A. V., & Sargent, W. L. W. 1997, ApJ, 487, 568
- Hutchings, J. B. et al. 1998, ApJ, 492, L115
- Imanishi, M. 2000, MNRAS, 313, 165
- Kauffmann, G., & Heckman, T. M. 2009, MNRAS, 397, 135
- Khachikian, E. Y., & Weedman, D. W. 1974, ApJ, 192, 581
- Kinney, A. L., Schmitt, H. R., Clarke, C. J., Pringle, J. E., Ulvestad, J. S., & Antonucci, R. R. J. 2000, ApJ, 537, 152
- Kondratko, P. T., Greenhill, L. J., & Moran, J. M. 2006, ApJ, 652, 136
- Kraemer, S. B., & Crenshaw, D. M. 2000, ApJ, 544, 763
- Kraemer, S. B., Schmitt, H. R., & Crenshaw, D. M. 2008, ApJ, 679, 1128
- Kraemer, S. B., Schmitt, H. R., Crenshaw, D. M., Meléndez, M., Turner, T. J., Guainazzi, M., & Mushotzky, R. F. 2011, ApJ, 727, 130
- Maiolino, R., & Rieke, G. H. 1995, ApJ, 454, 95
- Malkan, M. A., Gorjian, V., & Tam, R. 1998, ApJS, 117, 25
- Meléndez, M., Kraemer, S. B., Schmitt, H. R., Crenshaw, D. M., Deo, R. P., Mushotzky, R. F., & Bruhweiler, F. C. 2008, ApJ, 689, 95
- Momjian, E., Romney, J. D., Carilli, C. L., & Troland, T. H. 2003, ApJ, 597, 809
- Morris, S., Ward, M., Whittle, M., Wilson, A. S., & Taylor, K. 1985, MNRAS, 216, 193
- Mulchaey, J. S., Wilson, A. S., & Tsvetanov, Z. 1996, ApJ, 467, 197
- Müller-Sánchez, F., Prieto, M. A., Hicks, E. K. S., Vives-Arias, H., Davies, R. I., Malkan, M., Tacconi, L. J., & Genzel, R. 2011, ApJ, 739, 69
- Nagar, N. M., Oliva, E., Marconi, A., & Maiolino, R. 2002, A&A, 391, L21

- Osterbrock, D. E., & Ferland, G. J. 2006, *Astrophysics of gaseous nebulae and active galactic nuclei*
- Osterbrock, D. E., & Pogge, R. W. 1987, *ApJ*, 323, 108
- Peterson, B. M. 1997, *An Introduction to Active Galactic Nuclei* (Cambridge University Press)
- Pogge, R. W. 1988, *ApJ*, 328, 519
- Pounds, K. A., Done, C., & Osborne, J. P. 1995, *MNRAS*, 277, L5
- Prieto, M. A., Marco, O., & Gallimore, J. 2005, *MNRAS*, 364, L28
- Riffel, R. A., & Storchi-Bergmann, T. 2011, *MNRAS*, 417, 2752
- Ruiz, J. R., Crenshaw, D. M., Kraemer, S. B., Bower, G. A., Gull, T. R., Hutchings, J. B., Kaiser, M. E., & Weistrop, D. 2001, *AJ*, 122, 2961
- . 2005, *AJ*, 129, 73
- Ruiz, M., Alexander, D. M., Young, S., Hough, J., Lumsden, S. L., & Heisler, C. A. 2000, *MNRAS*, 316, 49
- Sarzi, M., Allard, E. L., Knapen, J. H., & Mazzuca, L. M. 2007, *MNRAS*, 380, 949
- Schmitt, H. R., Donley, J. L., Antonucci, R. R. J., Hutchings, J. B., & Kinney, A. L. 2003, *ApJS*, 148, 327
- Schmitt, H. R., & Kinney, A. L. 1996, *ApJ*, 463, 498
- . 2000, *ApJS*, 128, 479
- Schmitt, H. R., Kinney, A. L., Storchi-Bergmann, T., & Antonucci, R. 1997, *ApJ*, 477, 623
- Schmitt, H. R., Storchi-Bergmann, T., & Baldwin, J. A. 1994, *ApJ*, 423, 237
- Simpson, C., Wilson, A. S., Bower, G., Heckman, T. M., Krolik, J. H., & Miley, G. K. 1997, *ApJ*, 474, 121
- Sparke, L. S., & Gallagher, III, J. S. 2000, *Galaxies in the universe : an introduction* (Cambridge University Press)
- Stoklasová, I., Ferruit, P., Emsellem, E., Jungwiert, B., Pécontal, E., & Sánchez, S. F. 2009, *A&A*, 500, 1287

- Trippe, M. L., Crenshaw, D. M., Deo, R. P., Dietrich, M., Kraemer, S. B., Rafter, S. E., & Turner, T. J. 2010, *ApJ*, 725, 1749
- Tully, R. B., Rizzi, L., Shaya, E. J., Courtois, H. M., Makarov, D. I., & Jacobs, B. A. 2009, *AJ*, 138, 323
- Ulvestad, J. S., Antonucci, R. R. J., & Goodrich, R. W. 1995, *AJ*, 109, 81
- Unger, S. W., Pedlar, A., Axon, D. J., Whittle, M., Meurs, E. J. A., & Ward, M. J. 1987, *MNRAS*, 228, 671
- Walsh, J. L., Barth, A. J., Ho, L. C., Filippenko, A. V., Rix, H.-W., Shields, J. C., Sarzi, M., & Sargent, W. L. W. 2008, *AJ*, 136, 1677
- Wilson, A. S., Shopbell, P. L., Simpson, C., Storchi-Bergmann, T., Barbosa, F. K. B., & Ward, M. J. 2000, *AJ*, 120, 1325
- Winter, L. M., Mushotzky, R. F., Reynolds, C. S., & Tueller, J. 2009, *ApJ*, 690, 1322
- Xilouris, E. M., & Papadakis, I. E. 2002, *A&A*, 387, 441

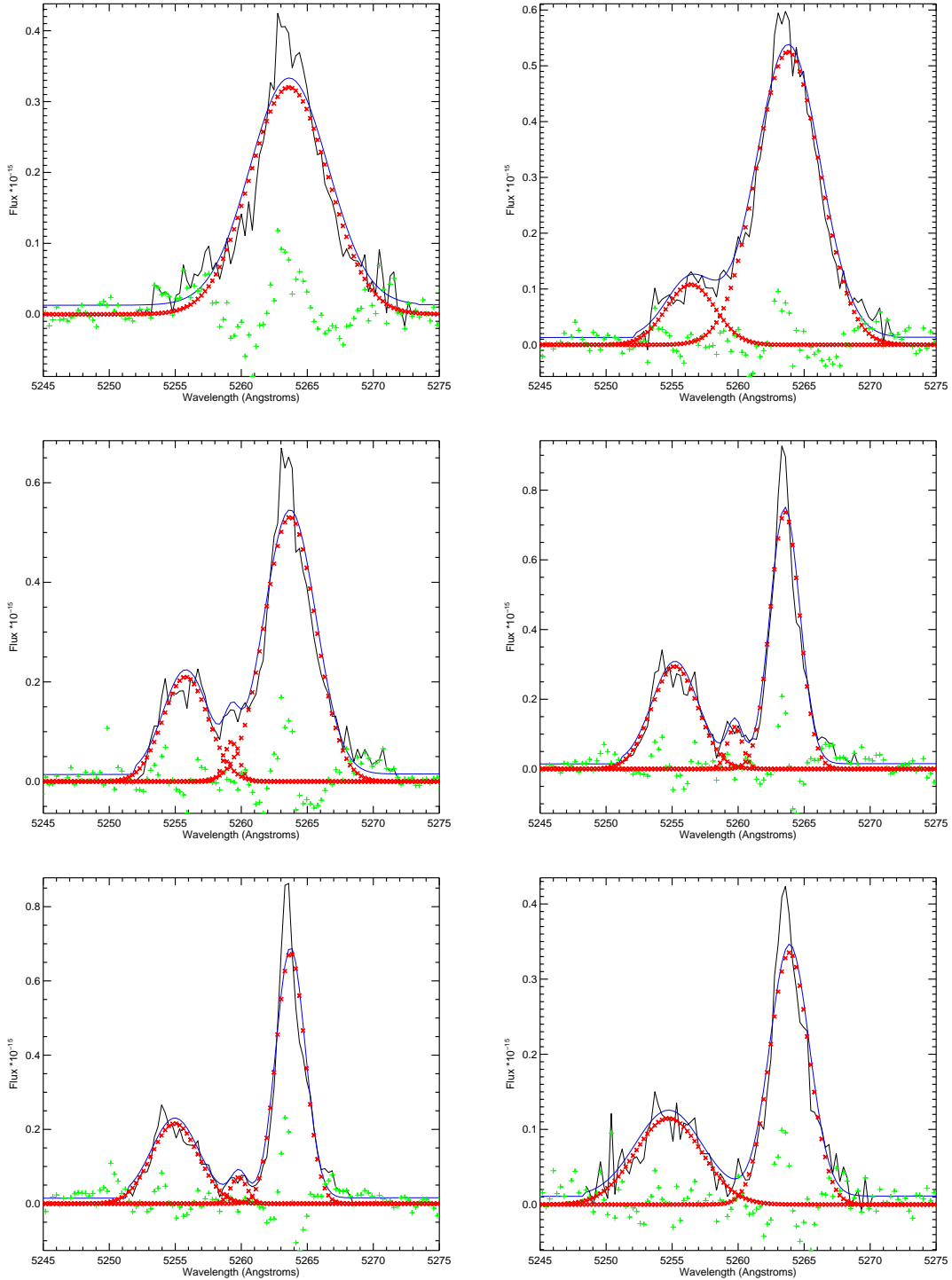


Fig. 1.— Spectra in black and fits in color showing the multicomponent Gaussian fits. The plots, ordered from left to right and top to bottom, are from positions separated by $0.05''$, increasing in distance from the nucleus. Red \times curves represent the Gaussian fit for each component, the blue line represent the model fit as the sum of the red curves and the average continuum, and green $+$ curves represent the difference between the black spectra and blue models. Spectra are not yet Doppler-corrected for the cosmological redshift of Mrk 34. Fluxes are in $\text{ergs s}^{-1} \text{cm}^{-2} \text{\AA}^{-1}$

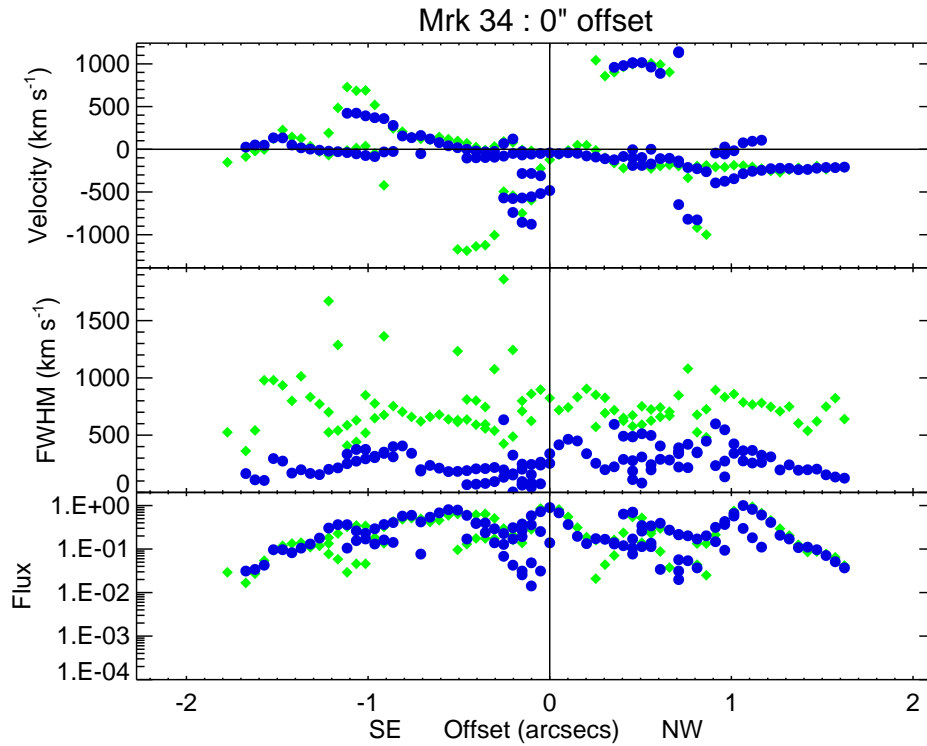


Fig. 2.— Radial velocities (top), FWHM (middle), and normalized fluxes (bottom) of [OIII] lines using the G430L (green diamonds) and G430M (blue circles) gratings for the central slit position of Mrk 34.

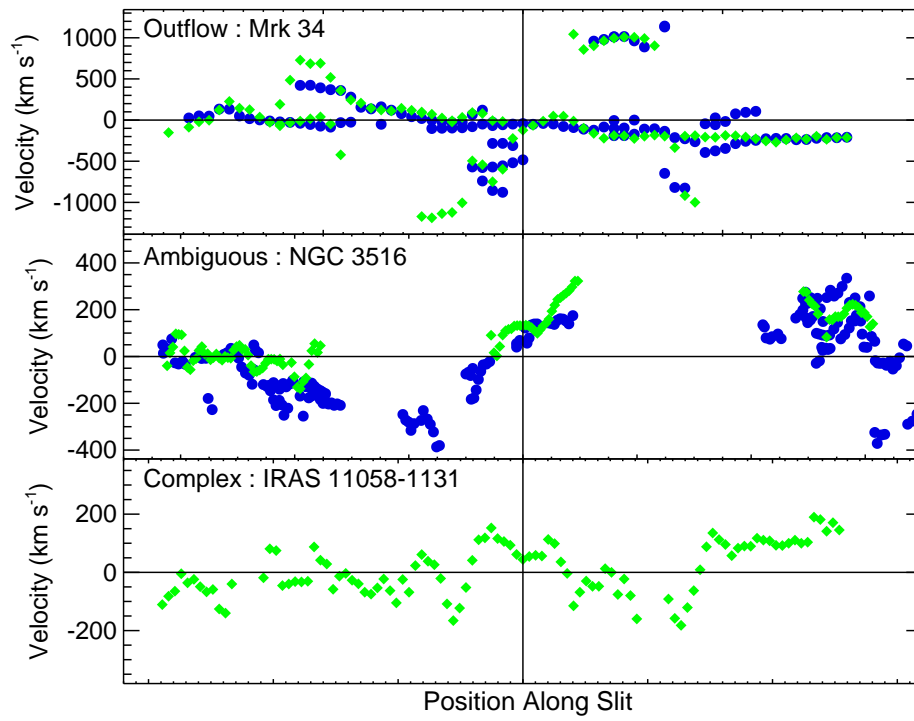


Fig. 3.— Radial velocities of [OIII] lines using the G430L (green diamonds) and G430M (blue circles) gratings for three AGN with different kinematic 'types'.

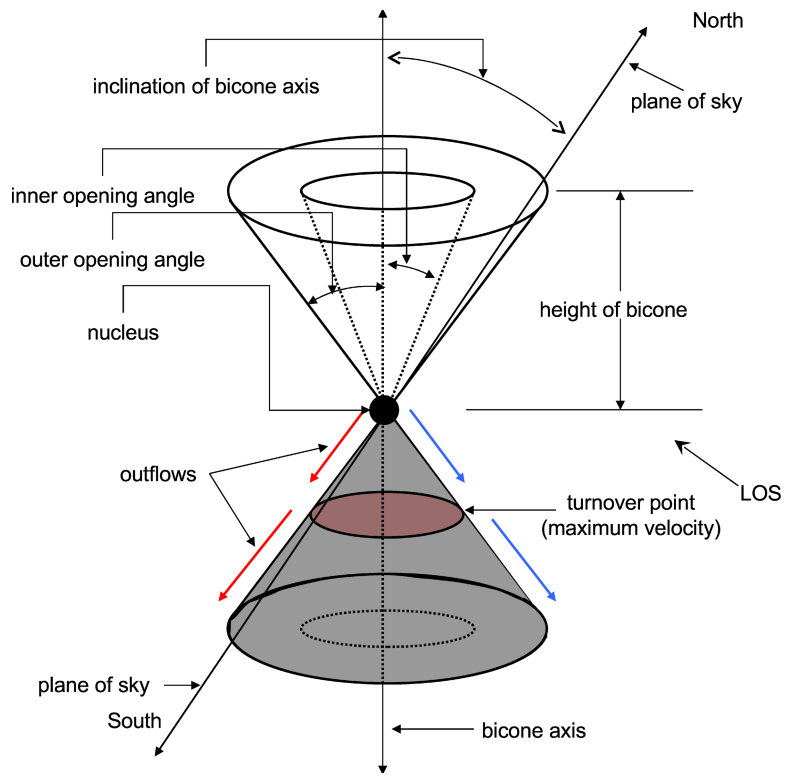


Fig. 4.— Cartoon displaying all alterable parameters used to create a kinematic model.

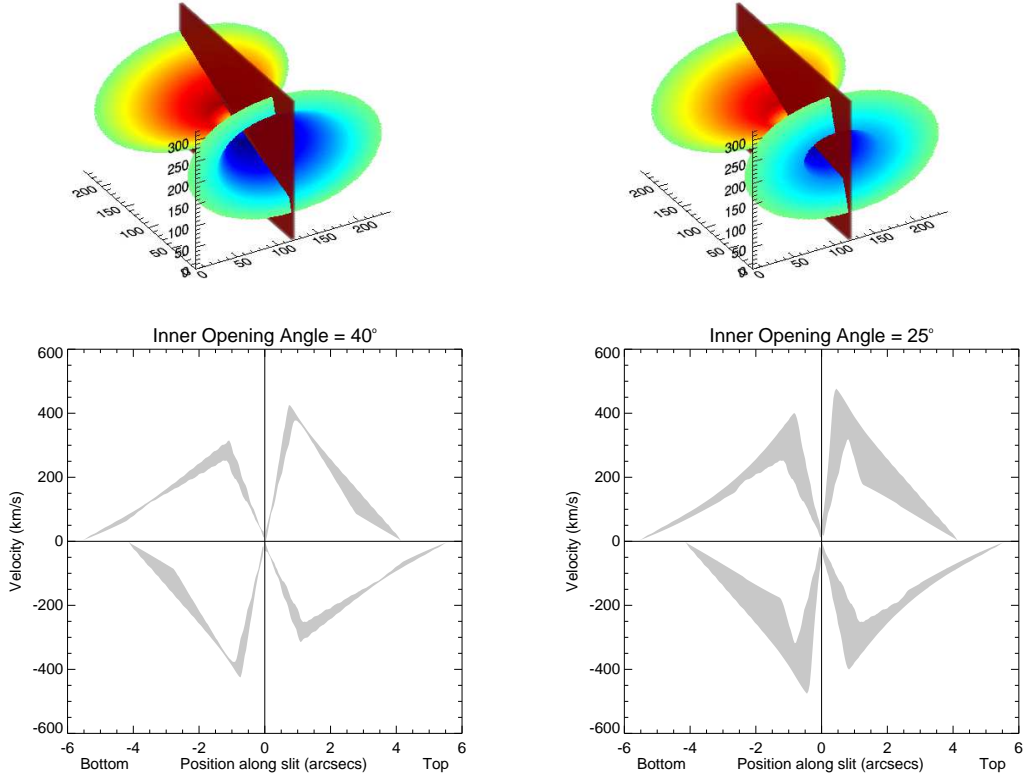


Fig. 5.— Top: Kinematic models using varied inner opening angles of 40° (left) and 25° (right) and a fixed outer opening angle of 50° . All other input parameters remain constant, inclination is fixed at 80° and maximum velocity is fixed at 500 km s^{-1} . Blue colors represent blueshifted outflow velocities, red colors represent redshifted outflow velocities. The red plane represents the orientation of the STIS long-slit observation with our LOS coming from the lower right. Bottom: Resultant extracted velocity plots along the given long-slit position showing radial velocity (positive, redshifted velocities increasing upward) as a function of position along the slit. Increasing the difference between inner and outer opening angles results in a larger range of velocities sampled closer to the nucleus, expanding the shaded component areas.

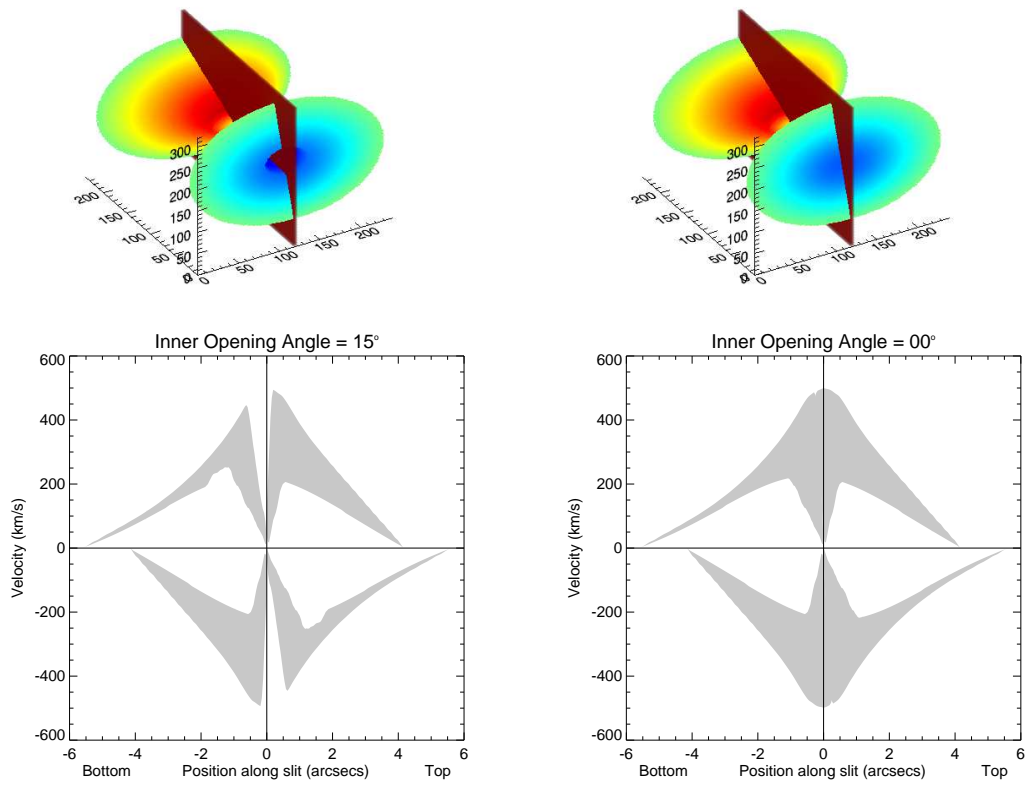


Fig. 6.— Same as Figure 5, except with inner opening angles of 15° (left) and 0° (right).

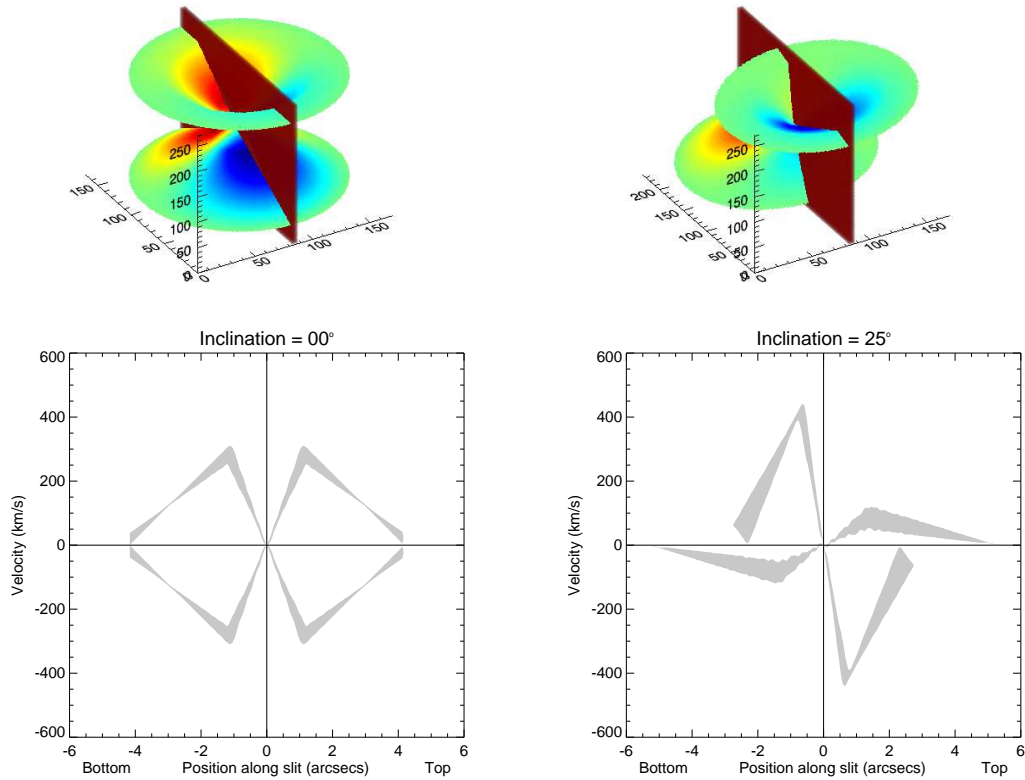


Fig. 7.— Top: Kinematic models using varied inclinations of 0° (left) and 25° (right). All other input parameters remain constant. Blue colors represent blueshifted outflow velocities, red colors represent redshifted outflow velocities. The red plane represents the orientation of the STIS long-slit observation with our LOS coming from the lower right. Bottom: Resultant extracted velocity plots along the given long-slit position showing radial velocity (positive, redshifted velocities increasing upward) as a function of position along the slit.

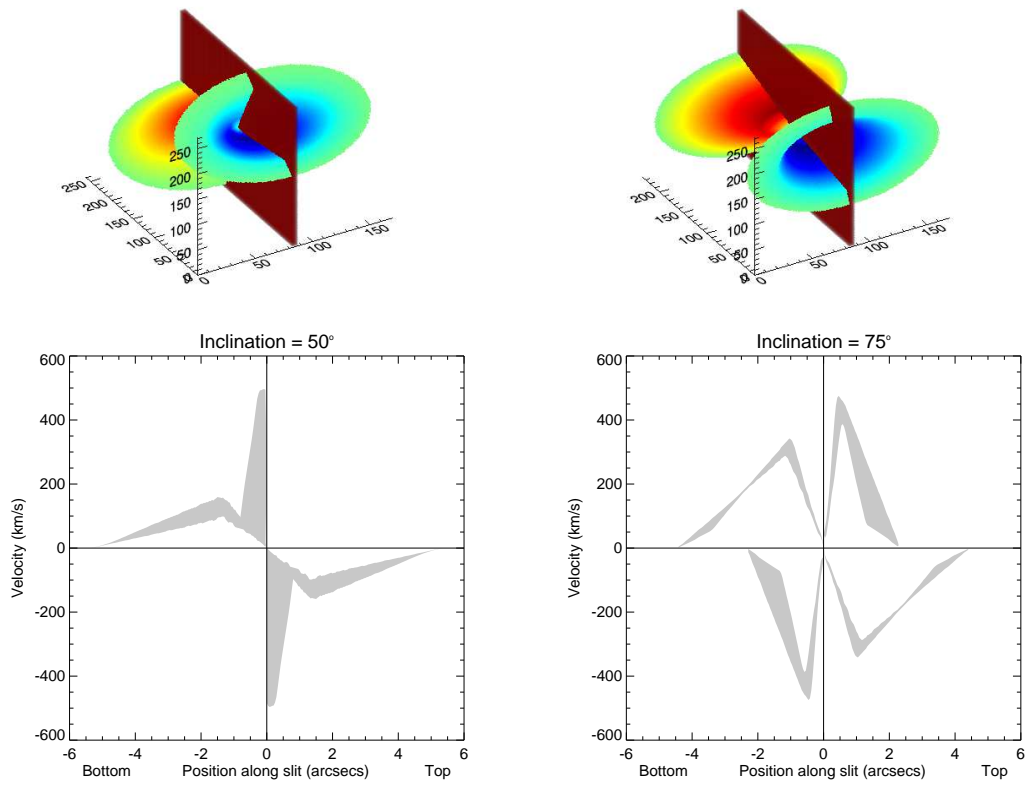


Fig. 8.— Same as Figure 7, except with inclinations of 50° (left) and 75° (right).

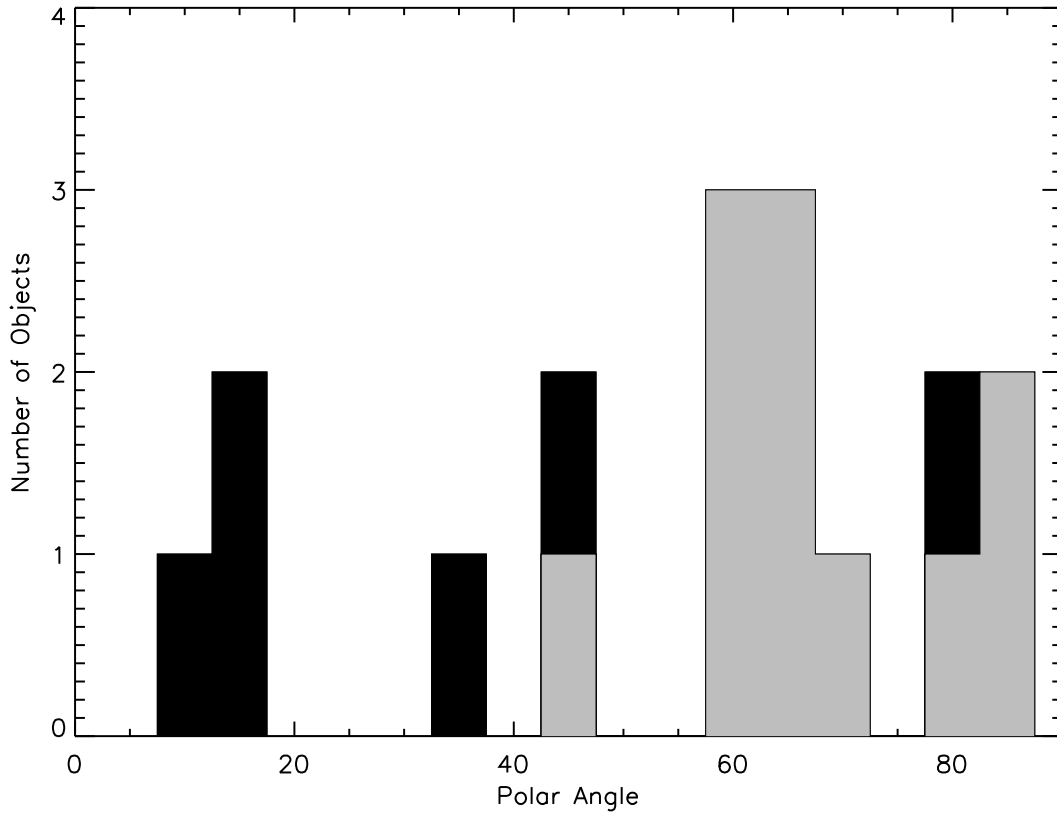


Fig. 9.— Histogram displaying the distribution of inclinations for Seyfert 1s (black) and Seyfert 2s (grey) in our sample, where the bicone axes of Seyfert 1s tend to be less inclined than Seyfert 2s. NGC 5506, modeled to have a high inclination, may be affected by host disk obscuration.

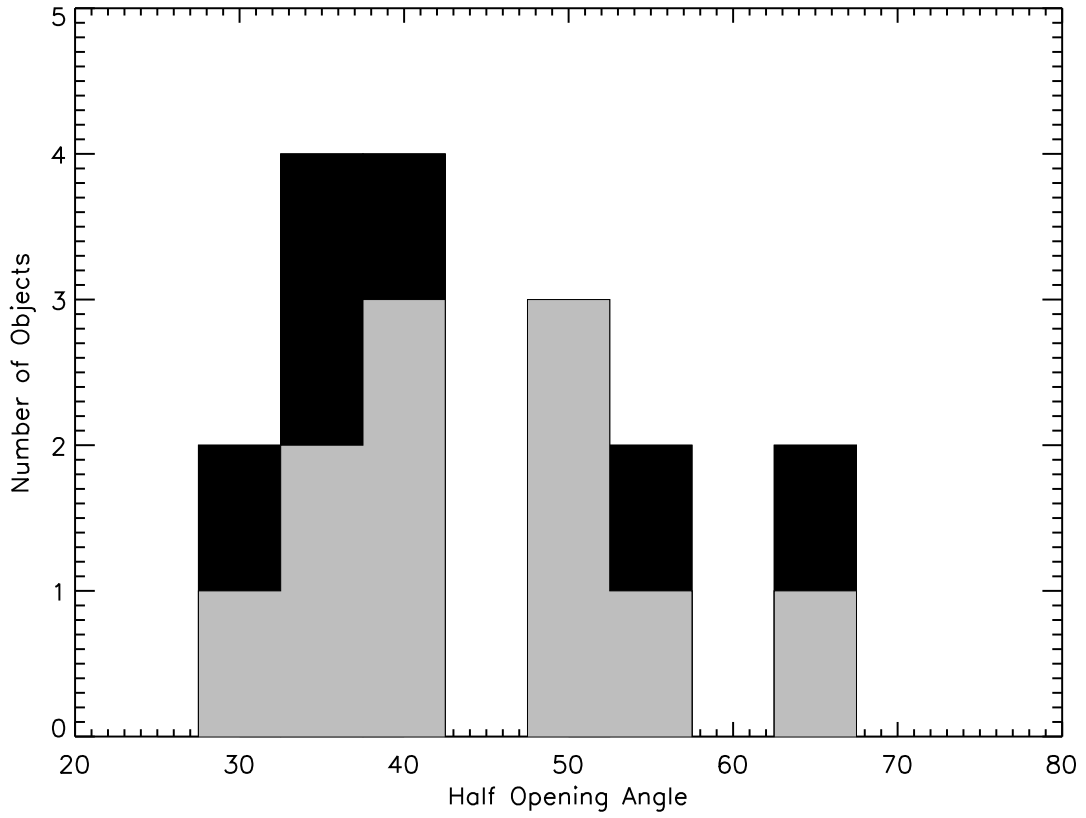


Fig. 10.— Histogram displaying the distribution of opening angles for Seyfert 1s (black) and Seyfert 2s (grey) in our sample. Seyfert 1s and Seyfert 2s appear to be evenly distributed.

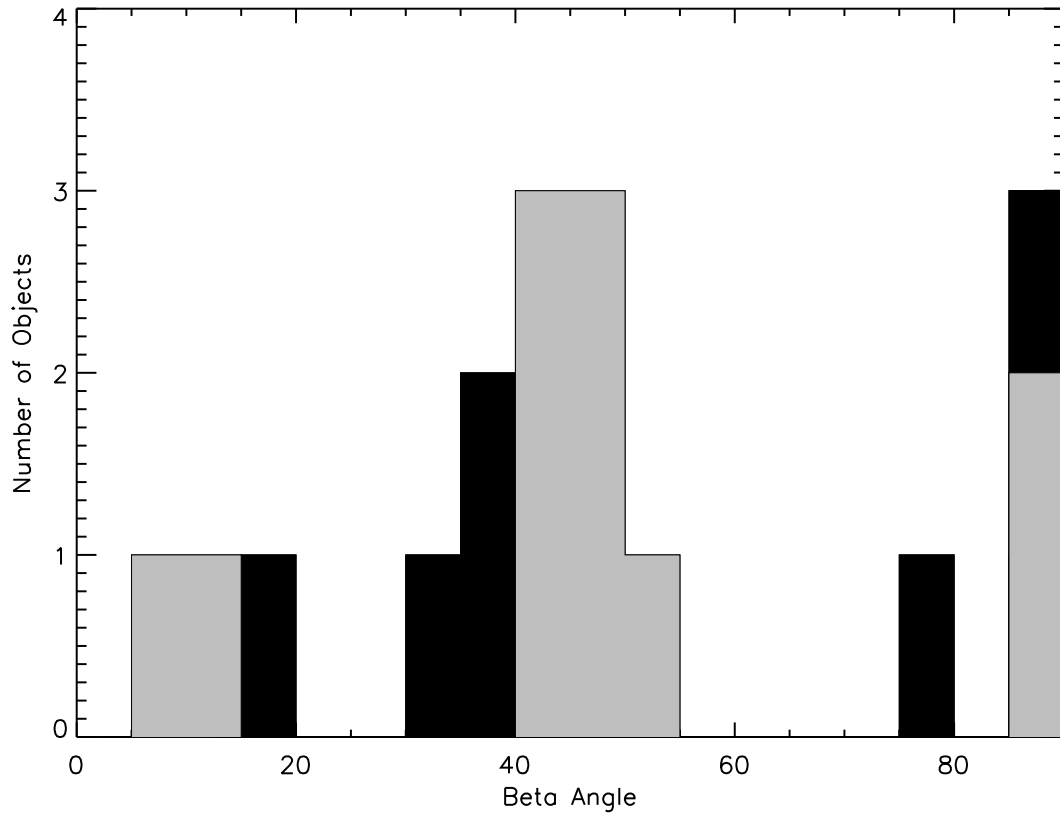


Fig. 11.— Histogram displaying the distribution of β angles for Seyfert 1s (black) and Seyfert 2s (grey) with modeled kinematics. β angles appear homogenously distributed between $0^\circ - 90^\circ$.

A. Targets With Clear Outflow Signatures

A.1. *Circinus*

Figure 12 shows that this is a Seyfert 2 galaxy with a single NLR cone visible in [O III] imaging that is nearly perpendicular to the major axis of the host disk. The modeled kinematics provide a good fit to the data, matching well to both visible outflow components. At this orientation, it is unlikely that an intersection exists between the extended host disk and the NLR. As the projected opening angle of the model NLR (91°) is close to that of the opening angle seen in available imaging (96°) and the size of the NLR in this very nearby AGN is only ~ 50 pc, it is likely that the NLR is ionizing a dense medium in the galactic disk. The south-east cone is undetectable at optical wavelengths as it is hidden behind the heavy extinction of the galactic disk (Ruiz et al. 2000; Prieto et al. 2005). Extended filamentary [O III] emission greater than $10''$ from the nucleus is not included in our model as slit positions containing this emission are displaced several arcseconds away from the nucleus, and the remote emission would have been difficult to accurately incorporate into a biconical model. An available G750M long-slit spectrum perpendicular to the NLR runs along the major axis and detects $H\alpha$ emission from H II regions surrounding the nucleus in the plane of the disk (Wilson et al. 2000), peaking at an observed velocity of ~ 175 km s $^{-1}$. This allows us to determine that the rotation of the host disk is blueshifted to the north and redshifted to the south; combined with NLR imaging, this confirms that the south-east side of the host disk is closer to us, obscuring the south-east NLR cone. Greenhill et al. (2003) found that H $_2$ O maser emission traces a warped, edge-on accretion disk at radii between ~ 0.1 and 0.4 pc and suggest that the warping of the accretion disk collimates the NLR outflow. The resultant model from their hypothesis is similar to our own, though their full opening angle appears to be over 130° , much larger than our 82° .

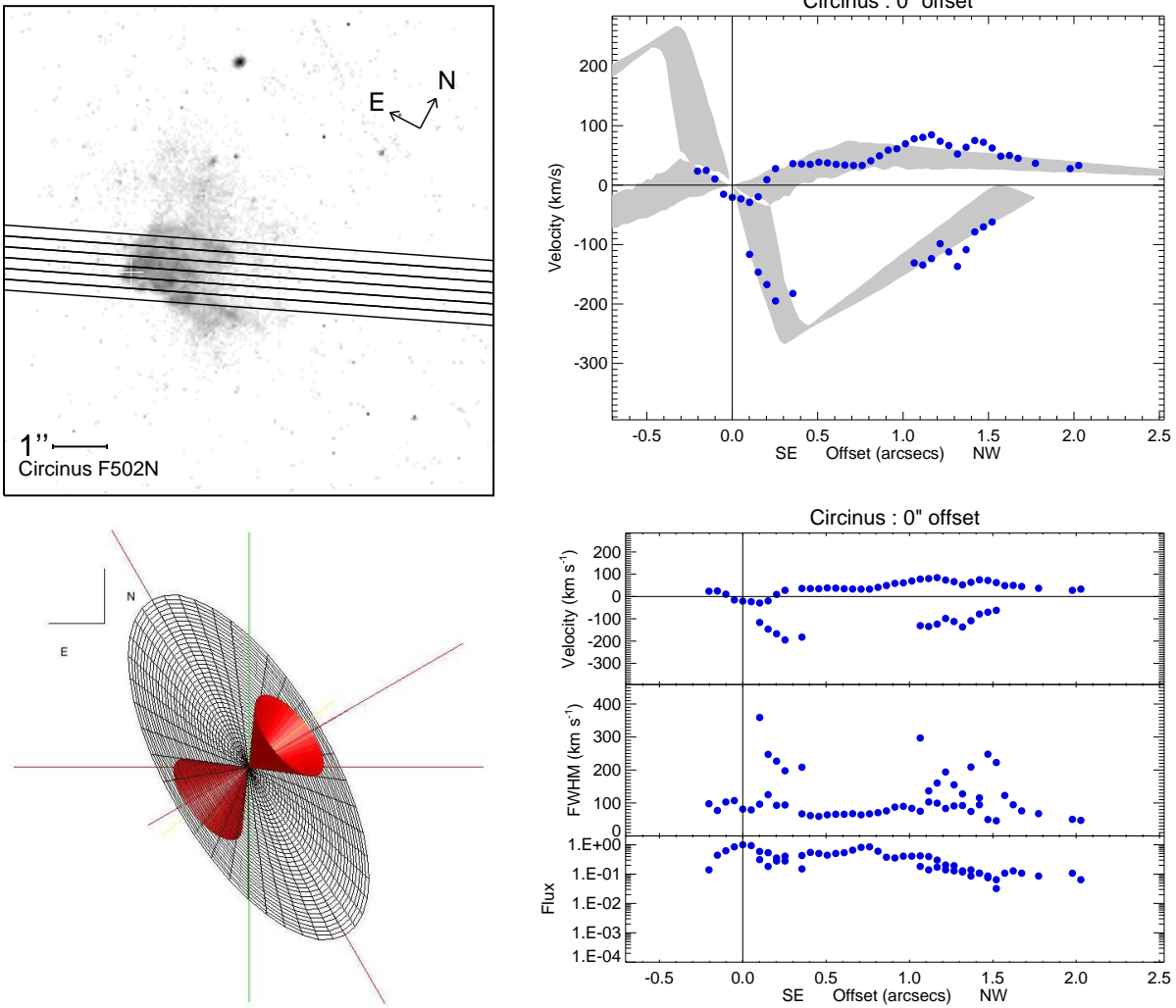


Fig. 12.— Top Left: *HST* imaging of Circinus with STIS observation positions overlotted. Top Right: Kinematic model for the central slit position of Circinus fitting two kinematic components. Bottom Left: Corresponding geometric model of the NLR with disk geometry. The bicone axis is illustrated as a yellow line. Black axes illustrate the extended plane of the host galaxy. Red axes illustrate the plane of the sky. Bottom Right: Velocities, FWHMs, and fluxes normalized to the highest measured flux for the central slit position of Circinus. Green diamonds, blue circles, and red squares correspond to G430L, G430M, and G750M grating data respectively.

A.2. *Mrk 34*

This is a Seyfert 2 galaxy with a backwards S-shape NLR, as shown in Figure 13, similar to Mrk 3 (Crenshaw et al. 2010). The modeled kinematics provide a good fit to the data, matching well to all four components save for a few high-velocity points. Employing our geometric model, we see that the S-shaped formation is likely an intersection between a gas spiral in the host disk and the ionization bicone as the projected area of the host disk enclosed by the outer opening angle matches well with emission seen in the [O III] imaging. Similar to Mrk 573 (Fischer et al. 2010), we suggest rotation does not play a role in the kinematics we observe as the low velocity components would correspond to a disk rotating clockwise while the host disk spiral arms are winding up in the counterclockwise direction. Kondratko et al. (2006) identified water maser emission in Mrk 34 due to an edge-on accretion disk. Thus, because our model gives the inclination of the bicone axis to be 25° out of the plane of the sky, it is possible that Mrk 34 experiences the same warped disk scenario as Circinus. Alternatively, if a torus is collimating the ionizing radiation, it is tilted $\sim 25^\circ$ with respect to the maser disk. This scenario would still suggest warping as the inflow moves from the torus to the accretion disk.

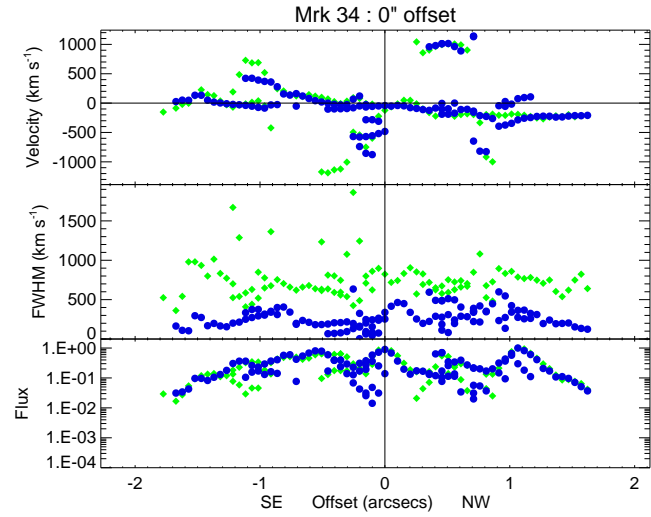
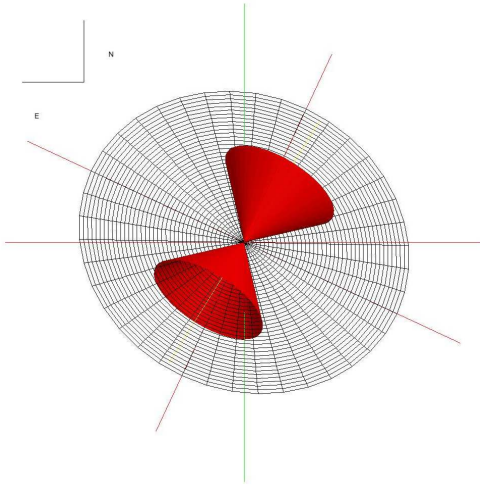
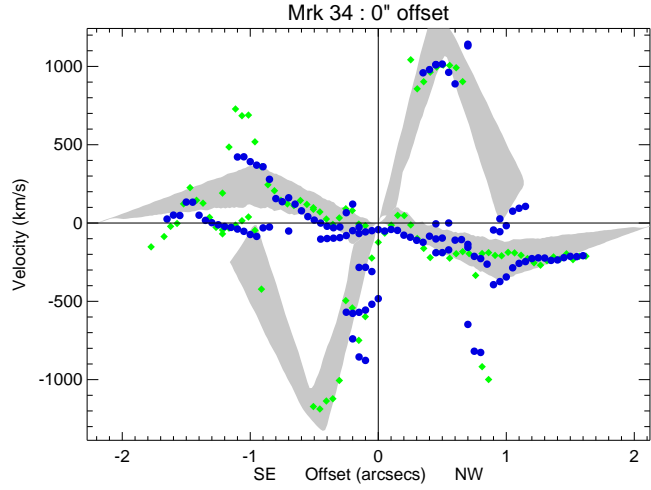
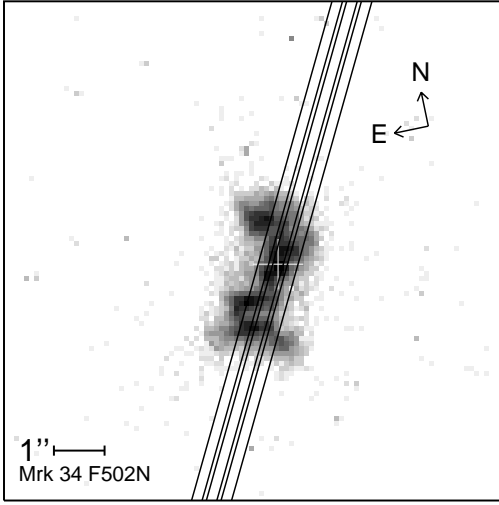


Fig. 13.— Same as Figure 12, but for Mrk 34 fitting four kinematic components..

A.3. *Mrk 279*

Mrk 279 is a Seyfert 1 residing in a moderately inclined host. The modeled kinematics provide a good fit to the data, as we are able to account for three components within a small area over the nucleus. Imaging of the NLR shows a compact area slightly more than $1''$ in diameter. The opening angle seen in the [O III] imaging has a similar width of 140° as the intersection between the host disk and NLR in the geometric model. While the resulting wedge geometry of the intersection matches well with the imaging, our model assumes that the inner portion of each NLR cone is hollow. This creates a discrepancy between the model and imaging data as we should only see a 'V' of emission across the disk without seeing the central portion illuminated because our model assumes the center of the cone is hollow. It is possible that the dust and gas within the portion of the host disk illuminated by the NLR has been evacuated.

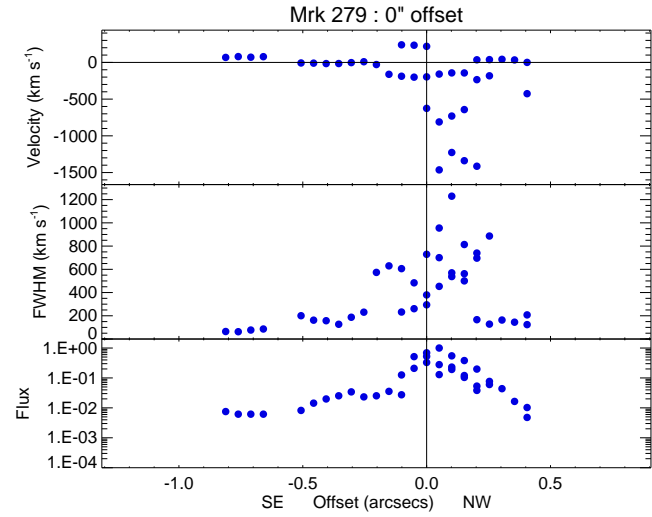
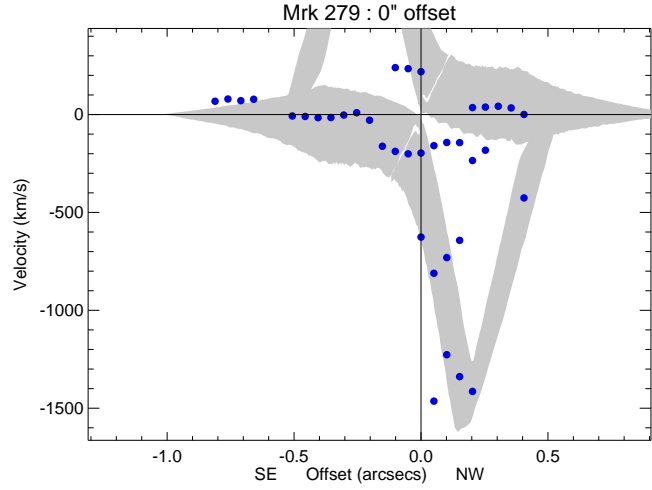
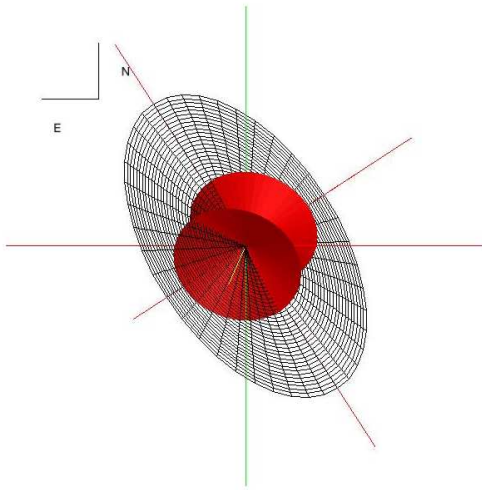
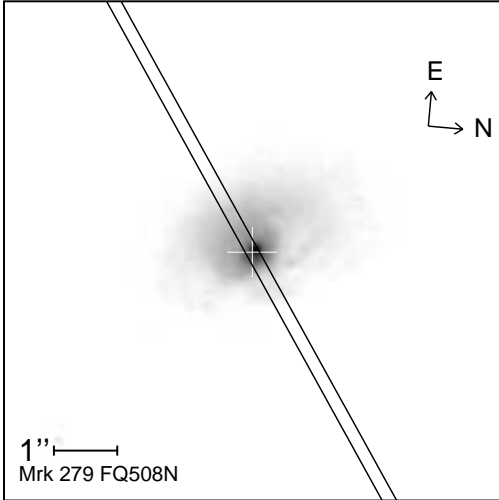


Fig. 14.— Same as Figure 12, but for Mrk 279 fitting two kinematic components.

A.4. *Mrk 1066*

Mrk 1066 hosts the Seyfert 2 AGN with the smallest opening angle in our sample with a θ_{max} of 25° . The modeled kinematics provide a good fit to the data. The majority of the detected emission resides in three knots northwest of the nucleus, which can be modeled as a single cone inclined 10° out of the plane of the sky. Bower et al. (1995) creates an [O III] + $H\beta$ emission-line image that depicts a similar single cone to the northwest of the AGN nucleus with a θ_{max} of 23° . At the modeled orientation, including the disk geometry determined by Kinney et al. (2000), the bicone does not intersect with the host disk, which obscures the unobserved second cone, similar to Circinus. Likewise, the close proximity between the projected model opening angle (51°) and the opening angle seen in available imaging (47°) suggests that the NLR is ionizing a large medium above the host disk.

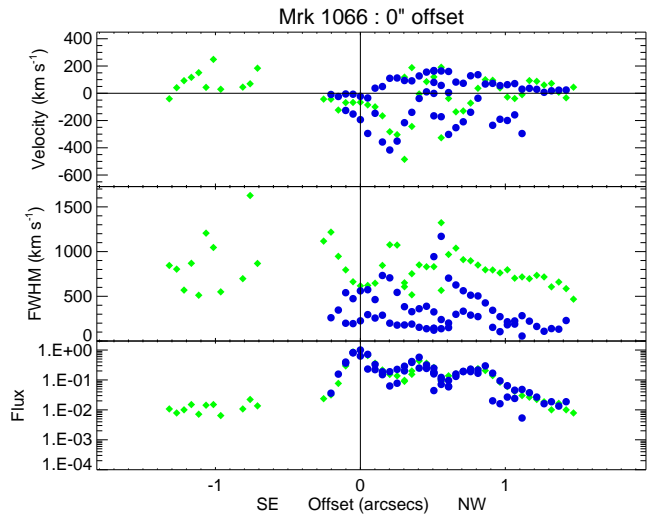
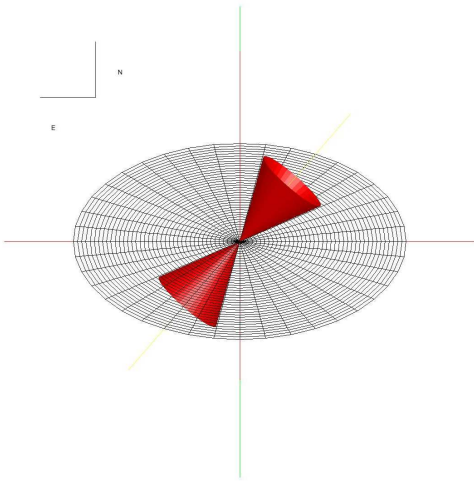
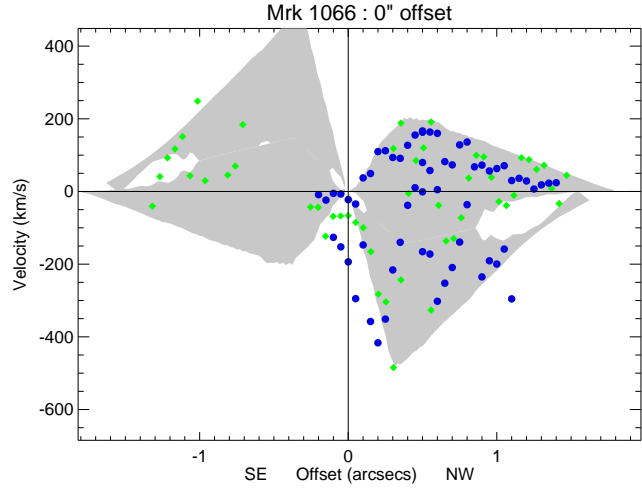
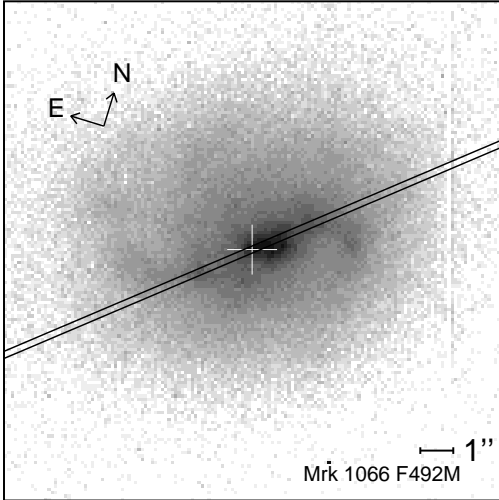


Fig. 15.— Same as Figure 12, but for Mrk 1066 fitting three kinematic components.

A.5. NGC 1667

NGC 1667 is a Seyfert 2 with a compact NLR spanning $\sim 1''$ in diameter in our STIS observation. NGC 1667 is unique in our sample in that we do not directly detect NLR emission in its *HST* images. Continuum imaging shows a fairly unspectacular nucleus, with a bright central region overlapped by several dustlanes. Figure 16 shows that the modeled kinematics provide a good fit to the data, although we cannot compare our modeled NLR geometry with the available broad band imaging as we cannot see where [O III] emission is present. As correspondance between imaging and our models is a parameter we use to create our most accurate fit, this discrepancy leaves room for improvement.

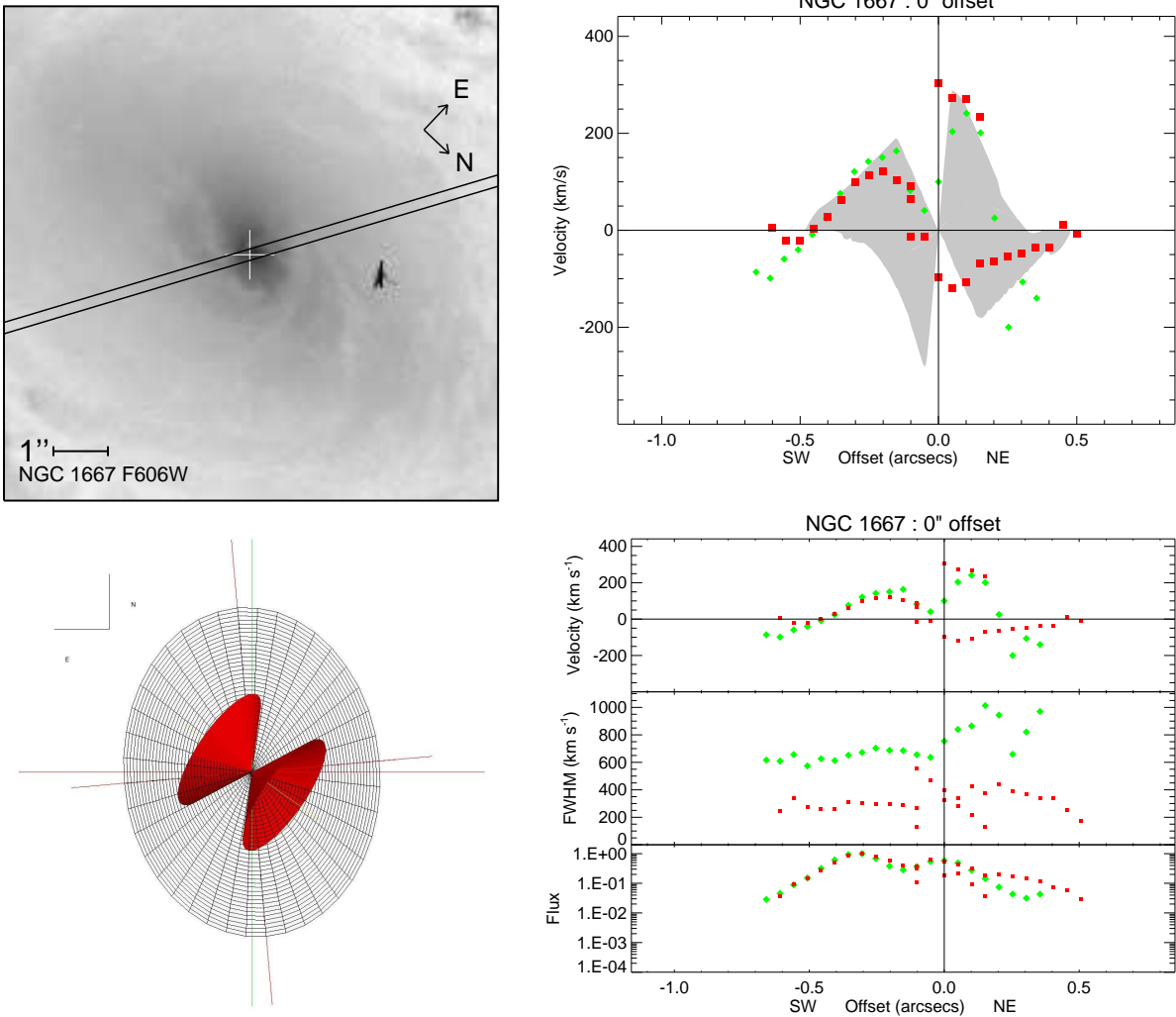


Fig. 16.— Same as Figure 12, but for NGC 1667 fitting two kinematic components.

A.6. *NGC 3227*

This is a highly reddened Seyfert 1 galaxy with an inclined disk that constrains NLR emission to the northeast of the nucleus. The modeled kinematics provide a fair fit to the data, with less successful fits in slit positions $\geq 0.5''$ from the nucleus. Modeling would not be possible using [OIII] spectra alone, as the single available G430L slit position does not return enough kinematic information to fit to a model, as shown in the online supplementary data. Fortunately, supplementary G750M spectra map out a large portion of the NLR, which allow us to see prominent doppler-shifted $H\alpha$ emission northeast of the nucleus. Though corresponding [O III] emission is lacking, we can assume that the observed emission is due to outflows in the NLR versus ionization and rotation within the host disk as the kinematics are asymmetric, contain blueshifted velocities $> 400 \text{ km s}^{-1}$, and contain double-peaked profiles in the narrow $H\alpha$ emission line (see also Walsh et al. (2008)). The kinematics initially suggested that emission from both sides of a single cone are visible which would place the bicone axis near the plane of the sky. From available imaging, a conical shape that would correspond to such an orientation is not present, though much of the region to the east of the nucleus is illuminated. We find that the blue and redshifted kinematic components can instead be attributed to a single side of both cones, with the host disk extinguishing the other half of each cone, and that the bicone axis is near our line of sight. This alignment between bicone axis and host disk concurs with analysis in Crenshaw et al. (2002) which concludes that AGN reddening of NGC 3227 is due to lukewarm absorbers coplanar with the host disk.

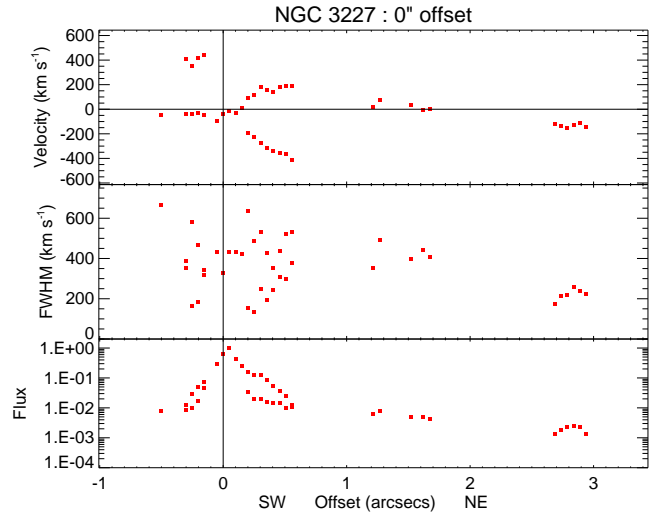
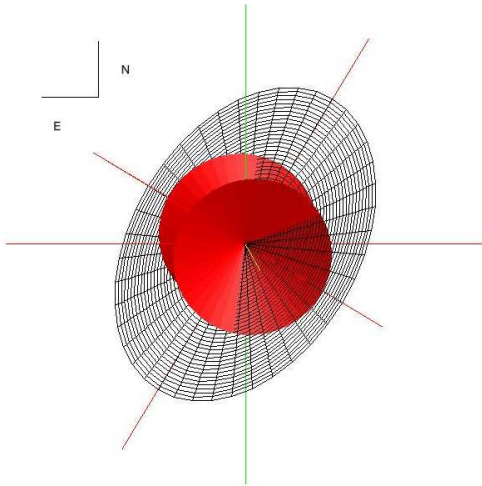
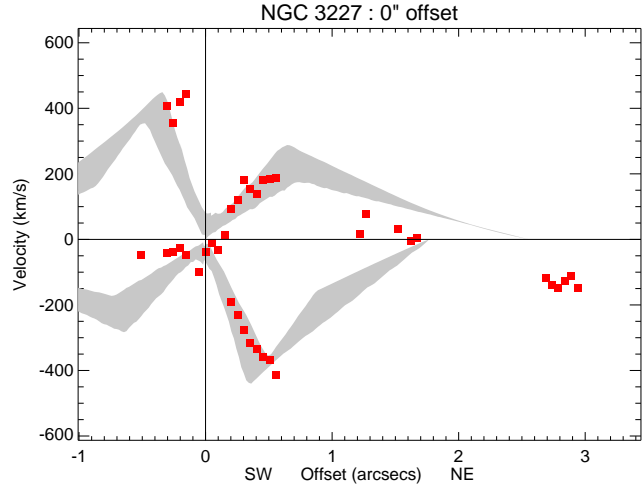
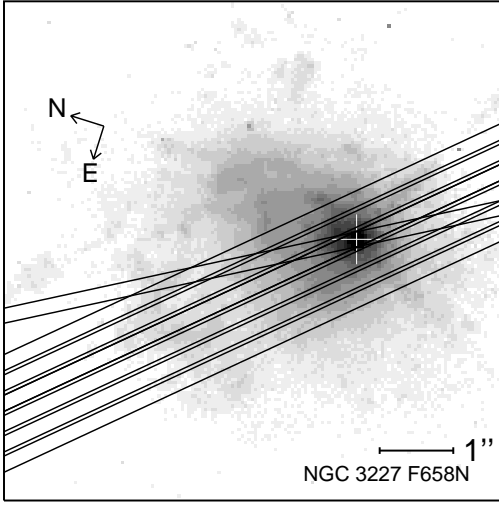


Fig. 17.— Same as Figure 12, but for NGC 3227 fitting four kinematic components.

A.7. *NGC 3783*

HST [OIII] imaging in Figure 18 depicts Seyfert 1 galaxy NGC 3783 as a nearly unresolved nuclear point source less than an arcsecond (~ 200 pc) in diameter. Emission detected with STIS reaches out to nearly twice that distance, with the [OIII] $\lambda 5007$ line remaining visible at fluxes less than 1% of that at the continuum source. The resultant kinematics depict red and blue shifts on either side of the nucleus which fits well with a biconical outflow axis nearly perpendicular to the plane of the sky such that the kinematics for each cone are both redshifted or blue shifted. This pole-on geometry agrees fairly well the symmetric, compact point source in the [OIII] imaging and the Type 1 designation of the AGN.

This target was also studied by Müller-Sánchez et al. (2011), using the *Keck* OH-Suppressing Infrared Integral Field Spectrograph (OSIRIS) and kinematic models that include outflows based on the work from Crenshaw & Kraemer (2000), where they publish a outflow parameter set with a more edge-on inclination and a view far outside of the bicone, invoking a clumpy torus model to explain their observations. Fitting their outflow + rotation model parameters to our kinematics, outflows would contribute to the redshifted velocities to the northwest and blueshifted velocities to the southeast with rotational velocities accounting for the remaining kinematics. Using additional parameters of imaging and host disk geometry to confirm this model pose problems for this result. [O III] imaging shows no elongated structure along the proposed bicone axis (P.A. = -177°), where one should expect emission on either side of the nucleus corresponding to a single cone. Additionally, their kinematic model states that the southern cone should be completely obscured by the host disk, however they provide a geometric model where the NLR outflow is instead bisected by the host disk, similar to our own model for NGC 3227.

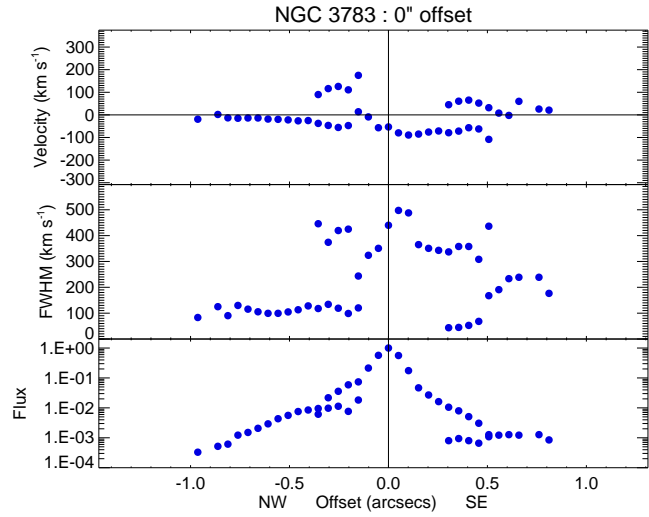
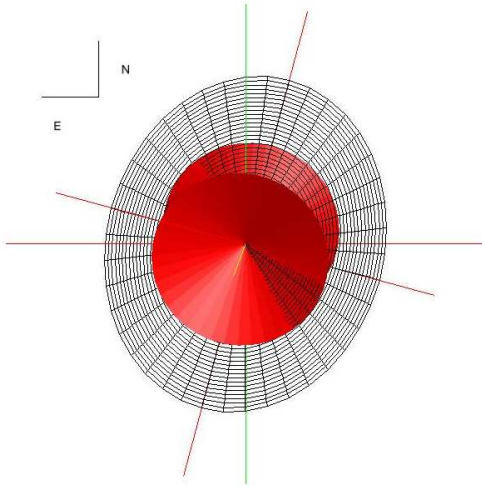
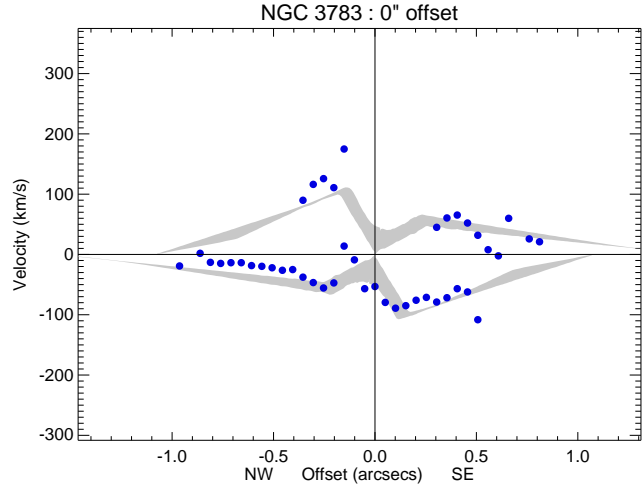
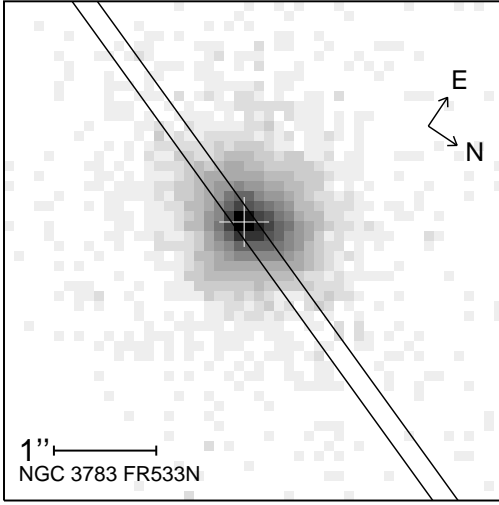


Fig. 18.— Same as Figure 12, but for NGC 3783 fitting four kinematic components.

A.8. *NGC 4051*

Observations of NGC 4051 are of particular interest as it is a Narrow-Line Seyfert 1 (NLS1). NLS1s have permitted lines with widths from their BLRs that are $\leq 2000 \text{ km s}^{-1}$ (FWHM), which are narrower than those of “normal” broad-line Seyfert 1s (BLS1s), but still broader than forbidden lines from the NLR (typically $\sim 500 \text{ km s}^{-1}$ FWHM; Osterbrock & Pogge 1987). The current paradigm for NLS1s is that they have supermassive black holes (SMBHs) with relatively low masses compared to BLS1s and they are therefore radiating at close to their Eddington limits (Pounds et al. 1995), i.e. $L/L_{\text{edd}} \approx 1$. Should NLS1s be more “pole-on” than normal broad-line Seyfert 1s (BLS1s), we could determine if these properties are due instead to a special viewing angle for NLS1s as suggested by their compact radio morphologies (Ulvestad et al. 1995).

The modeled kinematics provide a fair qualitative fit to the data (Figure 19), matching well to the inner accelerating blueshifted outflows. Using our final model parameters, we find that the axis of the bicone is inclined 12° away from pole-on, with our line of sight running near the edge of the NLR, between the inner and outer opening angles of the outflow. As we assume the highly blueshifted radial velocities are due to a biconical outflow, there is a noticeable lack of corresponding highly redshifted velocities near the nucleus. Combining the outer opening angle of the kinematic model with the inner disk geometry (Barbosa et al. 2009) suggests that the lack of redshifted outflow is likely due to disk obscuration.

We find that the inclination of NGC 4051 is near pole-on at 12° , and that the angle between the outer edge and our line of sight to be nearly the same. Analysis done for the three additional available unobscured NLS1s in our sample, Akn 564, Mrk 766 and Mrk 1040, show similar highly blueshifted velocities near their nuclei, suggest that a near pole-on orientation may be common. Unfortunately, the emission for these targets is too compact to fit with an accurate outflow model. Further study on the asymmetrical distribution of outflow velocities on either side of nuclei for both NLS1s and BLS1s will be required to test the pole-on hypothesis for NLS1s.

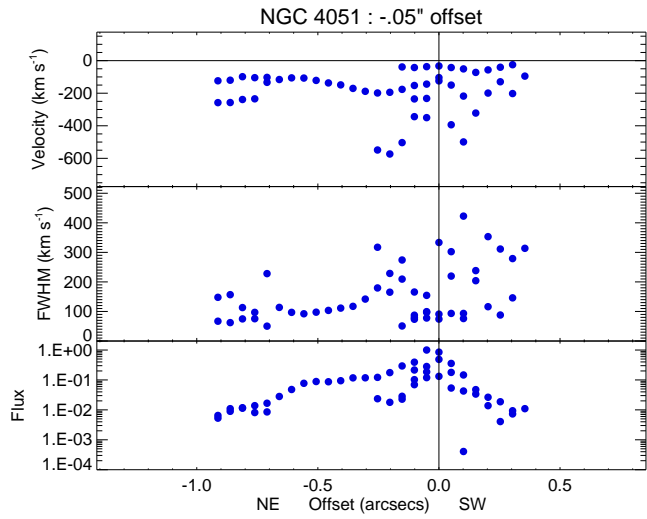
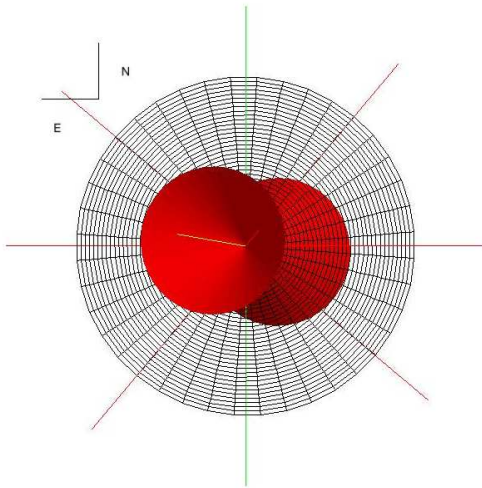
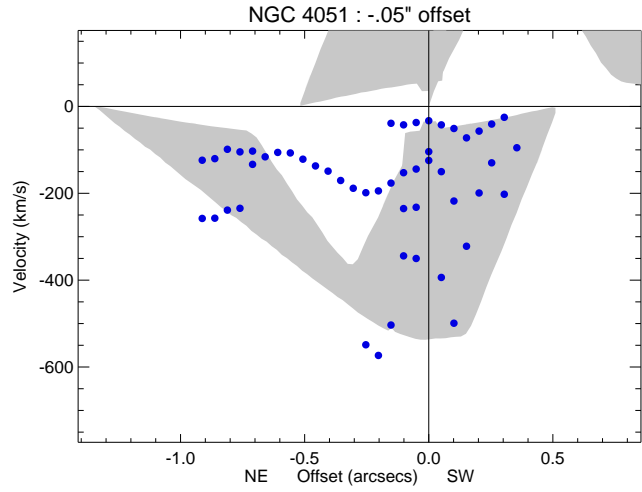
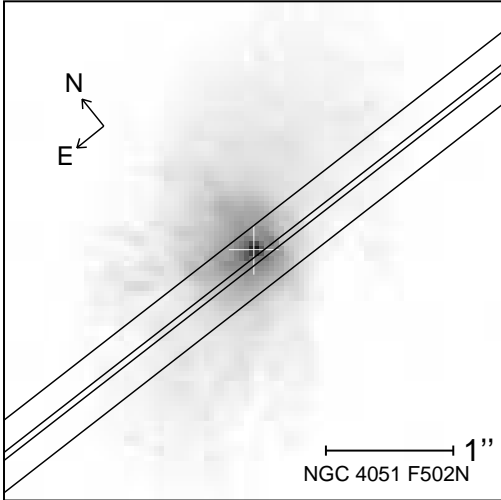


Fig. 19.— Same as Figure 12, but for NGC 4051 fitting two kinematic components.

A.9. *NGC 4507*

This is a Seyfert 2 galaxy that features two extended knots of emission. The first, $0.5''$ northwest of the nucleus along the STIS slit, is traveling near systemic velocity and fits well in the final kinematic model. The second knot, at $1''$ northwest of the nucleus, is highly blueshifted at 1000 km s^{-1} . This second knot is abnormal in that it is a spatially resolved, high velocity knot at a large distance from the nucleus such that it cannot be fit with our model. Rogue high velocity clouds such as this have also been documented in the kinematics of NGC 4151 (Das et al. 2005), though they are located at radii near the peak of the velocity curve versus the end of the curve in this case. Two other kinematic components exist in the blueshifted quadrant to the northwest of the nucleus, thus it is unlikely to be a part of the typical NLR outflow and is possibly a cloud near the axis of the bicone. Though many highly blueshifted velocities exist near the nucleus, the blueshifted component was fit such that the higher flux velocities (Figure 20) took priority. Additionally, opening the bicone to accommodate the high, southeast velocities would allow for the viewing of the central engine, which does not currently occur as our line of sight runs in between the inner and outer opening angles of the NLR.

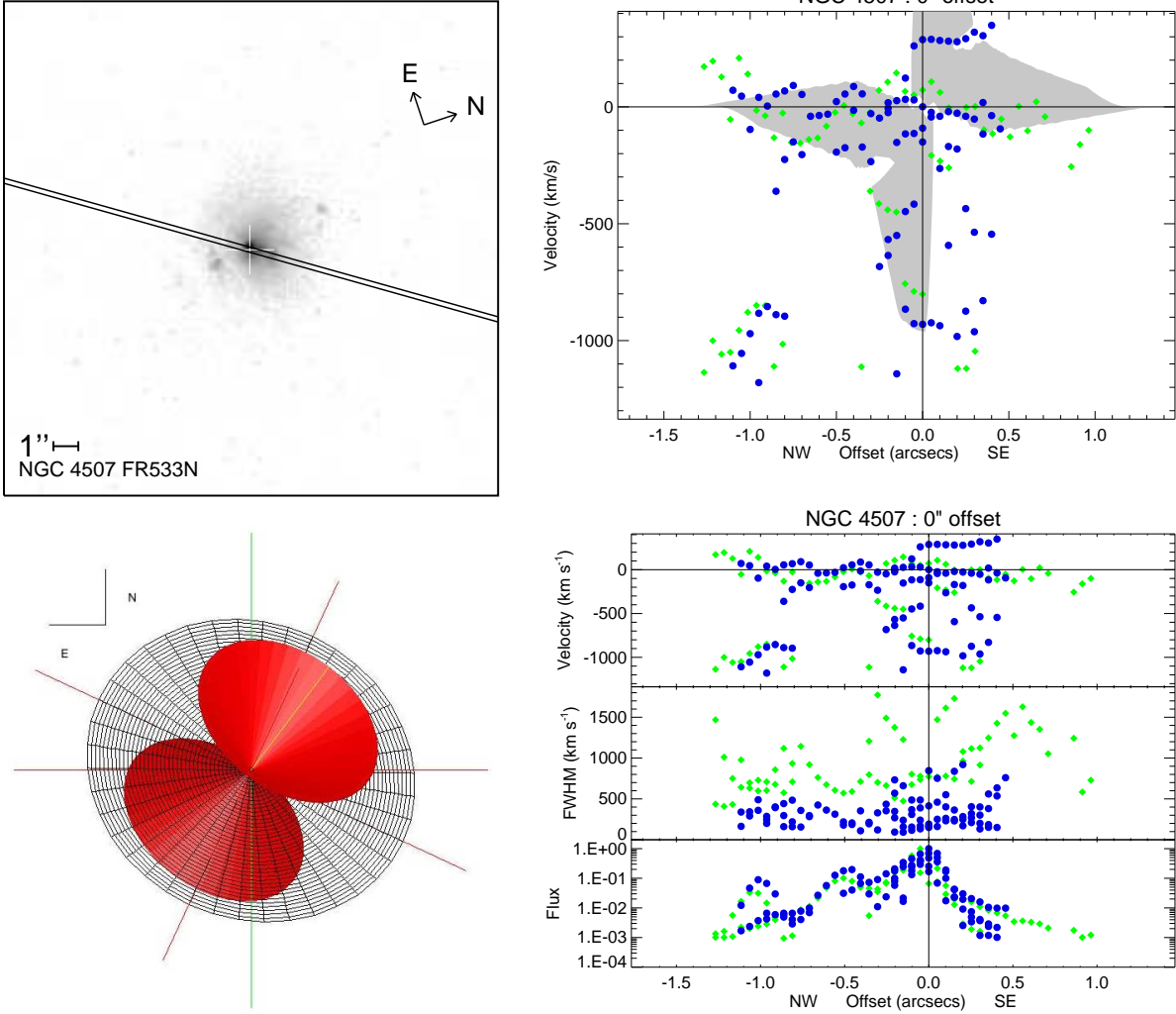


Fig. 20.— Same as Figure 12, but for NGC 4507 fitting three kinematic components.

A.10. *NGC 5506*

This is a debated NLS1 (Guainazzi et al. 2010) / Seyfert 1.9 (Maiolino & Rieke 1995) / Seyfert 2 (Trippe et al. 2010), whose classification is likely muddled by the fact that it resides in a near edge-on ($i = 76^\circ$) host. From imaging (Figure 21, see also Malkan et al. (1998)), a single, well-defined NLR cone is visible with its axis appearing to be near the plane of the sky and perpendicular to the host disk. Spectra available for this target consist solely of the slitless Ruiz et al. (2005) observations which can be fit well with a model that also agrees with the imaging. However, this edge-on AGN orientation does not conform to the unified model. With a majority of the extended emission being redshifted, it is possible that a stronger blueshifted component is obscured by the host disk (Imanishi 2000). As this is the only AGN with an edge-on host disk in our modeled sample, it is difficult to determine if the NLR of this AGN is also truly edge-on or if the host disk is extinguishing a large portion of the NLR emission, disguising a natural Type 1 AGN as an observed quasi-Type 2, and we are left modeling what remains of the NLR peering through the host disk. Additional evidence that the NLR model of NGC 5506 is suspect lies in a correlation between inclination and neutral hydrogen column density (N_H) (Fischer et al. in prep.) where AGN observed further from the axis of their NLR and closer to the toroidal structure surrounding the central engine have larger column densities. With a column density of $2.78 \times 10^{22} \text{ cm}^{-3}$ (Winter et al. 2009), NGC 5506 has one of the smallest densities in our sample, two to three orders of magnitude smaller than all other AGN with highly inclined NLRs. This implies a shallower inclination, more toward our LOS, than what is observed. As BLR emission has already successfully been detected in the near-IR (Nagar et al. 2002), further study of the NLR in the IR regime would avoid current extinction problems present at optical wavelengths and likely allow us to observe the full extent of the biconical outflow.

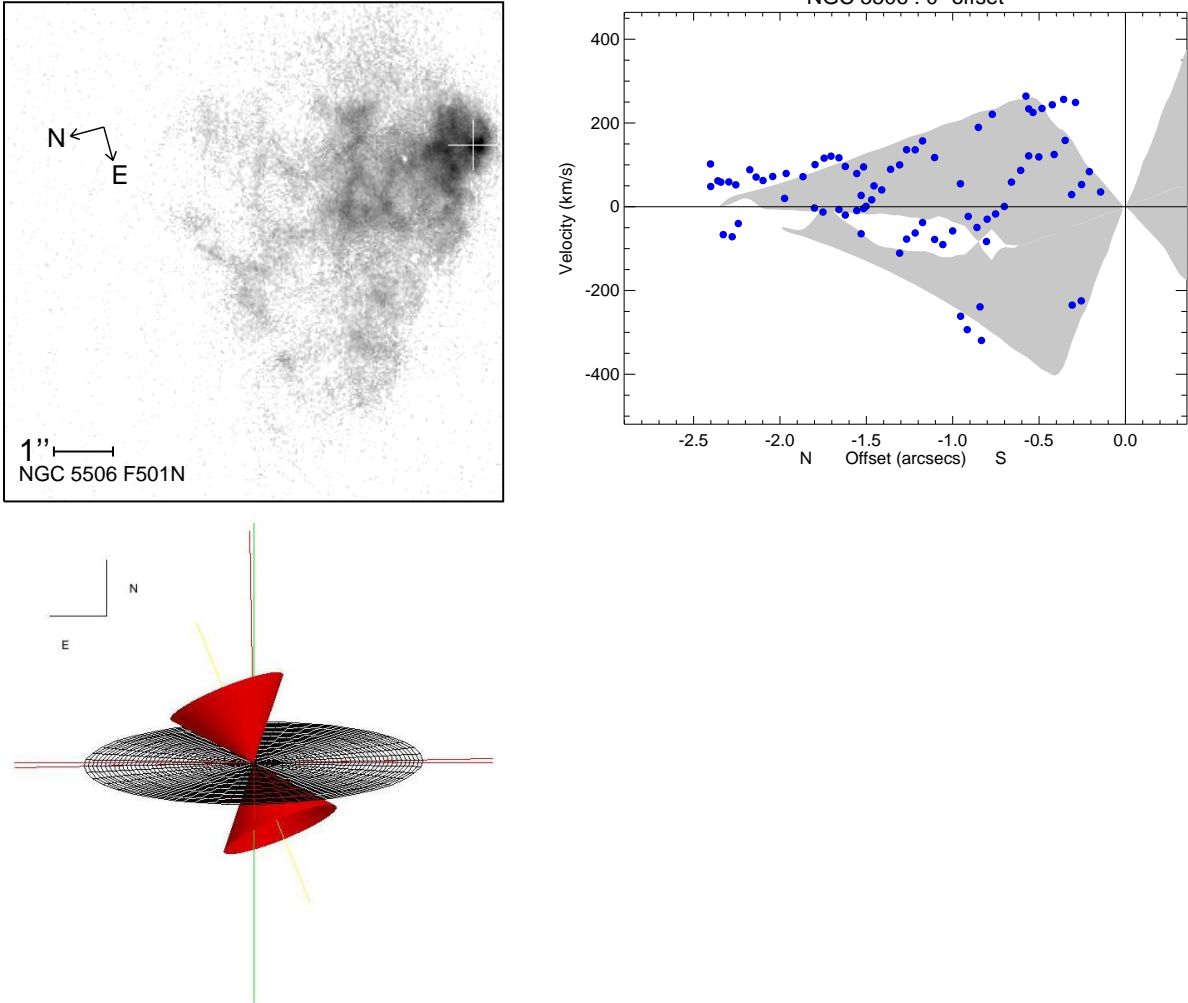


Fig. 21.— Same as Figure 12, but for NGC 5506 fitting two kinematic components. Kinematics are from Ruiz et al. (2001) data set, no FWHM or fluxes available.

A.11. *NGC 5643*

This is a Seyfert 2 which has a well-defined triangular emission region east of the nucleus, as seen in Figure 22. Filamentary structure within this ionized region appear to follow spiral arms in the host disk (Morris et al. 1985). Kinematics from slitless observations show that the majority of the extended emission is redshifted, with blueshifted velocities only visible near the nucleus. We fit a model to these kinematics that corresponds to a single, wide opening-angle cone inclined 65° from our line of sight. Available G430L and G750M long-slit observations have a position angle of -128° , placing them outside a majority of the NLR. Nonetheless, extracting components along the position angle of these observations shows that the model also fits these kinematics as well. Similar to Mrk 573, the extended [O III] emission seen in the imaging appears to result from the intersection between the host disk and the ionization bicone, providing a much narrower apparent opening angle than that of the model bicon. Our geometric model suggests that extended blueshifted emission should be observed west of the nucleus. This emission may be quenched by a warped disk or the presence of a dust lane to the southwest of the nucleus where traces of emission $4.5''$ and $8.2''$ west of the nucleus could represent emission seen through less obscured portions of the disk (Simpson et al. 1997). Spectroscopic observations by Schmitt et al. (1994) support this hypothesis as line emission to the west of the nucleus is more heavily reddened than that to the east.

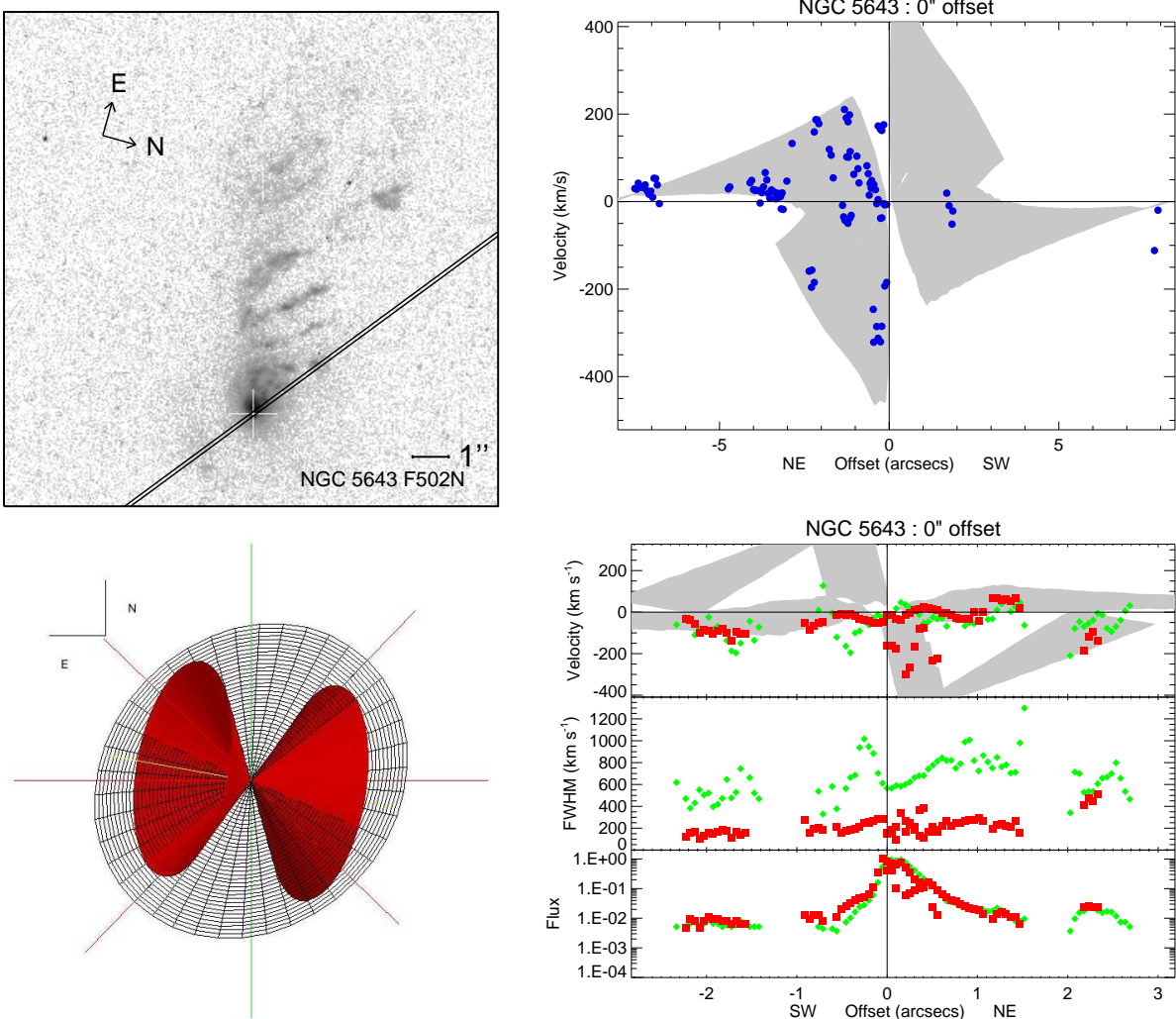


Fig. 22.— Top Left: *HST* imaging of NGC 5643 with STIS observation positions overlotted. Top Right: Kinematic model for the slitless kinematics of NGC 5643 fitting two kinematic components. Slitless kinematics are from Ruiz et al. (2001) data set, no FWHM or fluxes available. Bottom Left: Corresponding geometric model of the NLR with disk geometry. The bicone axis is illustrated as a yellow line. Black axes illustrate the extended plane of the host galaxy. Red axes illustrate the plane of the sky. Bottom Right: Velocities with overlaid kinematic model, FWHMs, and fluxes normalized to the highest measured flux for the long-slit observation of NGC 5643. Green diamonds, blue circles, and red squares correspond to G430L, G430M, and G750M grating data respectively.

A.12. NGC 7674

NGC 7674 is a Seyfert 2 with a distribution of radial velocities similar to Circinus with asymmetric extended emission to the northeast with high blueshifts and near systemic redshifts. The modeled kinematics provide an excellent fit to the data, clearly fitting the two observed components and what remains of the other velocities. Our model suggests the extended emission is due to a single cone, with the other cone obscured by the host disk. Radio data (Momjian et al. 2003) concurs with our model as jet axes are projected along the same position angle as the NLR bicone in our model, which also suggests a qualitatively good fit.

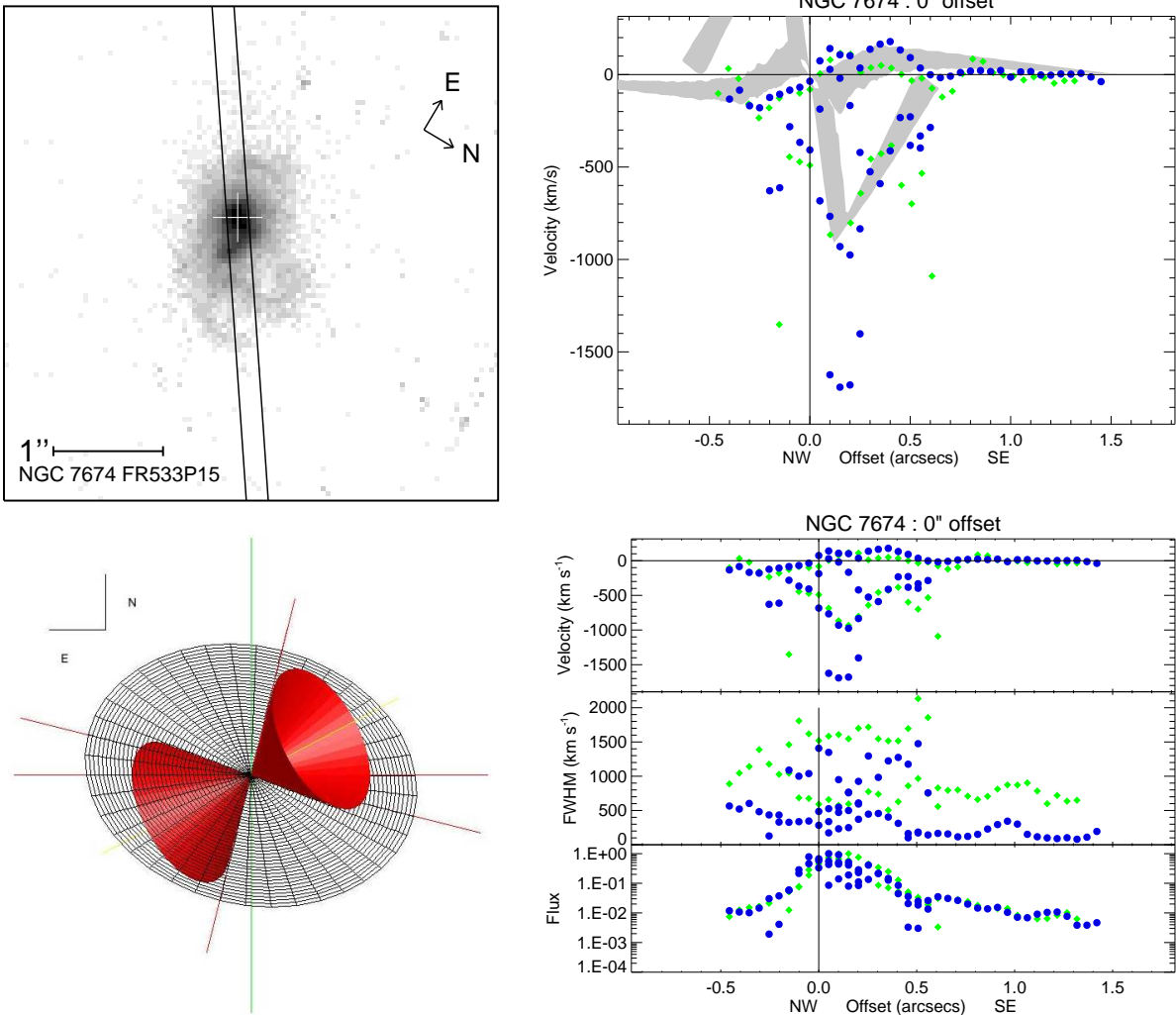


Fig. 23.— Same as Figure 12, but for NGC 7674 fitting two kinematic components.

B. Distinct Unmodeled Targets

B.1. *IRAS 11058-1131*

This is a Seyfert 2 that shows a likely intersection between the NLR and host disk in the visible S-shaped NLR seen in Figure 24. The kinematics of this target have been deemed ‘complex’ as no individual kinematic components can be seen in the radial velocity data. Velocities appear to be roughly rotational, as velocities further from the nucleus do not decelerate back toward systemic, but end with blueshifted values to the northeast and redshifted values to the southwest, reaching maximum velocities of $\sim 200 \text{ km s}^{-1}$. This implies a counter-clockwise rotation, which agrees with the apparent winding-up of the spiral arms that are illuminated. Velocity gradients responsible for the knotty, ‘complex’ kinematics observed may be due to in situ acceleration of ambient material similar to those seen in dust lanes of Mrk 573 (Fischer et al. 2010), though these gradients fail to align with specific flux peaks in the data.

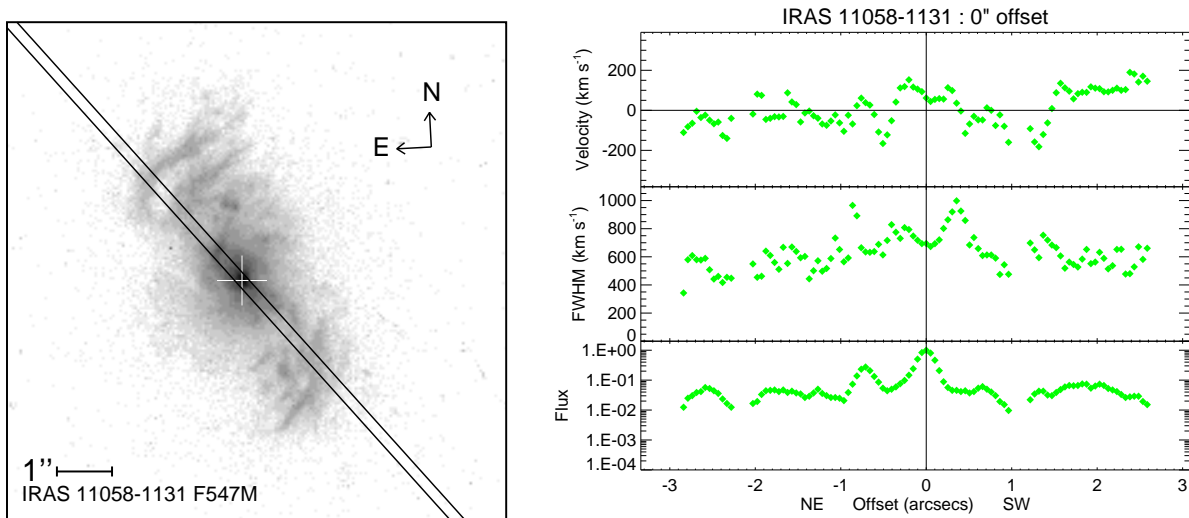


Fig. 24.— Left: *HST* imaging of IRAS 11058-1131 with STIS observation position overplotted. Right: Velocities, FWHMs, and normalized fluxes across the slit position.

B.2. Mrk 509

This is a Seyfert 1 that likely contains a tidal tail in its central regions. Seen in both optical continuum and [O III] imaging (Figure 25), this feature is composed of several knots of total length $2.2''$ at a position angle of -13° before jutting towards the nucleus from the southwest at a position angle of -110° . As the *HST* STIS slit was positioned favorably at 75° , we are able to observe the inner portion of the tail and analyze its kinematics. Southwest of the nucleus are redshifted velocities peaking near 400 km s^{-1} , which correspond to the highest flux emission lines at those positions. Coupling this data with the apparent projection of the tidal tail above the host galaxy disk suggests that the bright, inner portion of the tidal tail is inflowing. Should this be the case, we may be viewing a minor merger with a dwarf galaxy, and this system would provide a great opportunity to study the fueling of an AGN by a minor merger in progress. Assuming that the redshifted kinematic component southwest of the nucleus is an inflowing tidal tail, the remaining velocities do not provide enough information to fit a model to the true outflowing kinematics. Further observations of the entire tail, particularly the extended linear feature, would clarify which direction the feature is moving and whether or not it is inflowing.

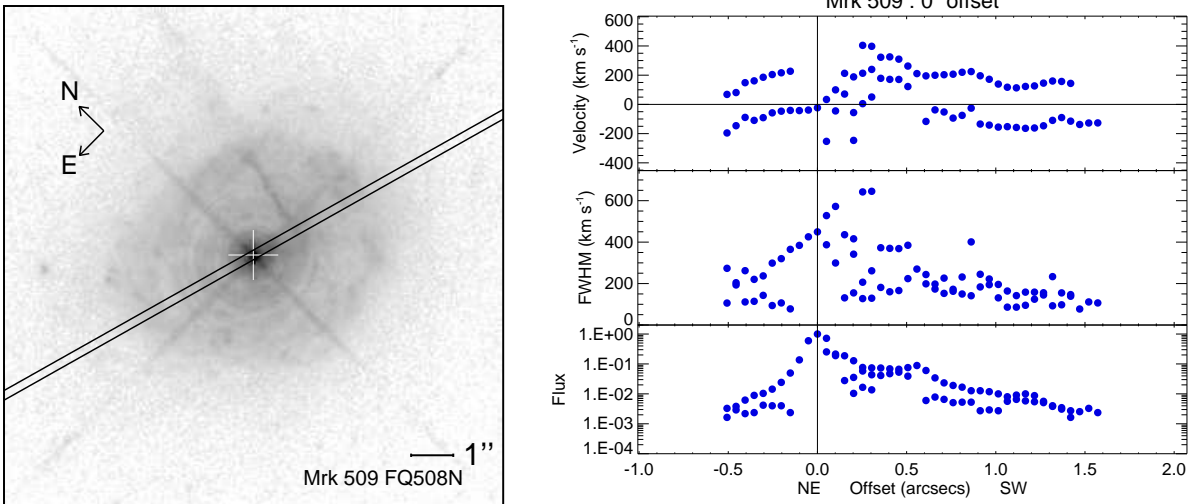


Fig. 25.— Same as Figure 24, but for Mrk 509.

B.3. NGC 3393

NGC 3393 is another Seyfert 2 that contains an S-shaped NLR, shown in Figure 26 that shows turbulent kinematics across several knots of emission, similar to Mrk 573 and IRAS 11058-1131. Though the NLR is well resolved (distinct knots visible over several arcseconds), it is unclear whether any distinct kinematic components are present. Two sets of high velocities exist to the southwest of the nucleus, one blueshifted component peaking at $0.75''$ and one redshifted component peaking at $1.25''$, which for a Seyfert 2 AGN would be two components for one cone to the southwest, inclined close to the plane of the sky. This is unlikely as imaging shows symmetric lobes of emission on either side of the nucleus which would not be replicated in the kinematic data. An alternative method to fitting the kinematics is to move the central position of the nucleus southwest $\sim 0.9''$. This would imply that the location of the continuum peak in the spectral image would not suffice as the true position of the AGN, possibly due to obscuration and reflection of the central engine. Peaks in flux to either side of the new center support the possibility of obscuration over the AGN. At this new position, the two previous high velocity peaks are now on each side of the center, combined with the extended, near-systemic velocities further out to provide four kinematic components to model. However, there is not enough evidence to justify the altered placement of the kinematic center.

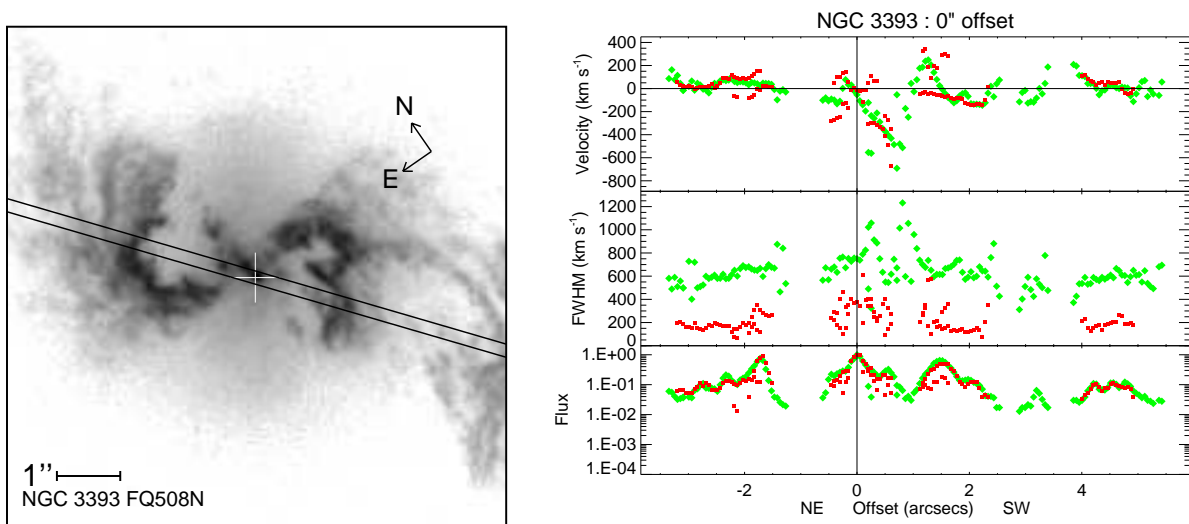


Fig. 26.— Same as Figure 24, but for NGC 3393.

B.4. *NGC 3516*

An atypical Seyfert 1 AGN as it contains an extended, S-shaped NLR (Figure 27) more often seen in Type 2 AGN, NGC 3516 is our prototypical "Ambiguous" outflow system. Similar to Mrk 3 and Mrk 573, this S-shape is likely due to dust lanes of the host disk becoming ionized as they intercept the NLR bicone. A well-defined symmetric kinematic component on either side of the nucleus traveling in opposite directions corresponds to the extended emission seen in imaging. While the kinematics seen in these components match signatures of outflow employed by our model, we cannot fit the data as the components are not adjacent to each other (see Section 5). It is not clear why components that correspond to the opposite side of each cone are not present, though it may be possible that they reside near the nucleus and are outshone by its flux or that there is a lack of an ionizing medium to detect where the components exist.

Though we cannot fit a kinematic model to NGC 3516, we attempted to recreate the NLR geometrically using the following assumptions:

- 1.) The side of each cone nearer the plane of the sky must intercept the host disk (using a Kinney et al. (2000) disk geometry) such that the resultant intersection geometry matches that seen in the [O III] imaging.
- 2.) The opening angle must be wide enough such that we are viewing the central engine (i.e. the geometric model must be a Type 1 AGN).

Using these parameters, we were able to construct a geometric model that agreed with the [O III] imaging using a bicone position angle, inclination, and outer opening angle of 40° , 50° , and 50° respectively. Unfortunately, the resultant kinematic model did not agree with the observed radial velocities and attempts to reconcile the two models have been unsuccessful.

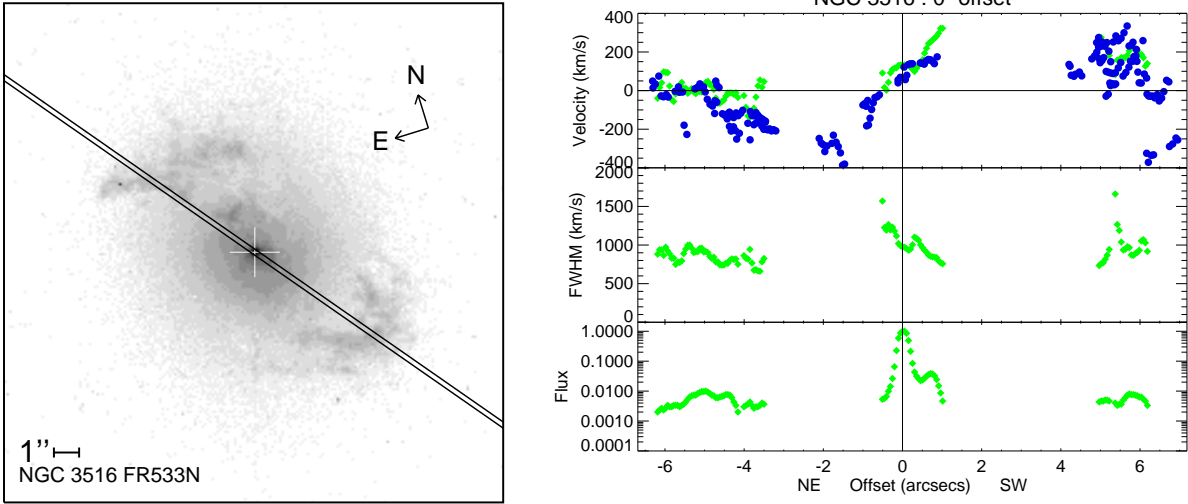
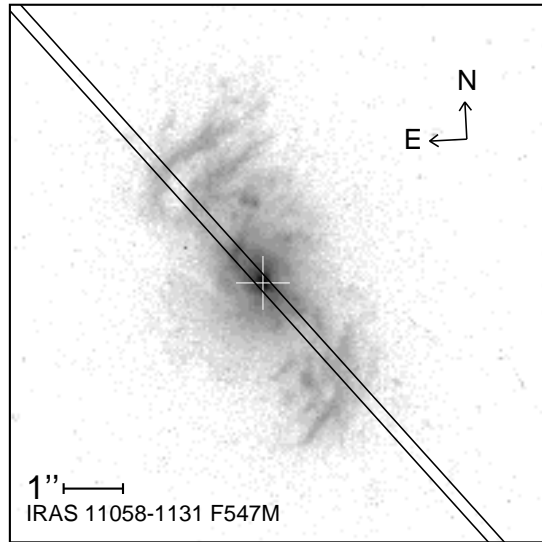
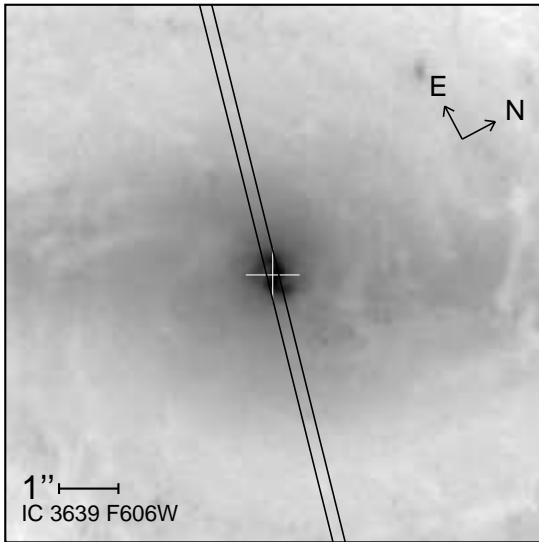
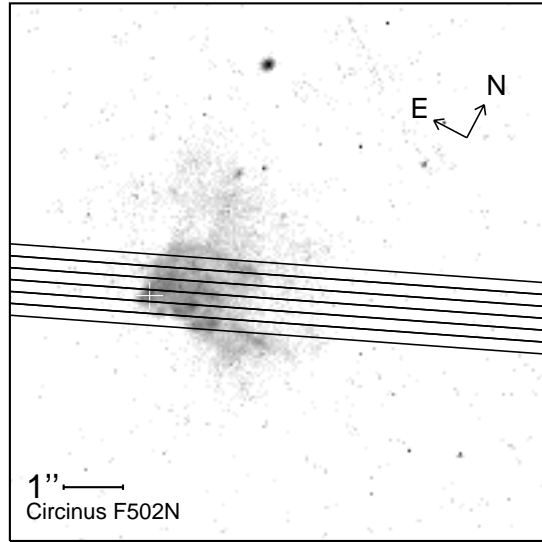
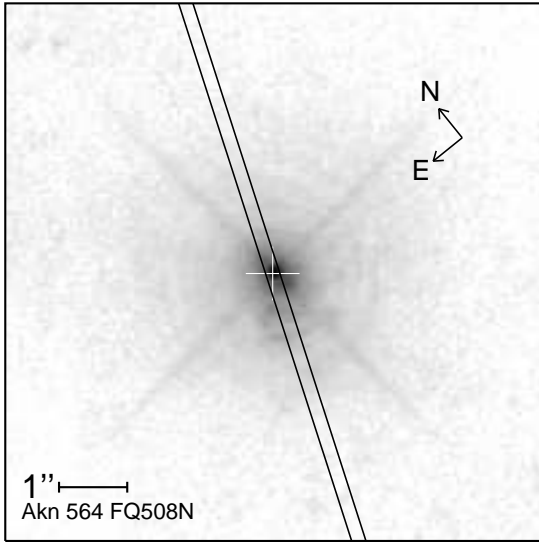


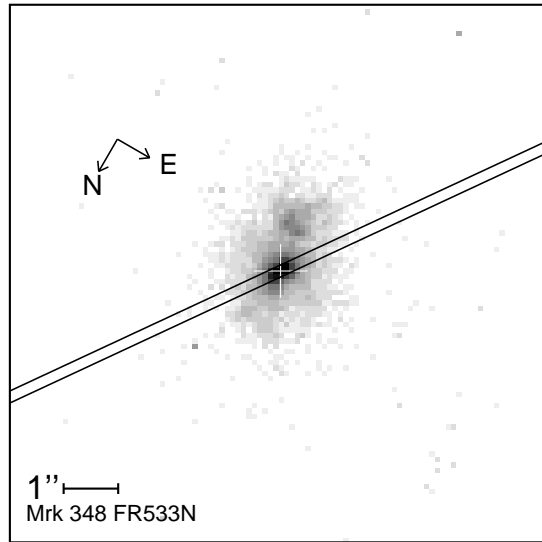
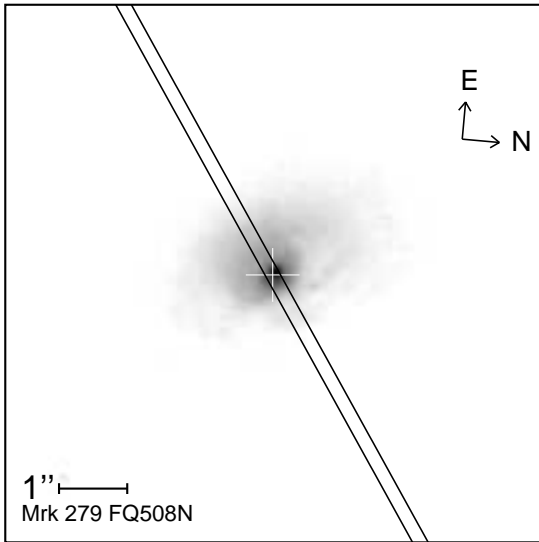
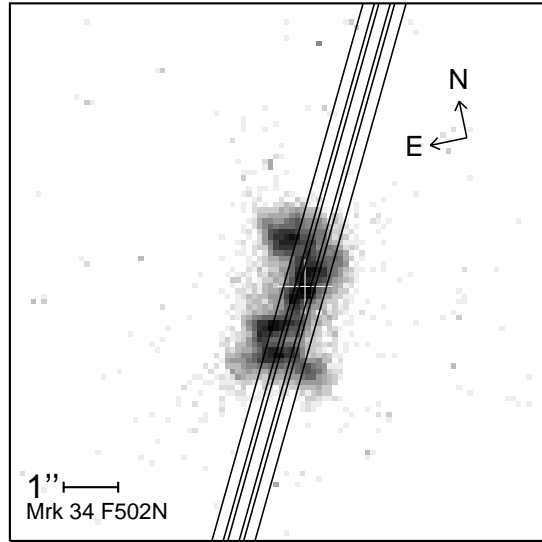
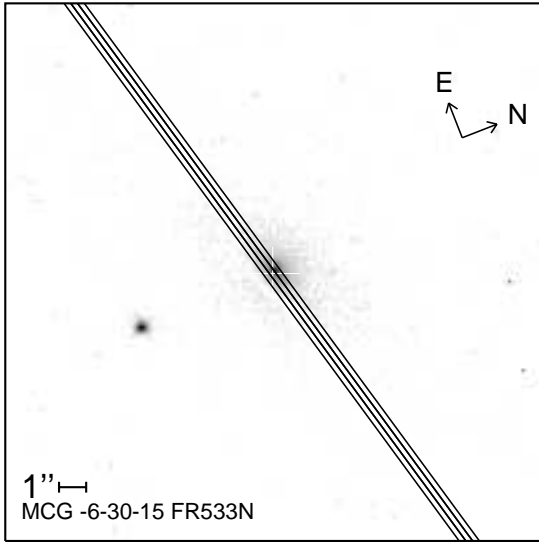
Fig. 27.— Same as Figure 24, but for NGC 3516. G430M kinematics are from Ruiz et al. (2001) data set, no FWHM or fluxes available.

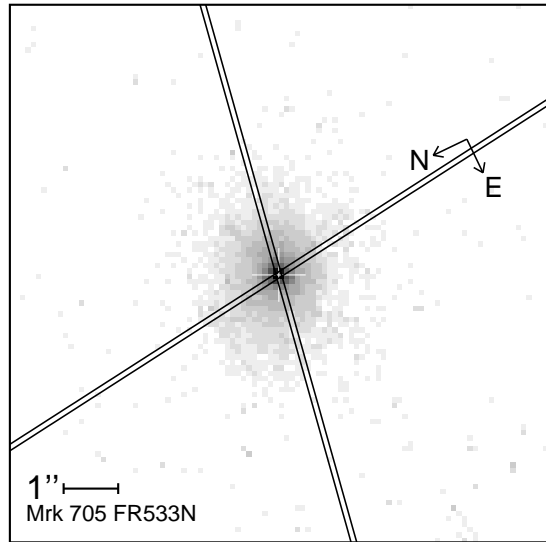
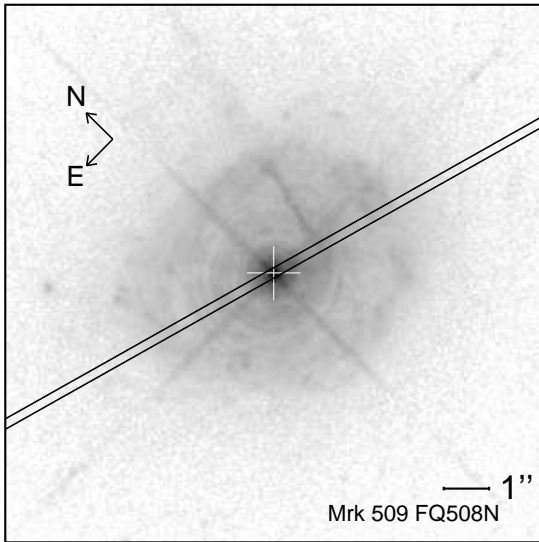
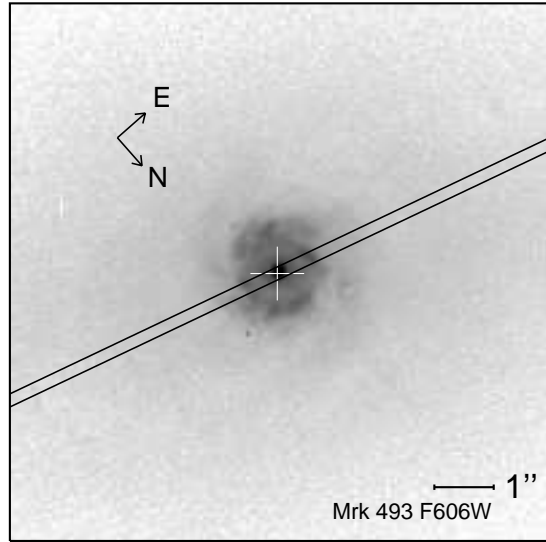
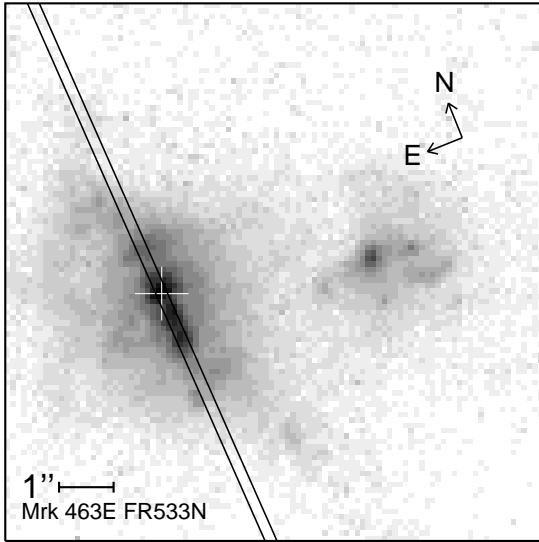
C. Online Figures

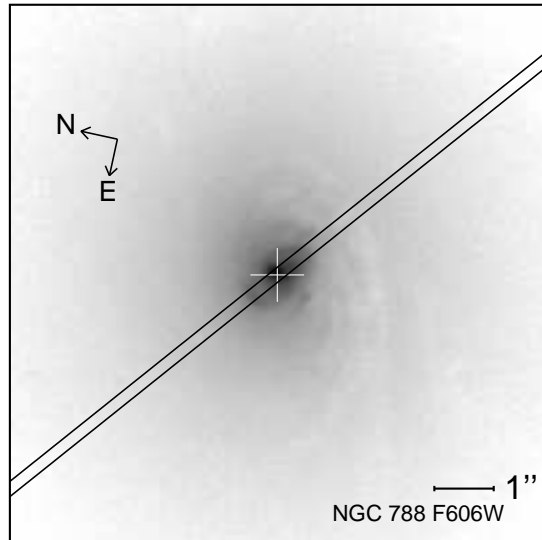
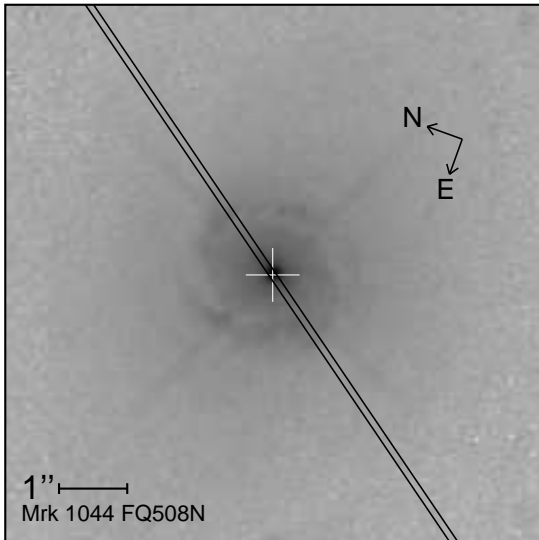
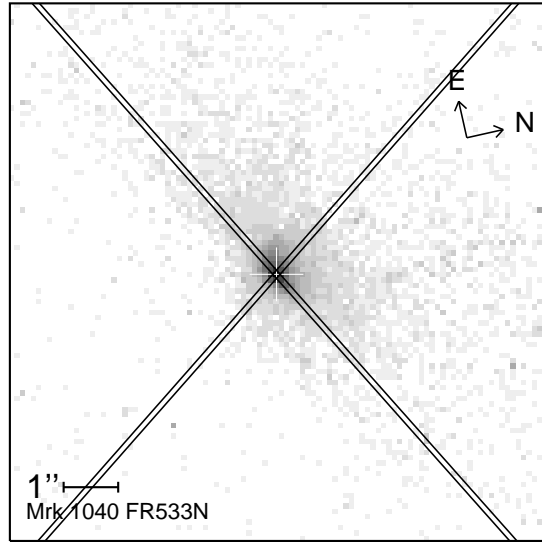
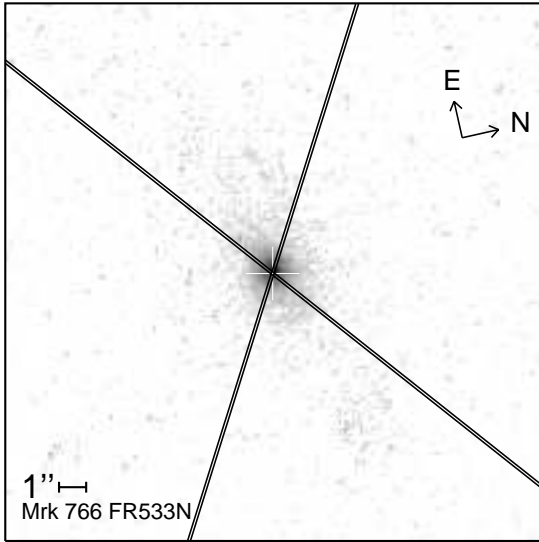
C.1. *HST* STIS Slit Positions

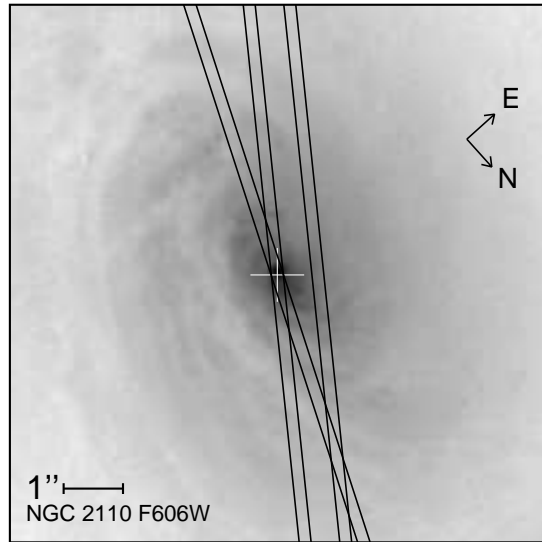
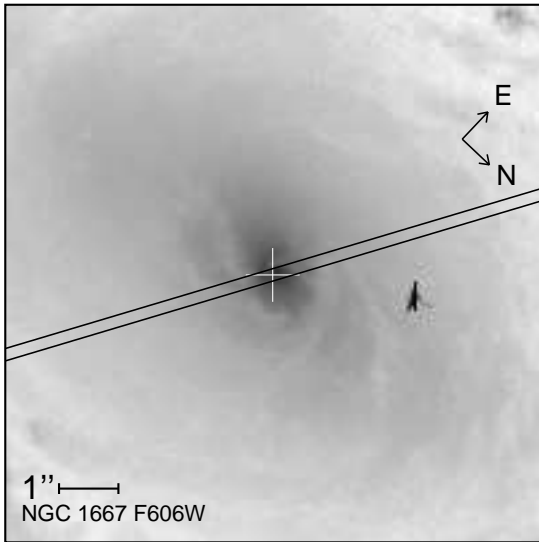
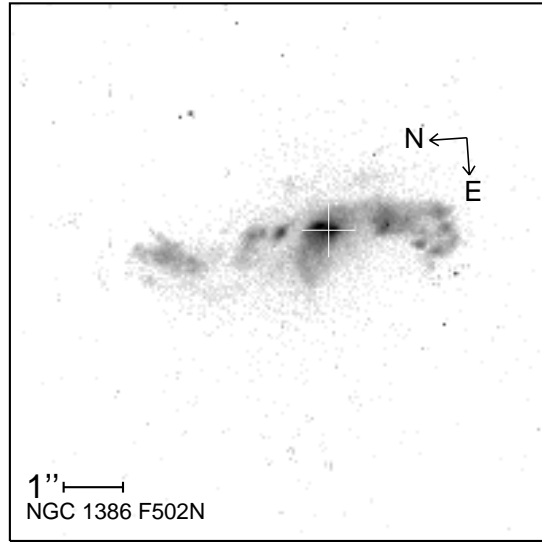
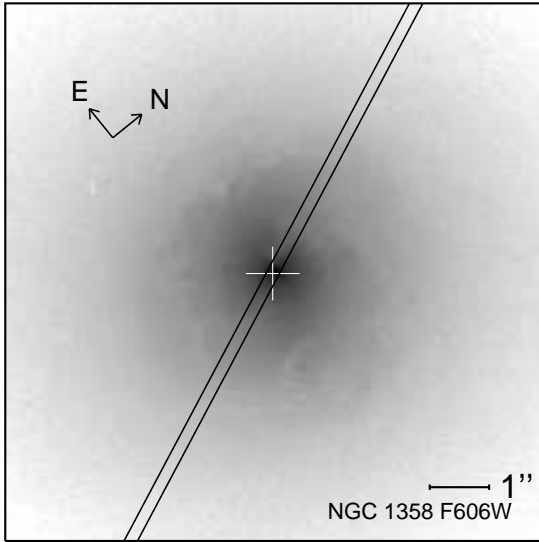
The appendix contains *HST* images of the extended sample. Filters centered on [O III] were used if available, otherwise F606W or F547M continuum filters are shown. Plus signs give the location of the optical continuum peaks. Solid lines outline the position of each STIS slit. Details for each observation are listed in Table 3. Images without slits are for targets using slitless STIS observations.

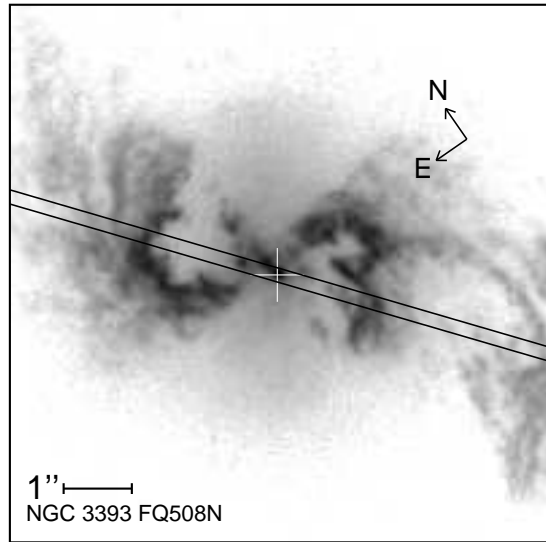
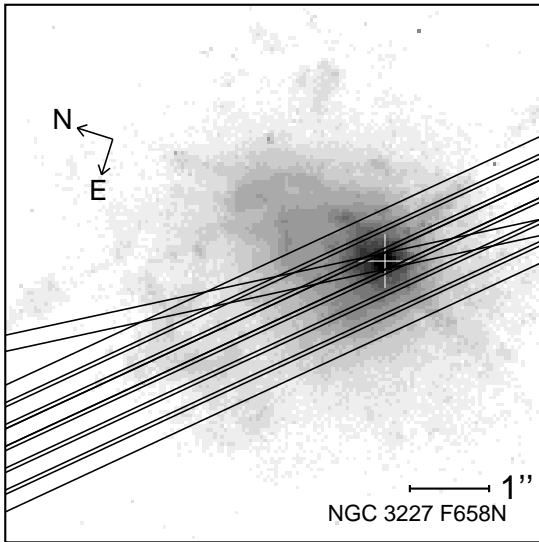
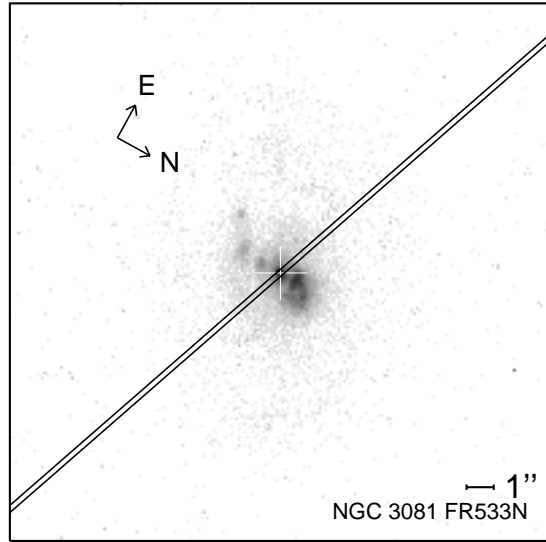
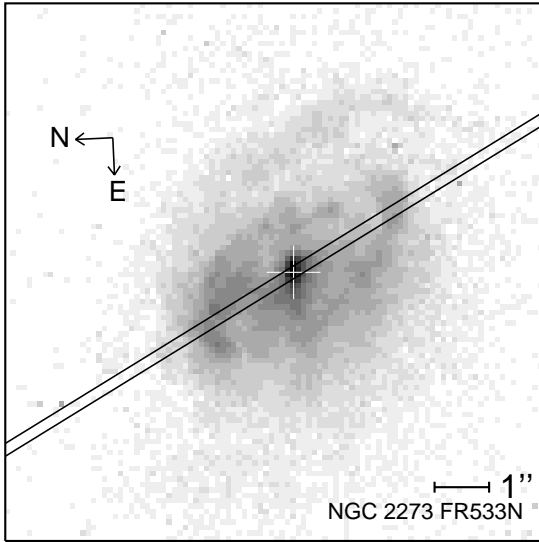


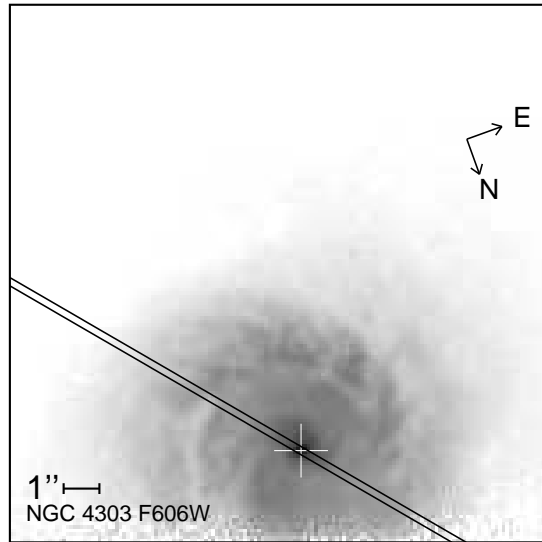
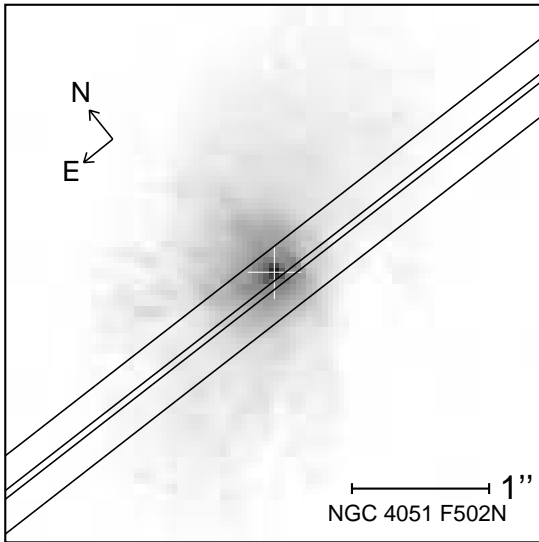
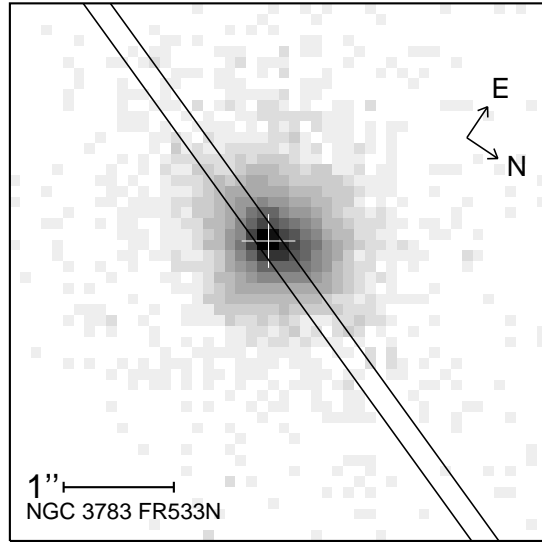
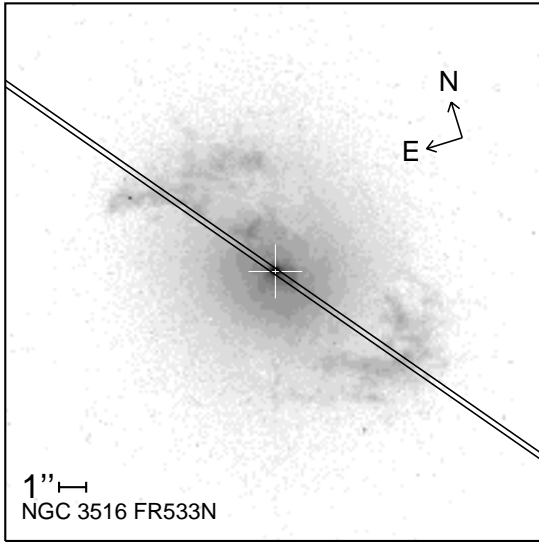


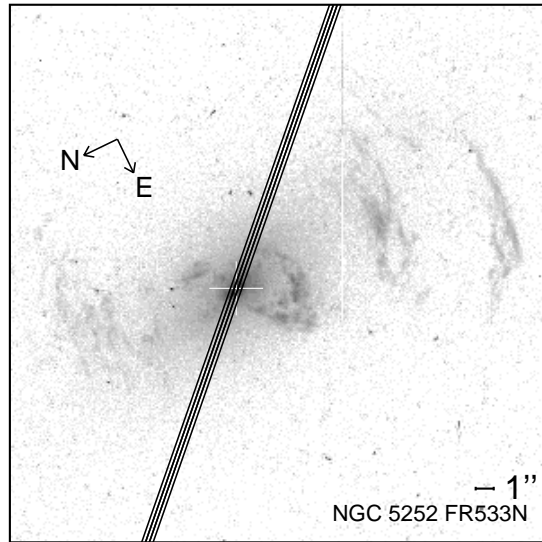
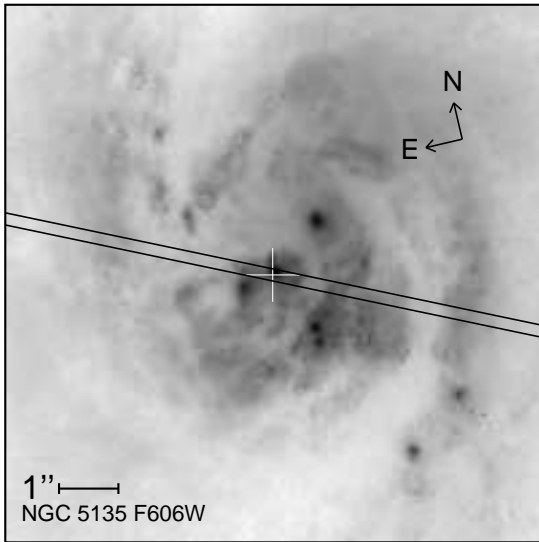
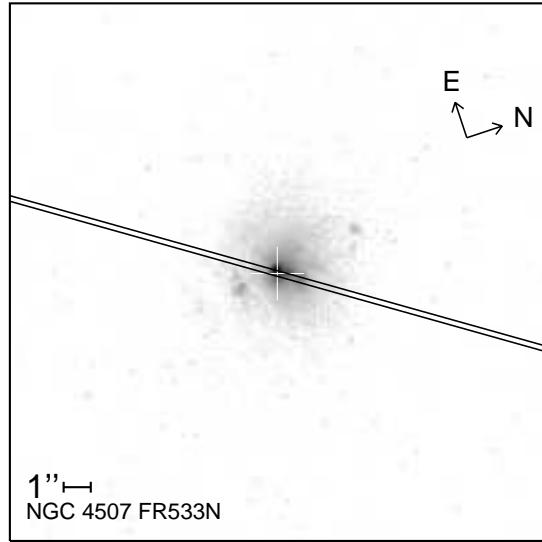
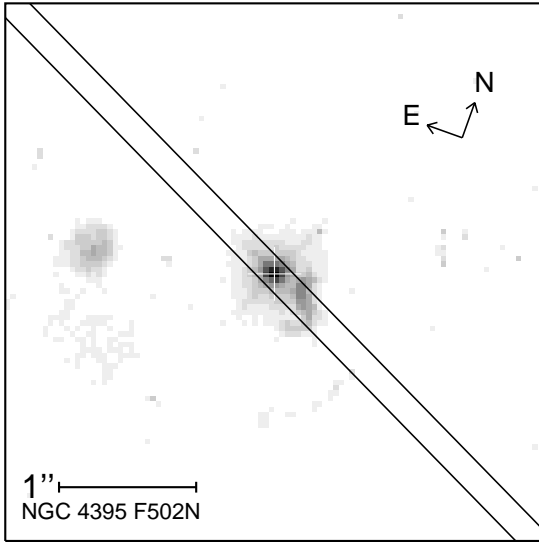


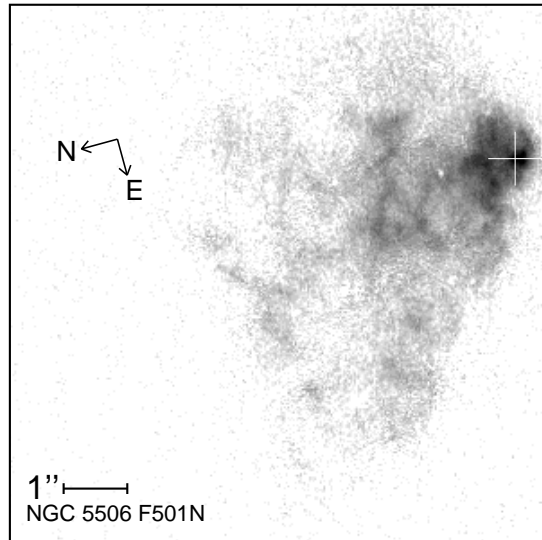
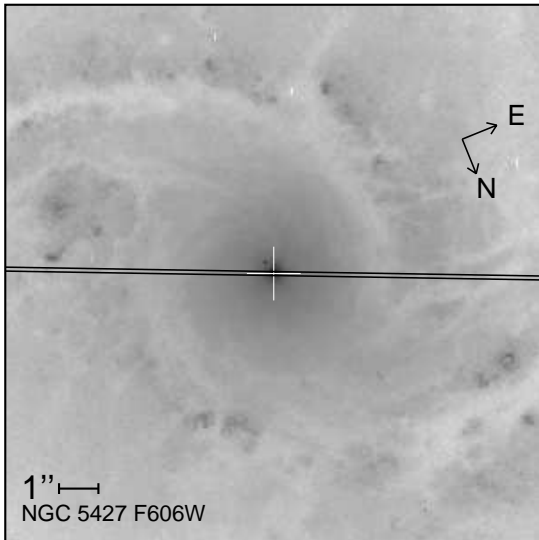
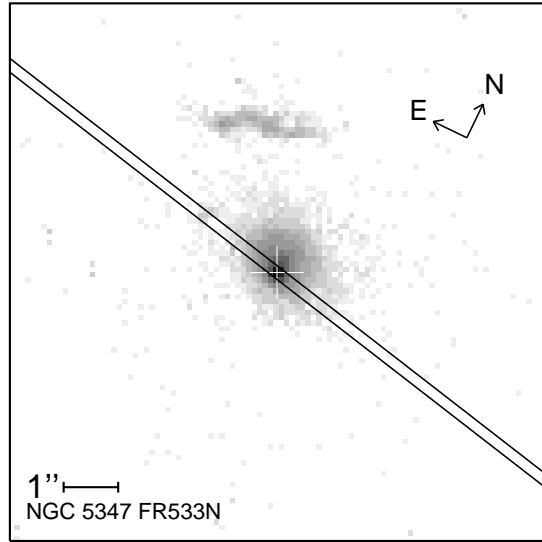
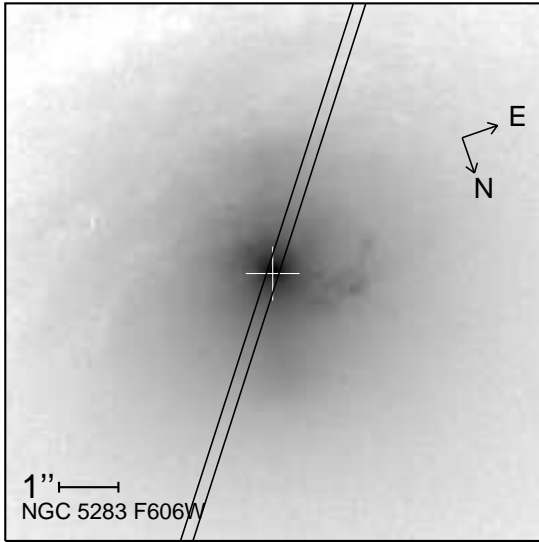


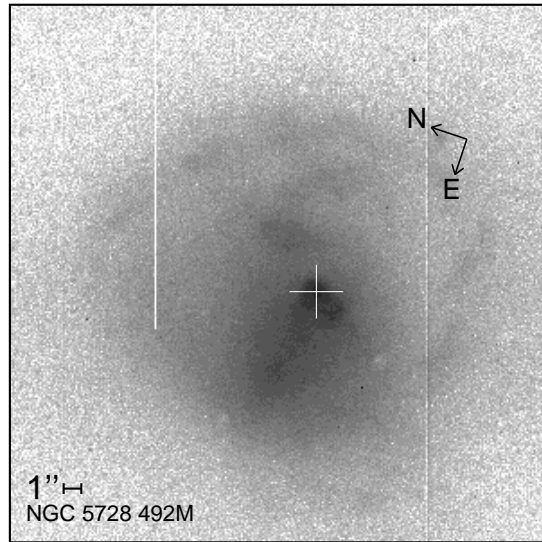
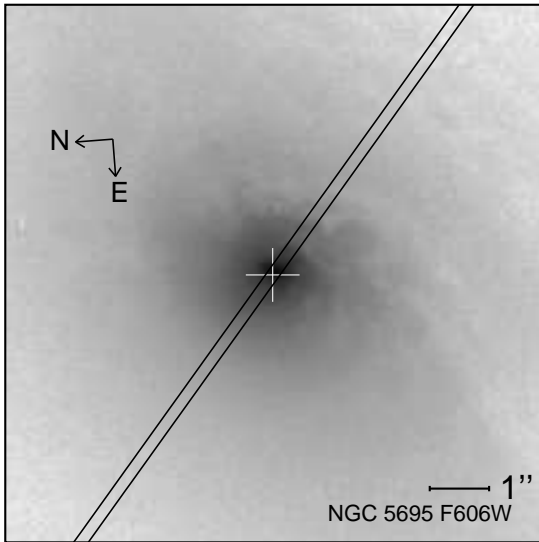
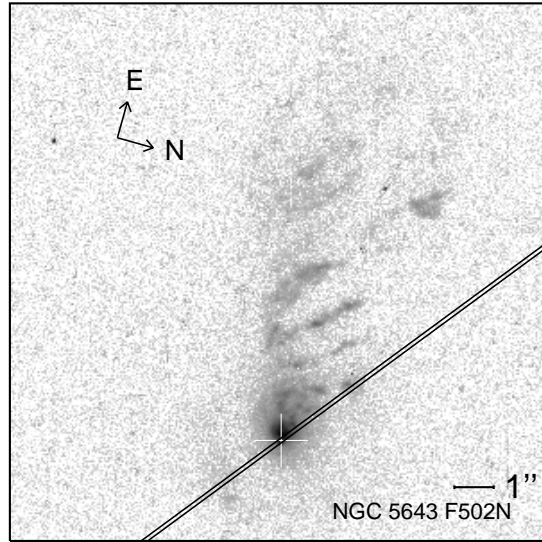
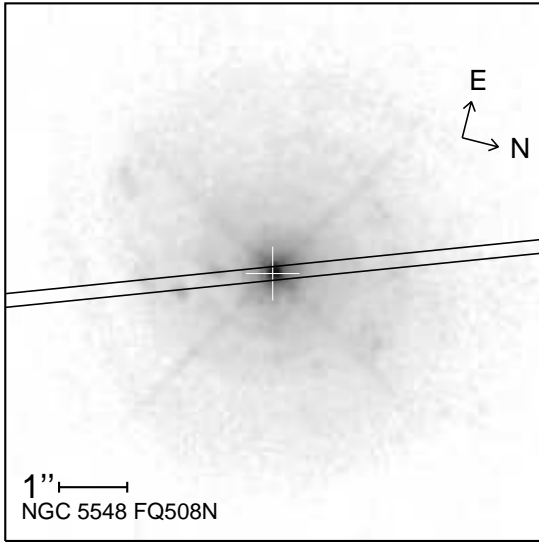


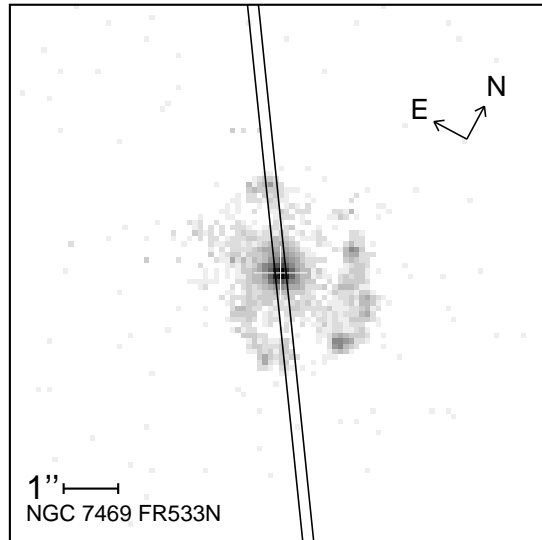
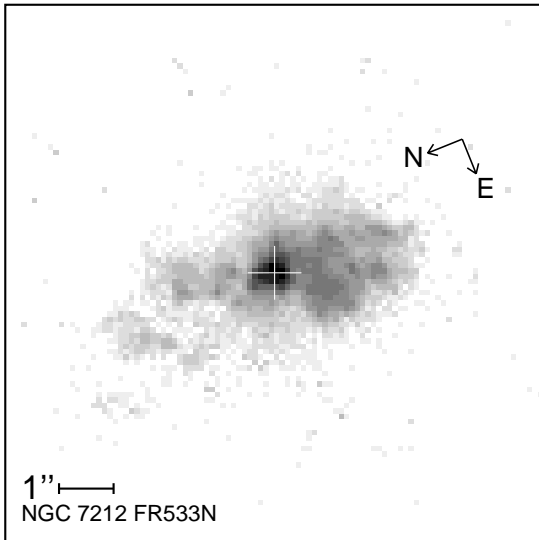
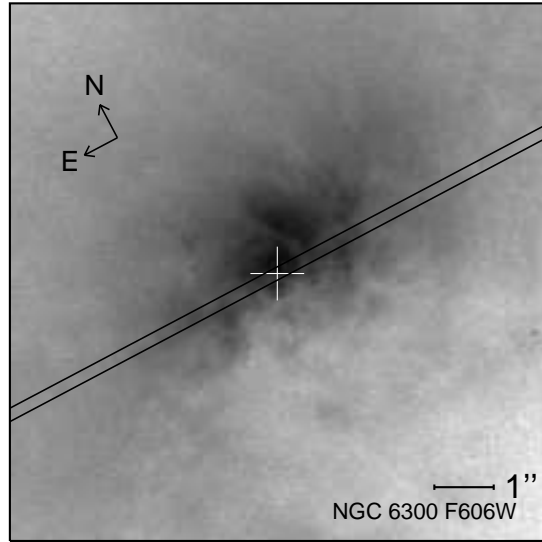
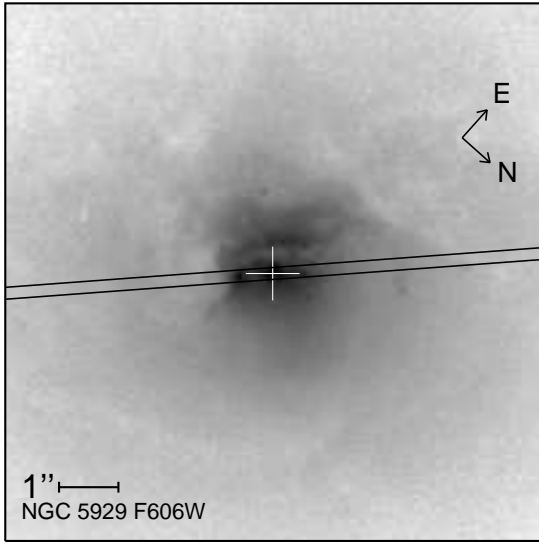


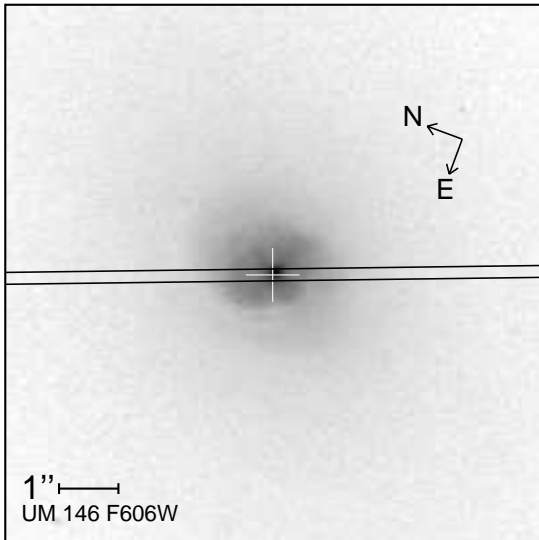
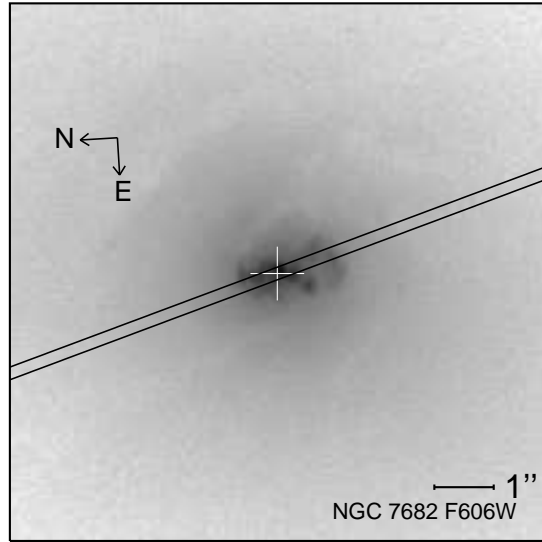
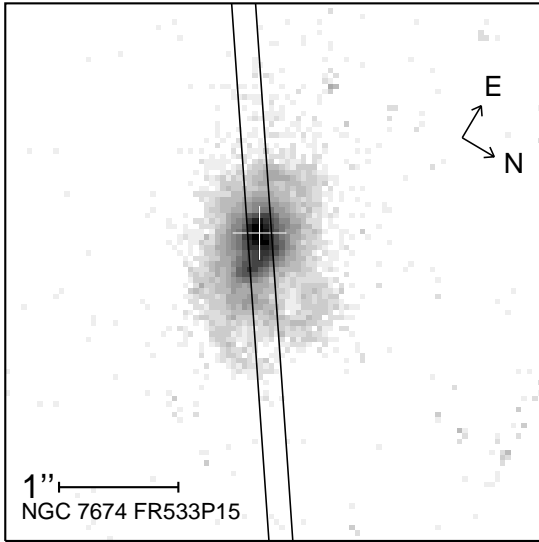












C.2. AGN Kinematic Data

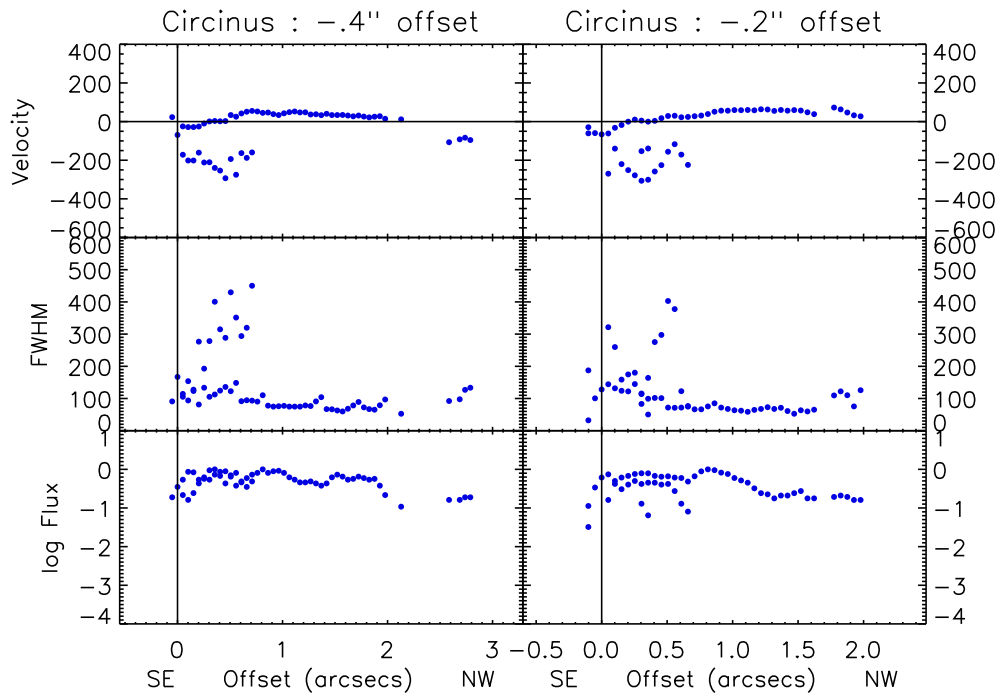
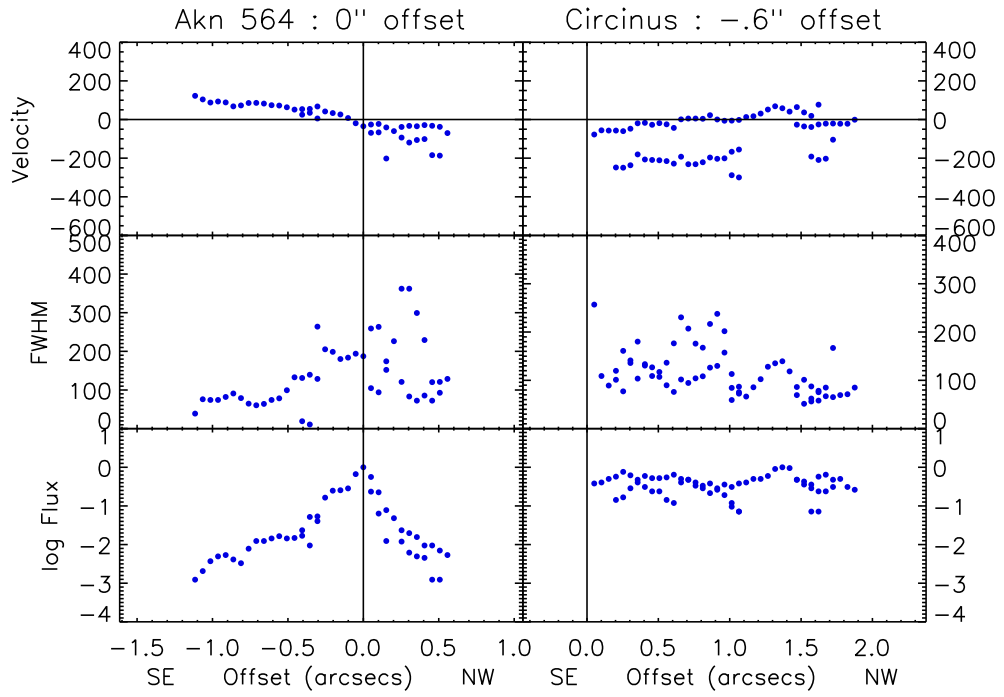
This appendix contains velocities, FWHMs, and normalized fluxes of each spectrum collected to create our expanded sample. Figures containing multiple data sets signify observations using separate gratings at an identical position. Kinematic data for slitless observations are available in Ruiz et al. (2005).

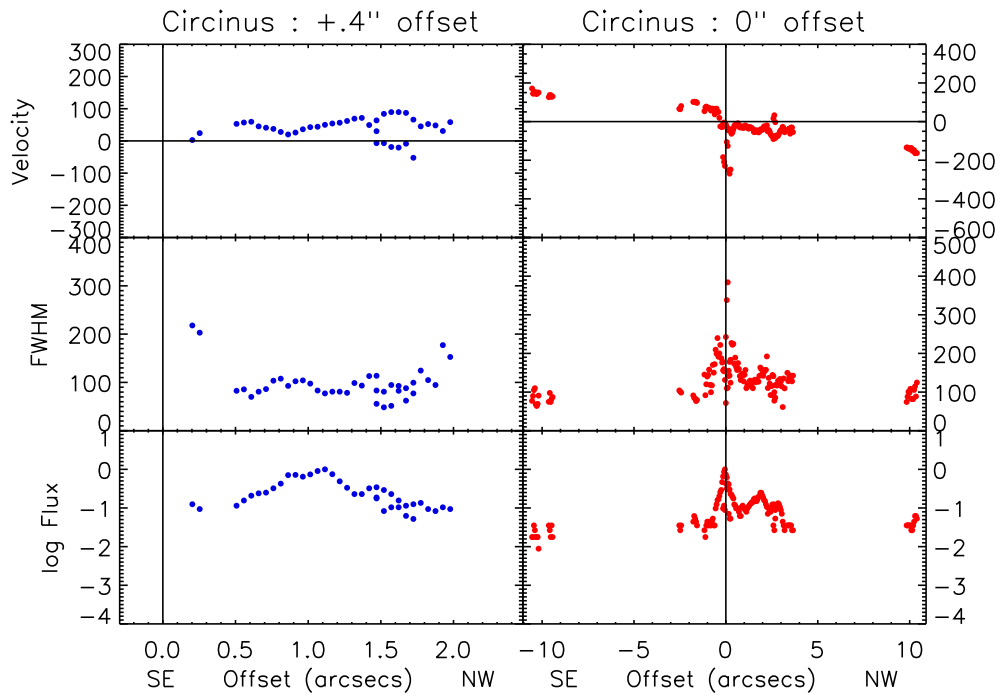
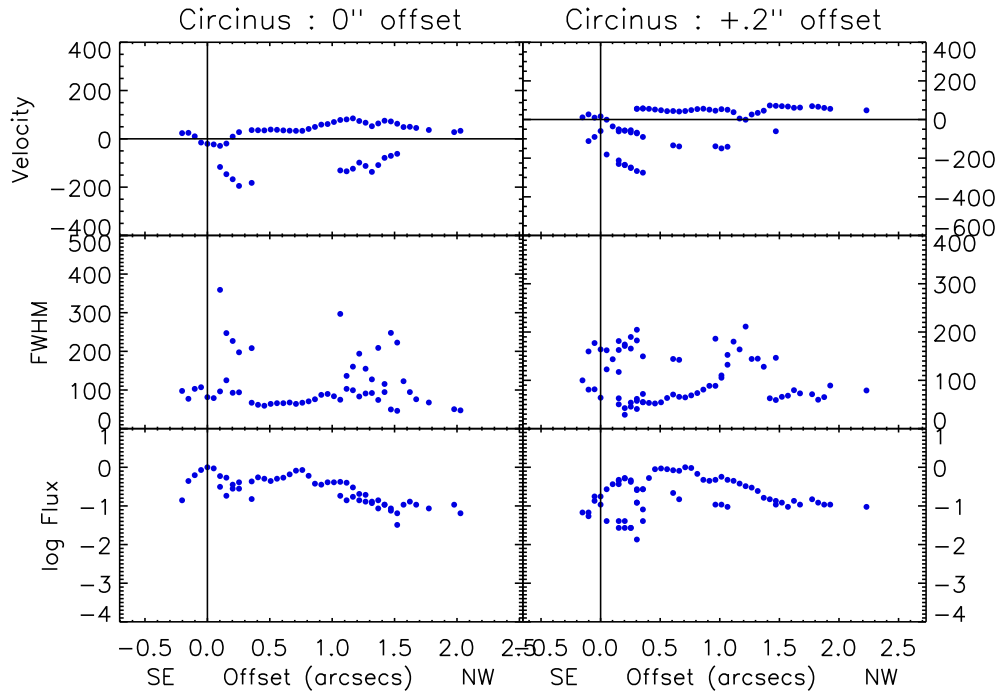
Kinematics data correspond to *HST* gratings as follows:

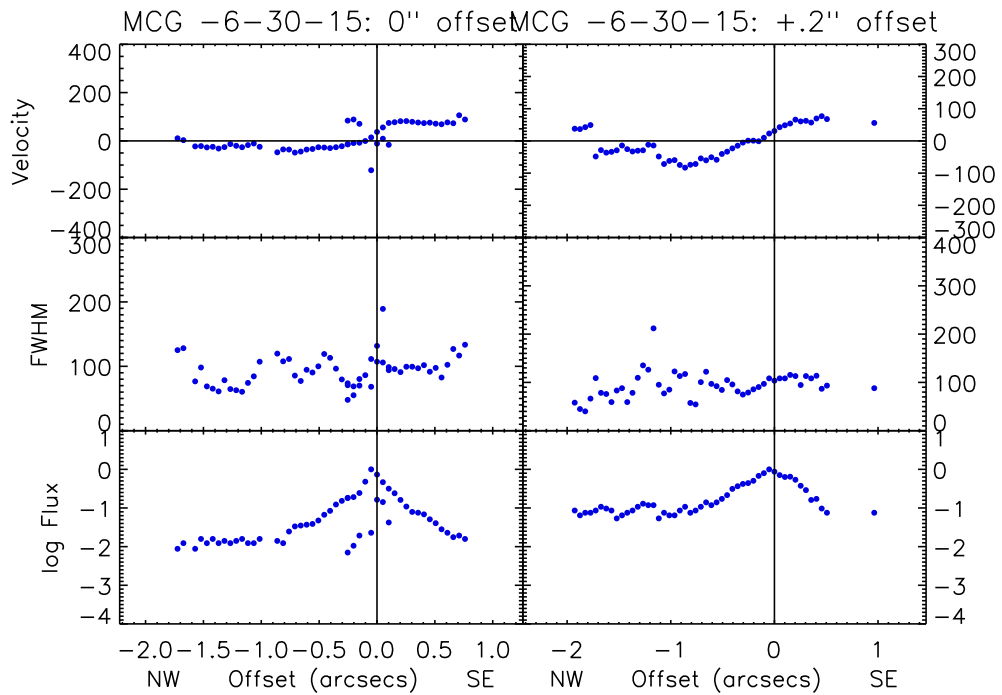
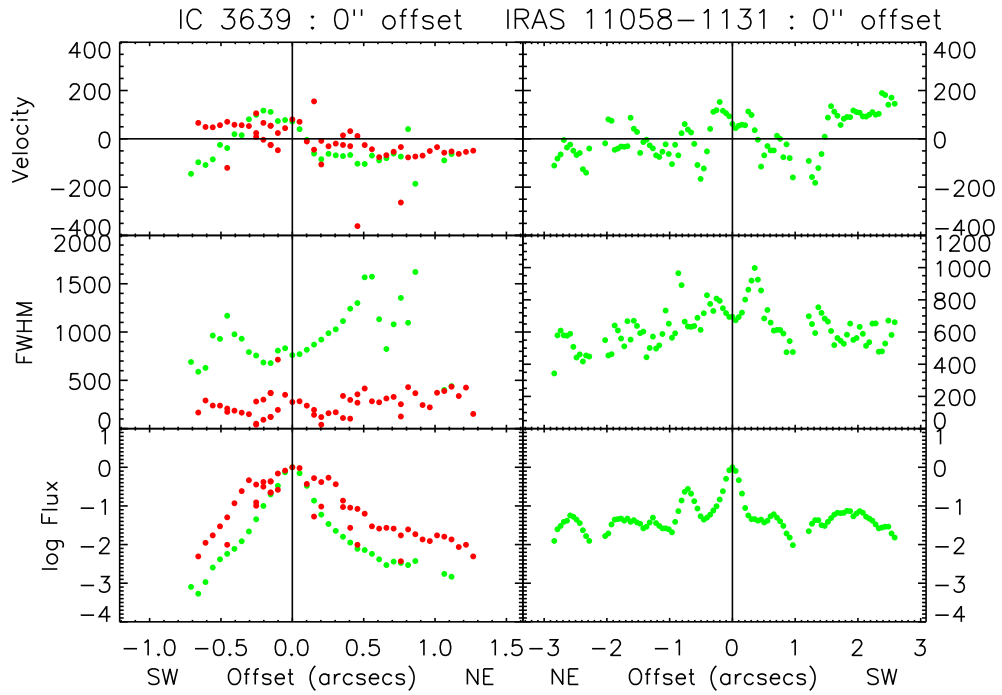
Green diamonds: [O III] 5007 emission line using G430L grating

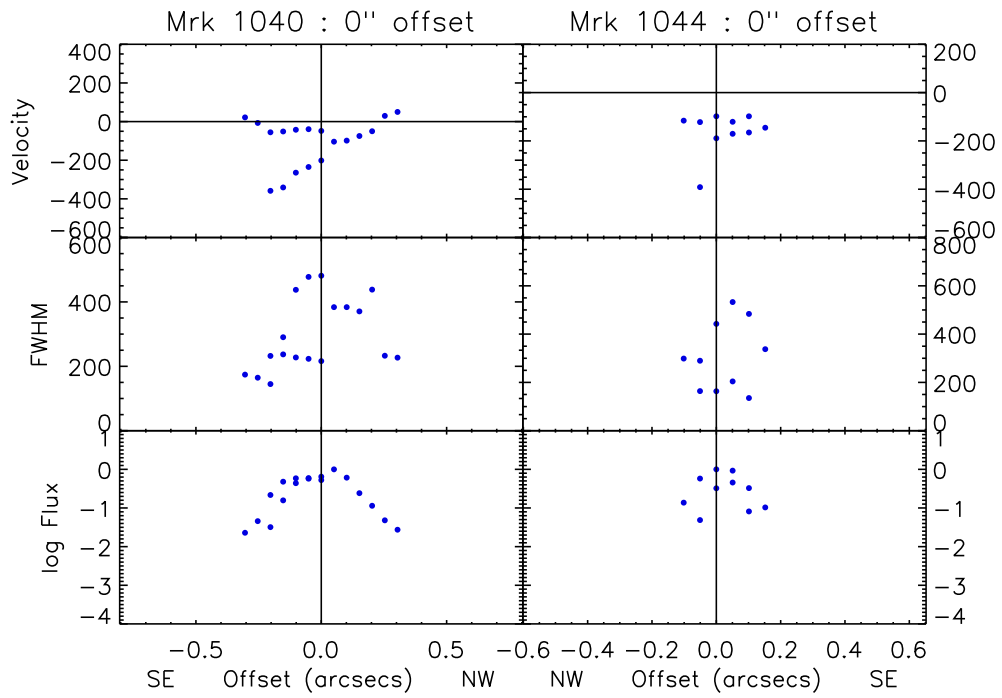
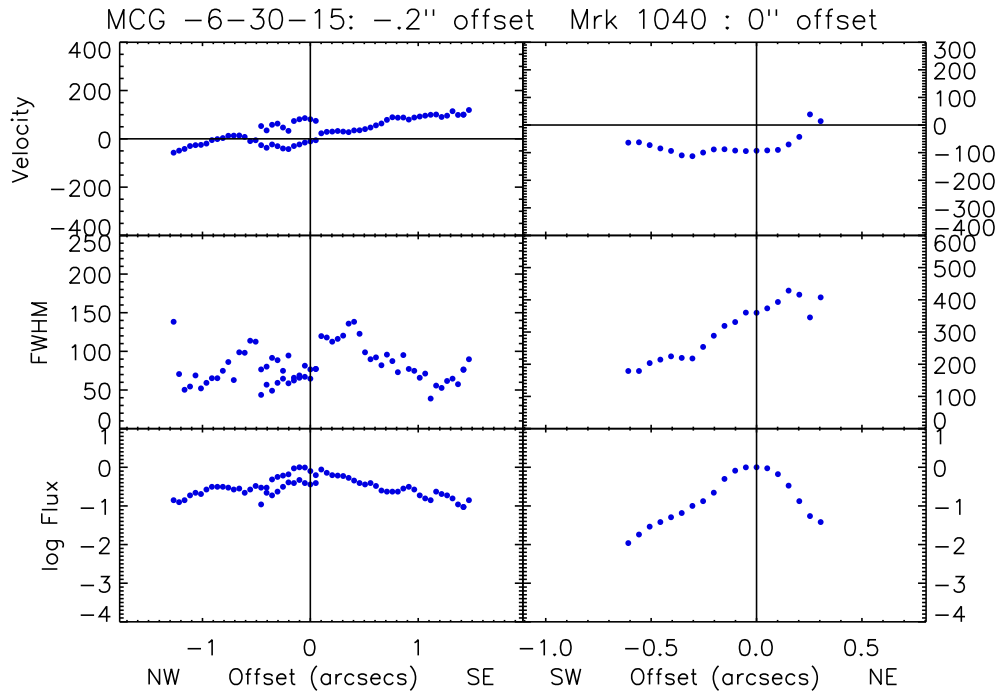
Blue circles: [O III] 5007 emission line using G430M grating

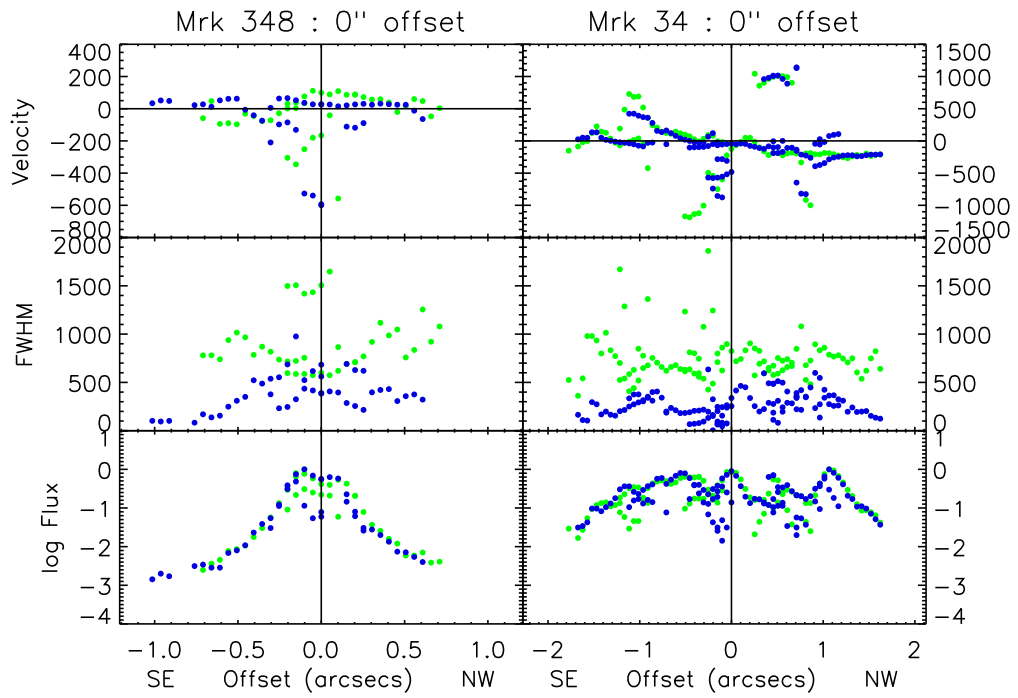
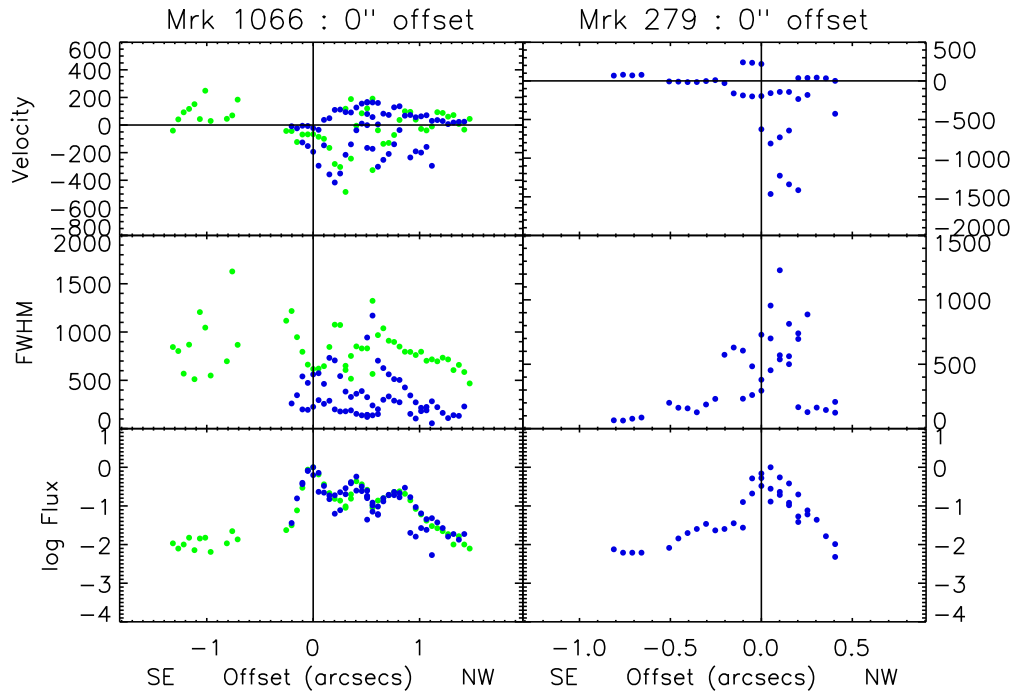
Red squares: H α 6564 emission line using G750M grating

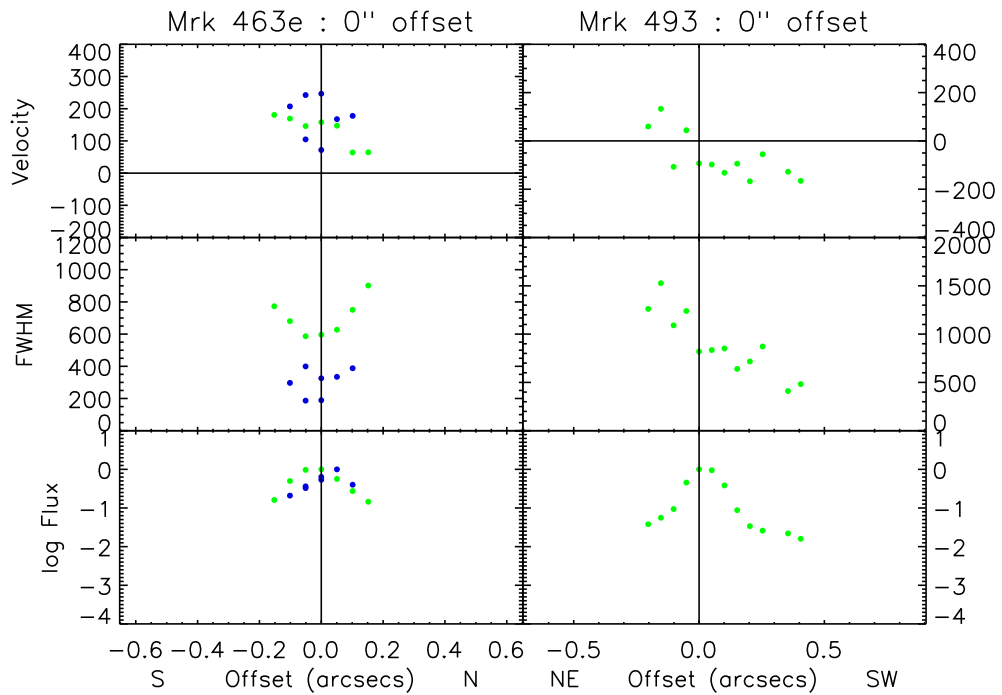
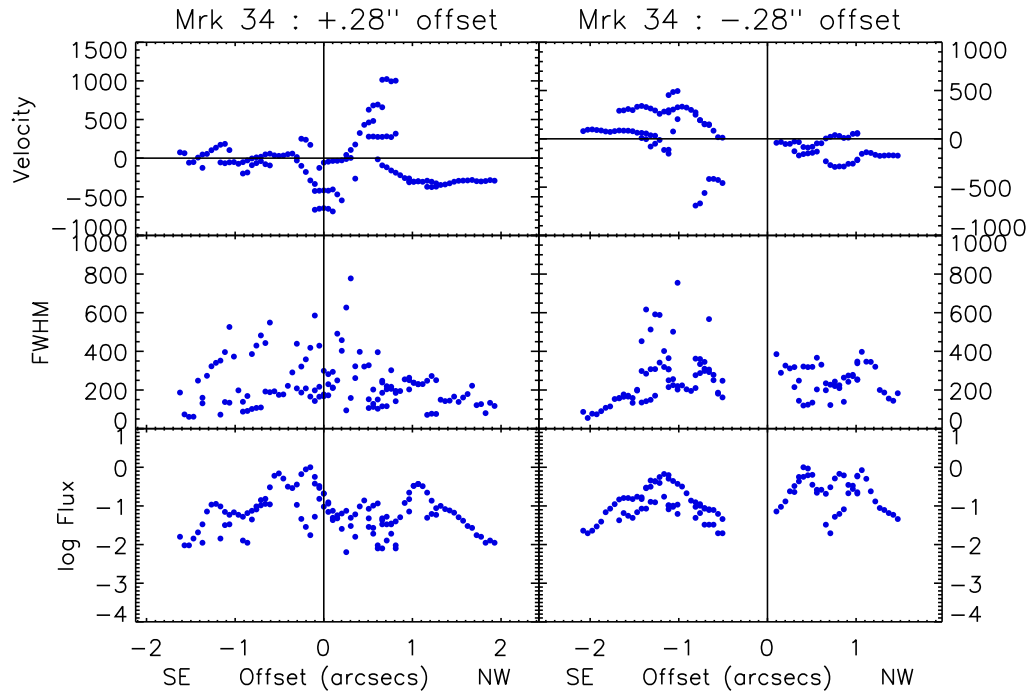


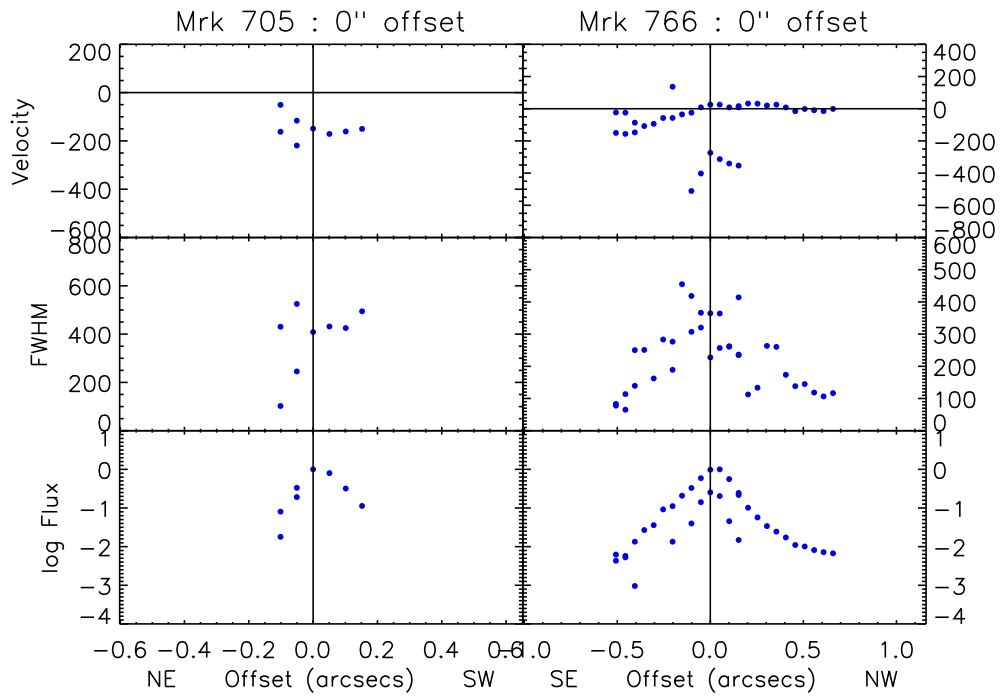
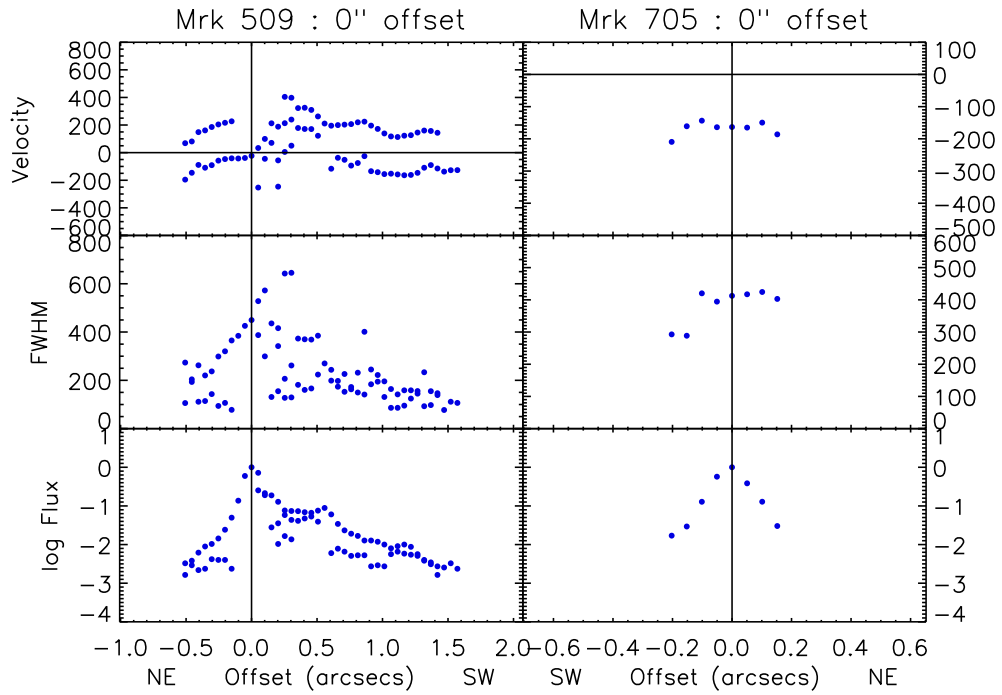


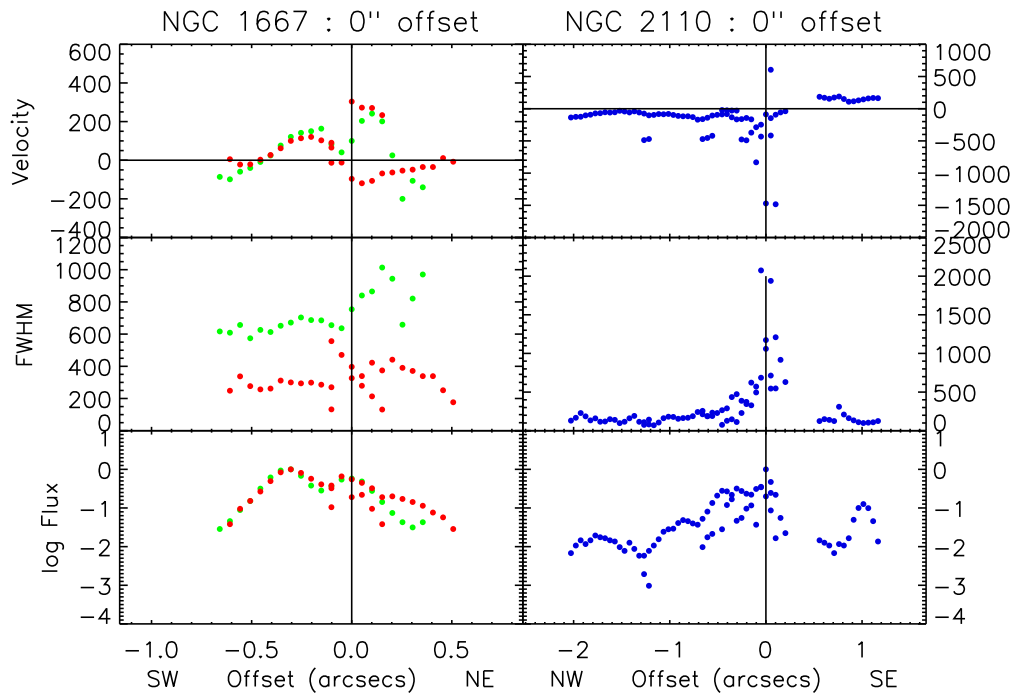
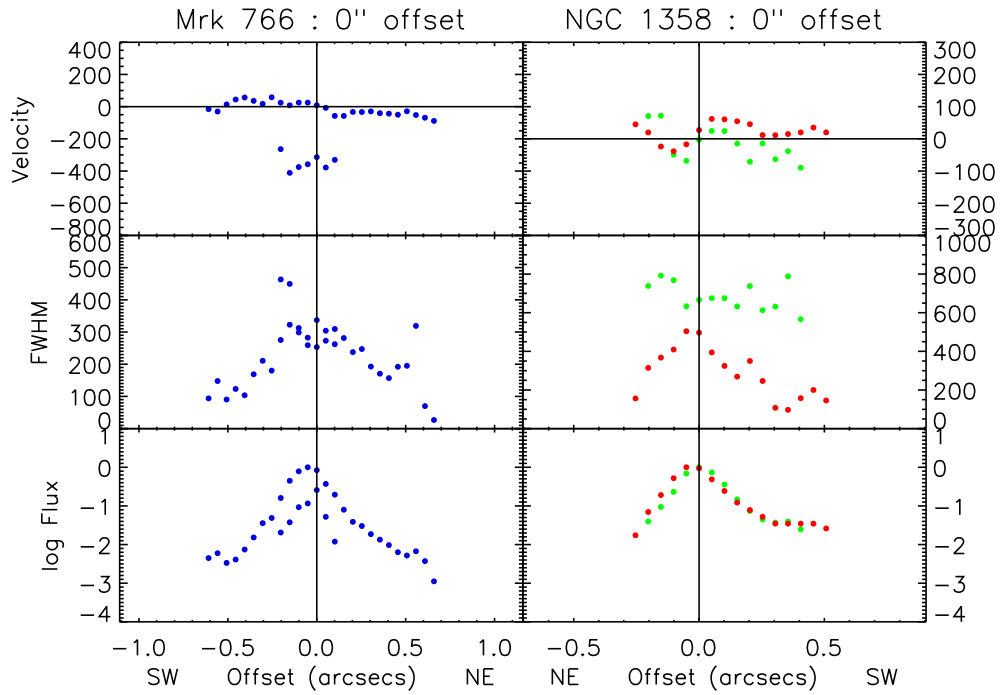


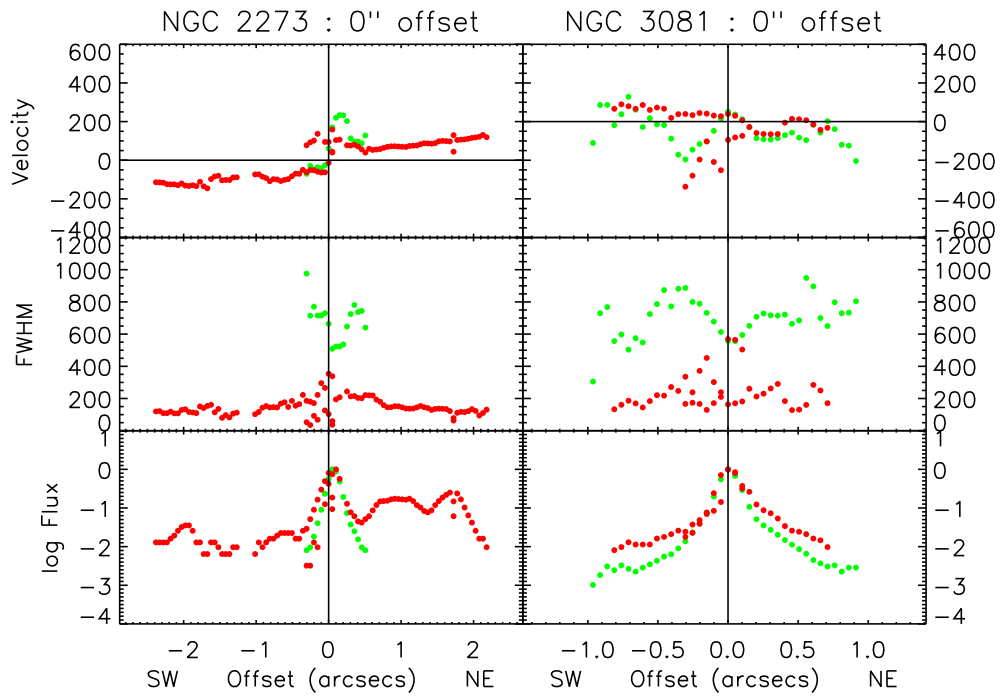
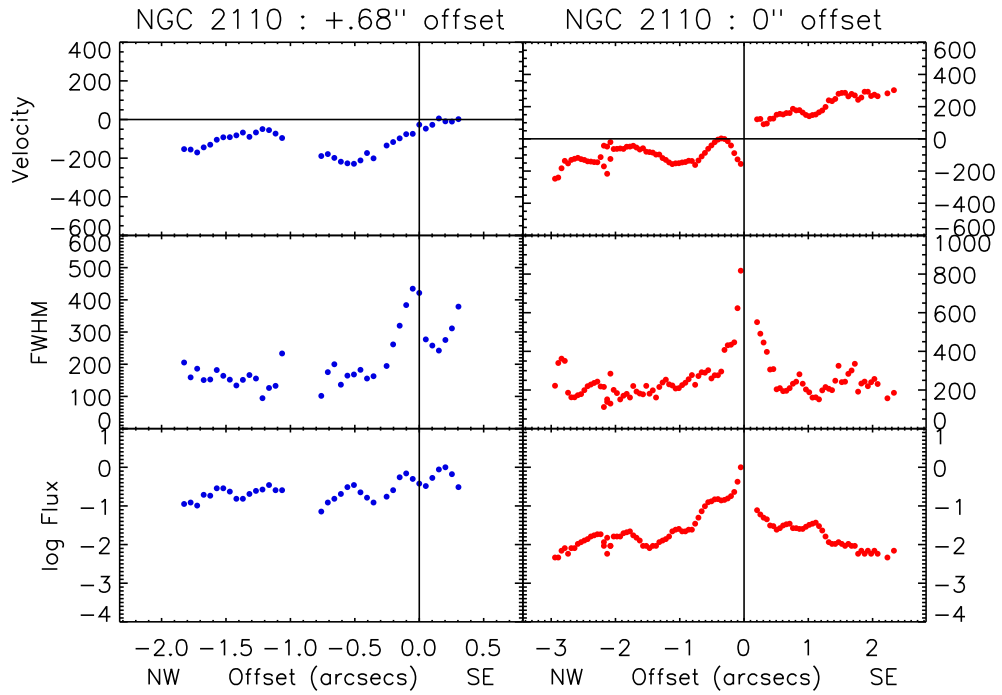


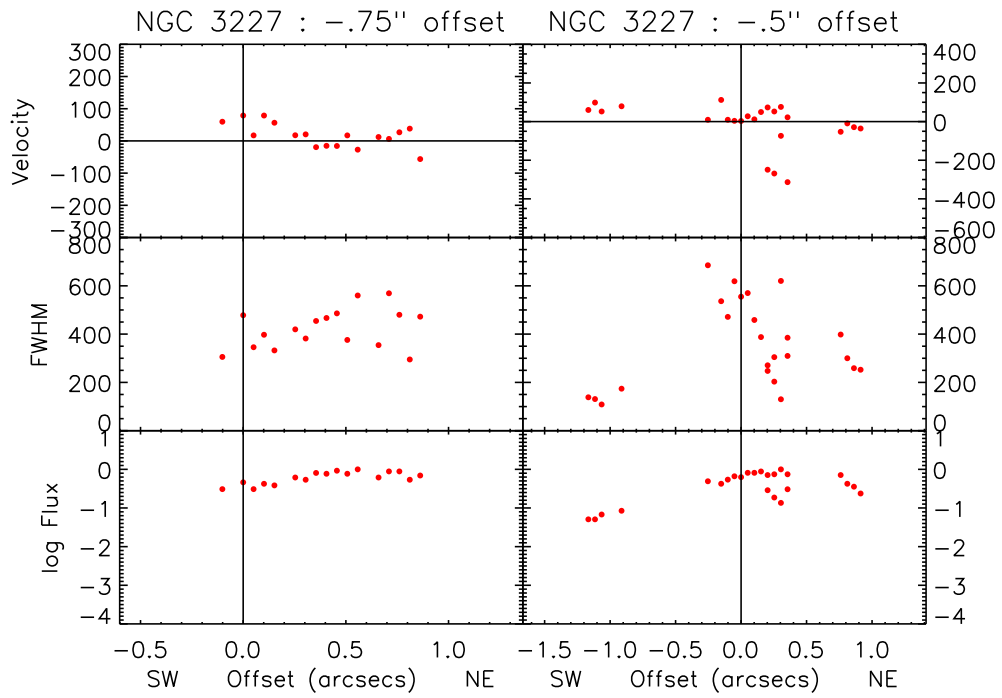
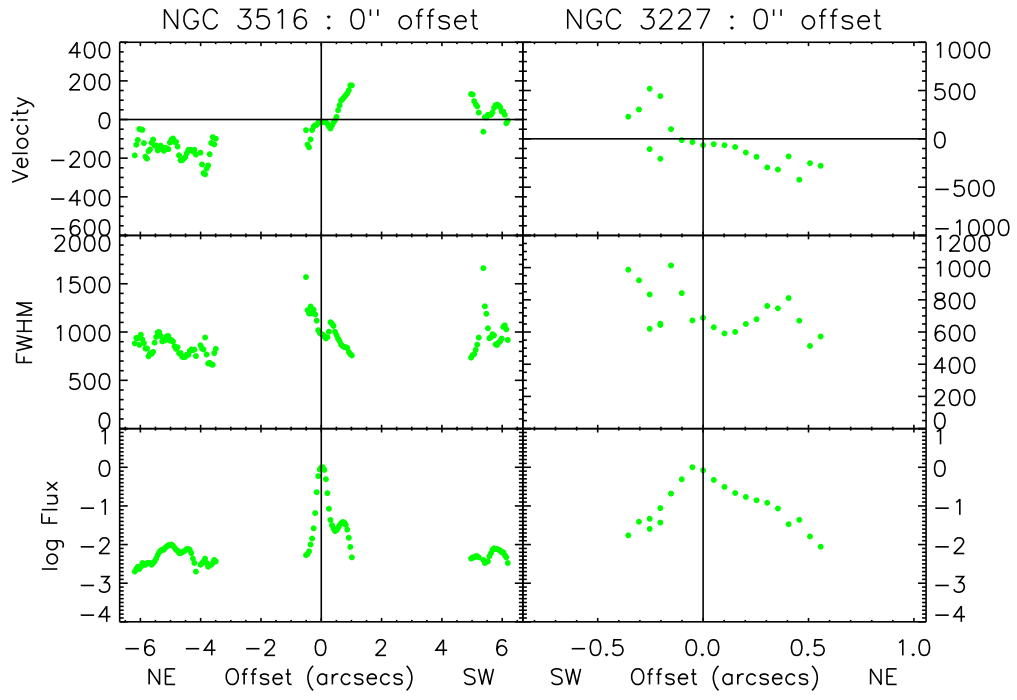


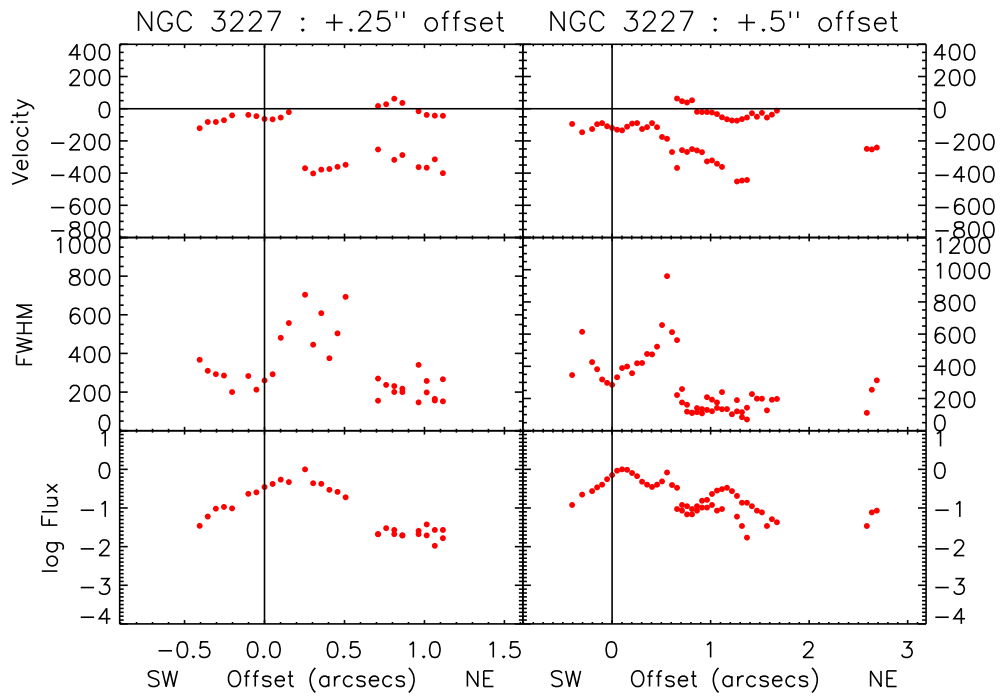
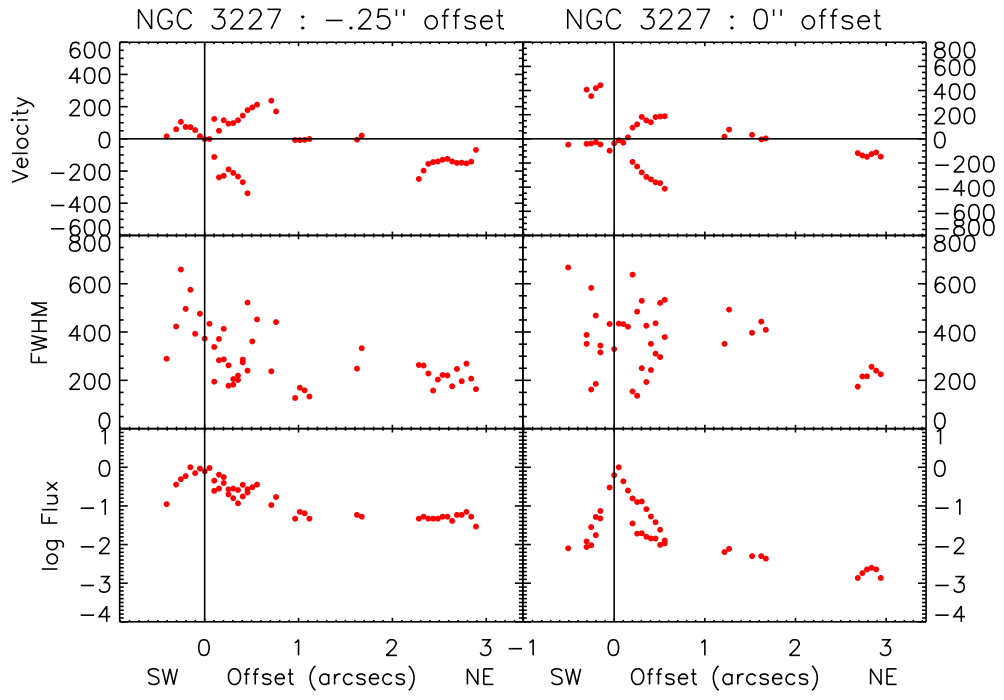


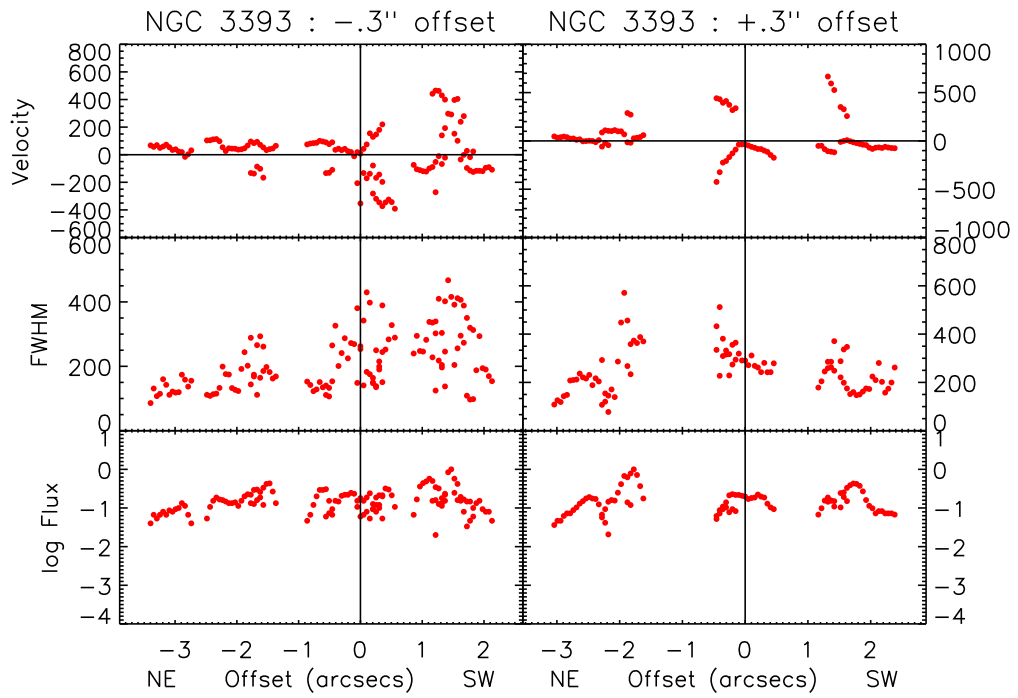
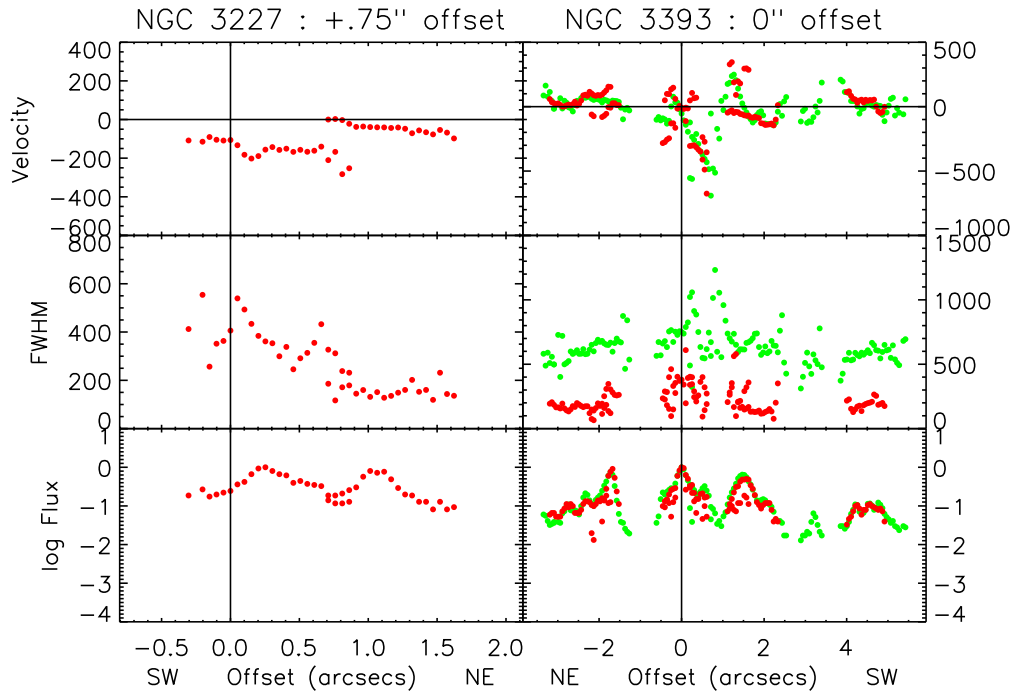


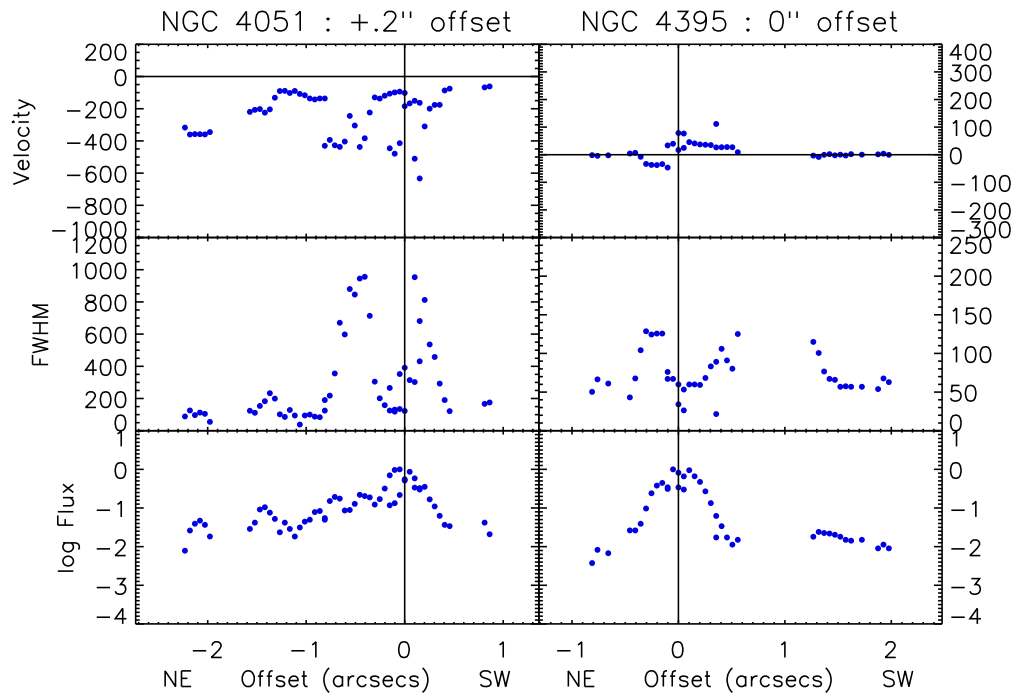
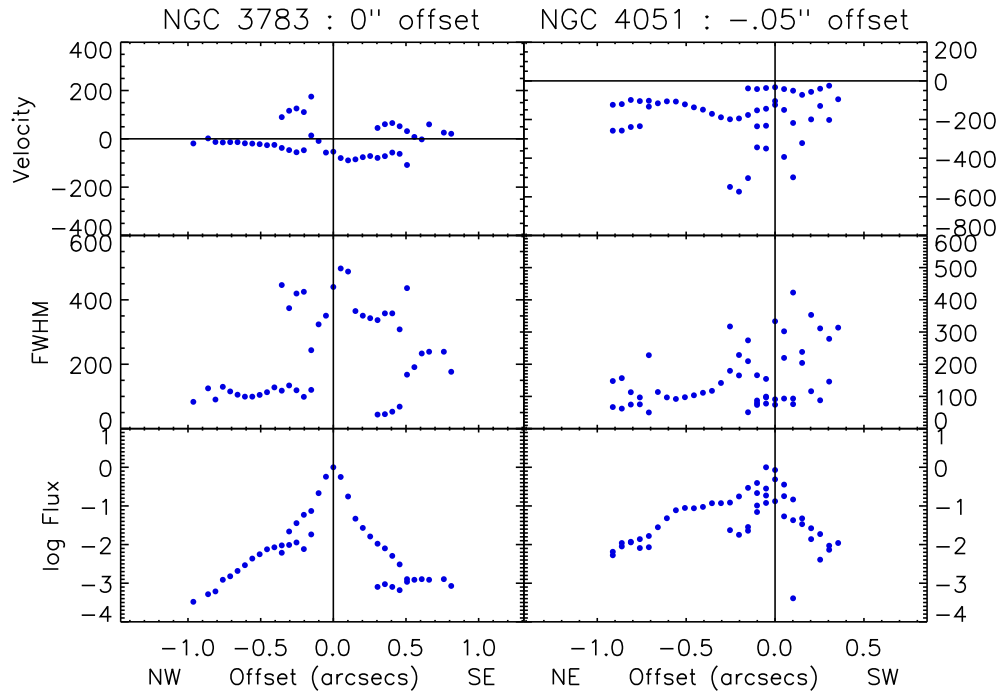


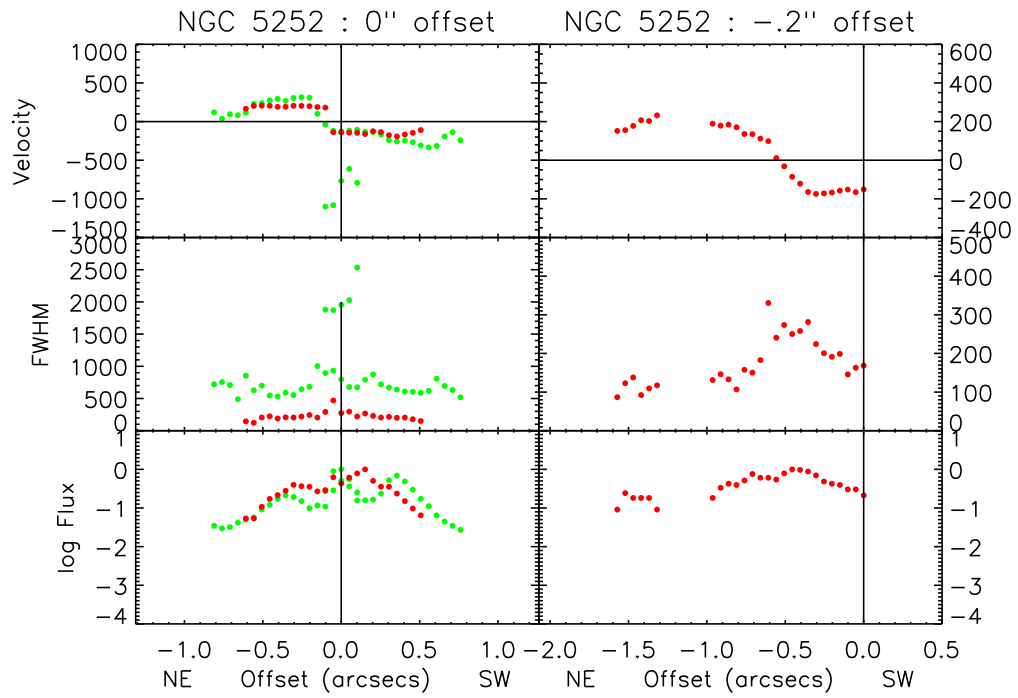
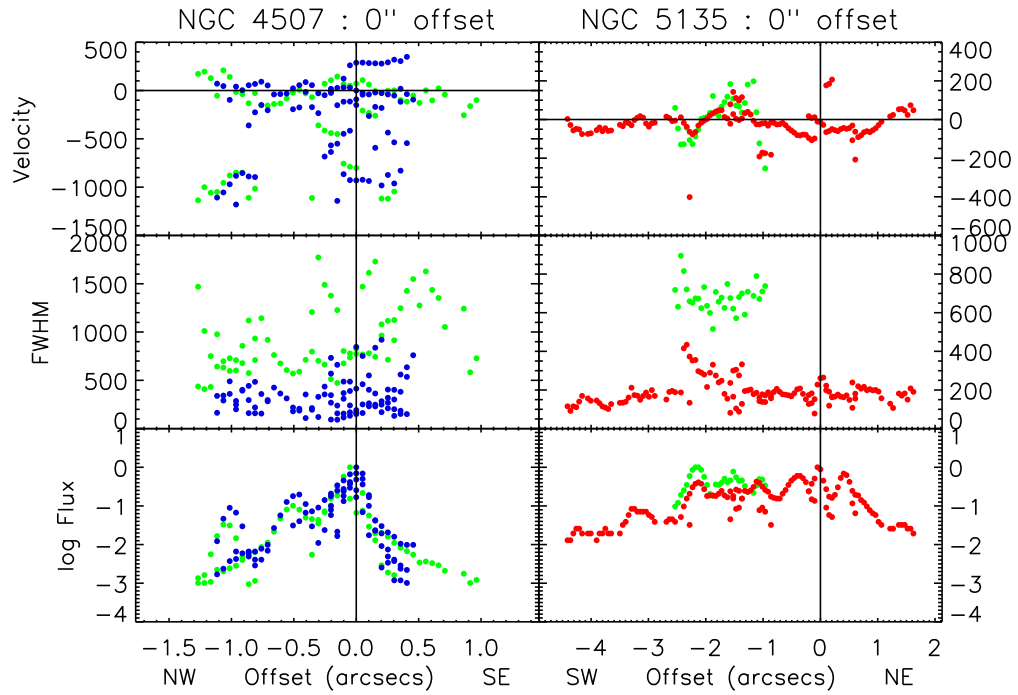


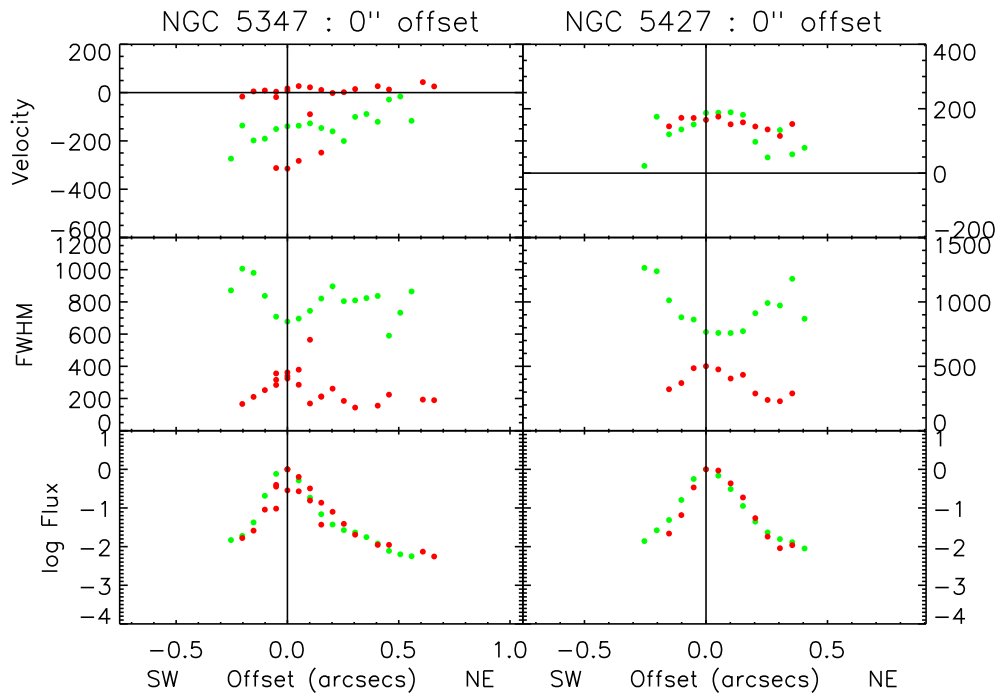
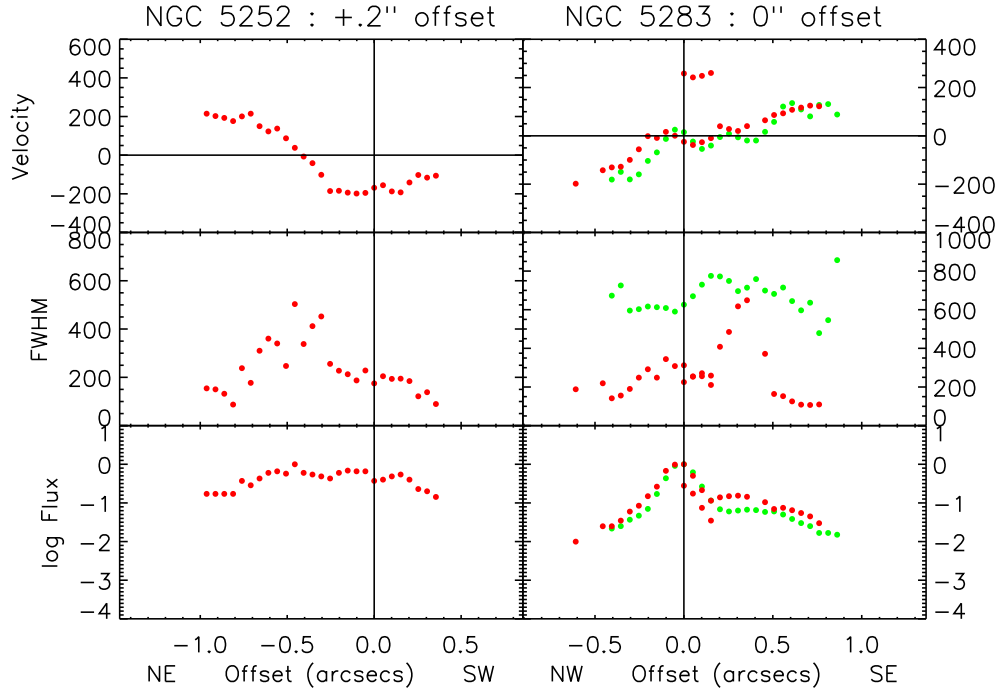


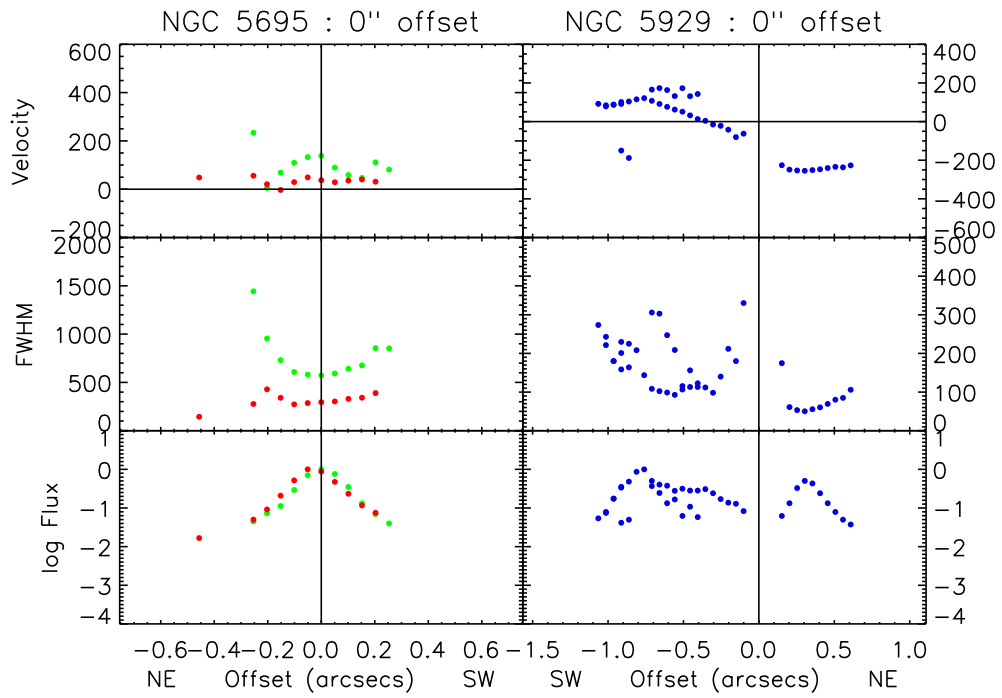
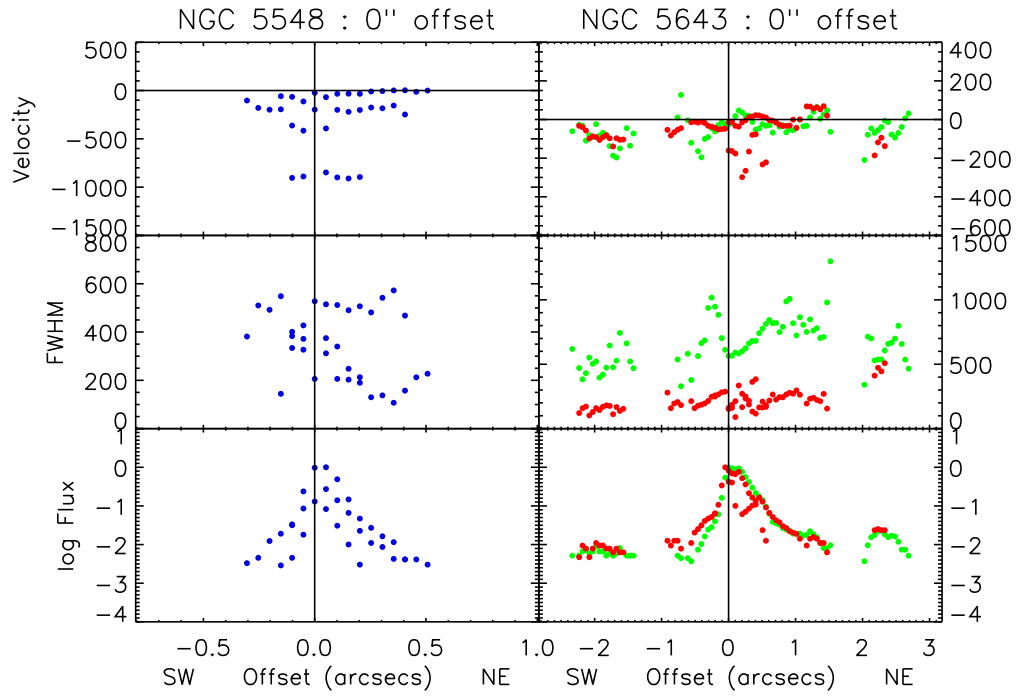


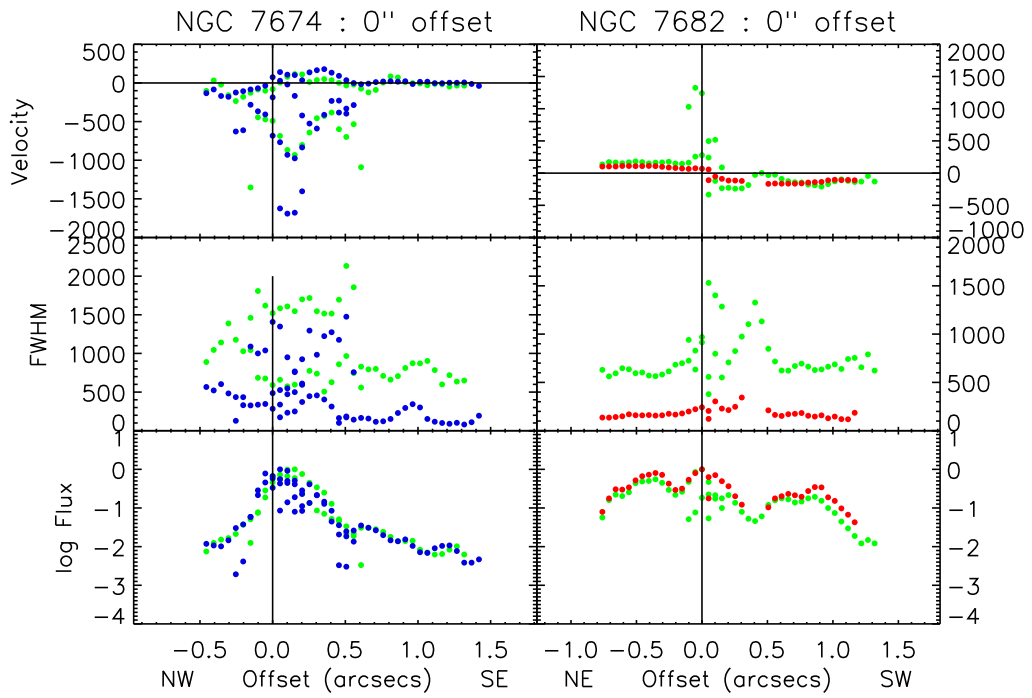
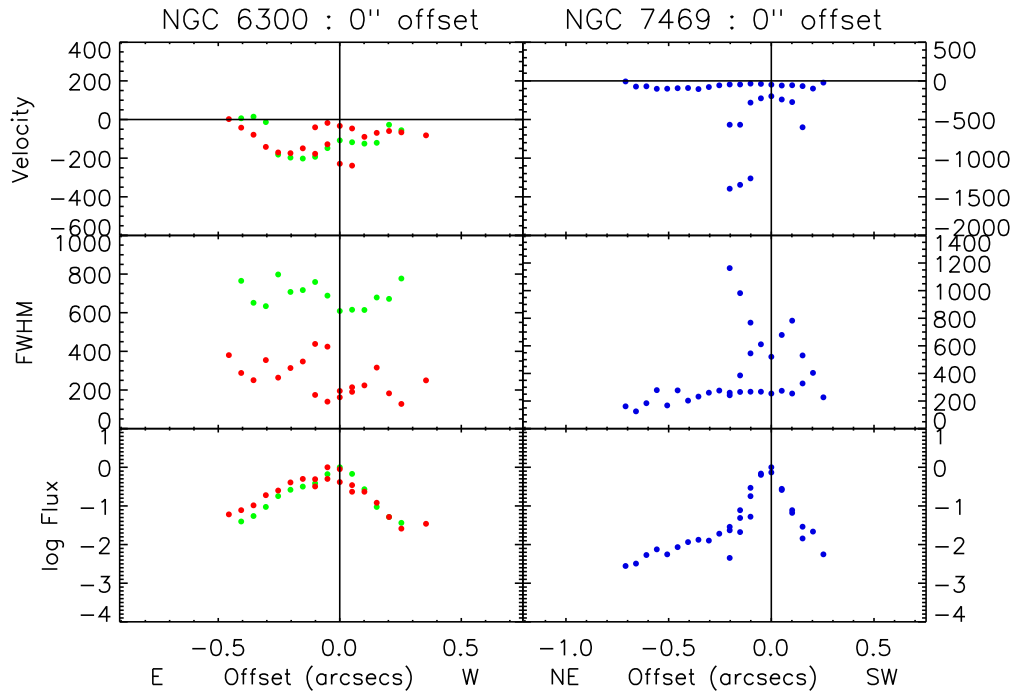


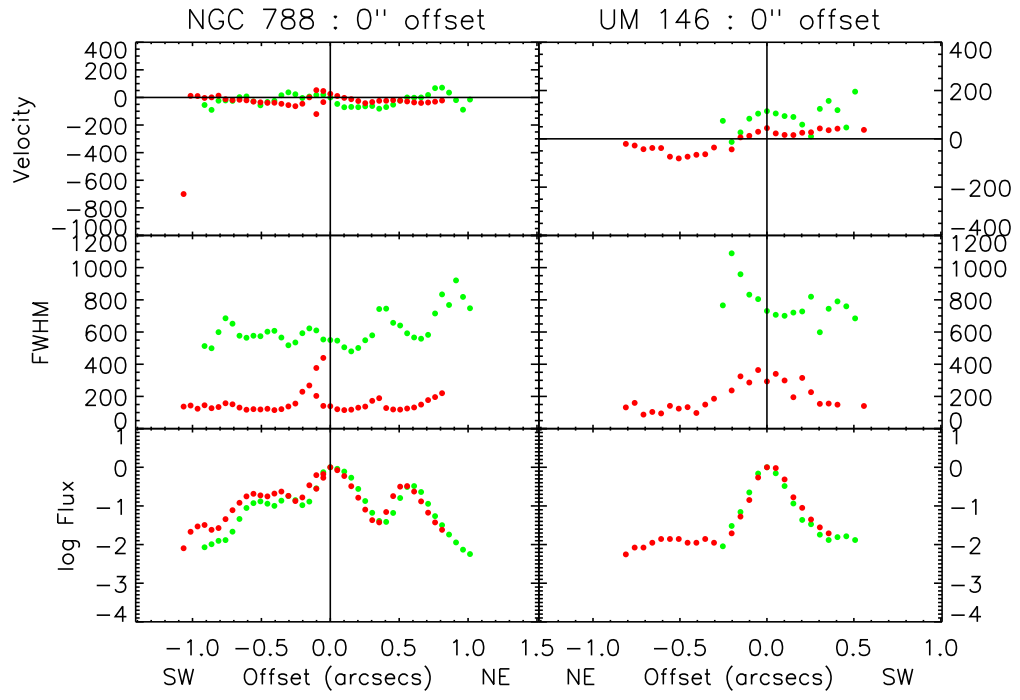












C.3. AGN Kinematic Models

Kinematics model chosen as the best fit for our radial velocity data set for modeled AGN. Parameters used to create this model are given in Table 6.

Kinematics data correspond to *HST* gratings as follows:

Green diamonds: [O III] 5007 emission line using G430L grating

Blue circles: [O III] 5007 emission line using G430M grating

Red squares: $H\alpha$ 6564 emission line using G750M grating

